Title
Spin Coherence and Vibrational Tunneling in Coupled Quantum Dot Pairs

Author
Jennings, Cameron Lamar

Publication Date
2020

Peer reviewed|Thesis/dissertation

UNIVERSITY OF CALIFORNIA, MERCED

Spin Coherence and Vibrational Tunneling in Coupled Quantum Dot Pairs

A dissertation submitted in partial satisfaction
of the requirements for the degree of

Doctor of Philosophy

in

Physics

by

Cameron L. Jennings

Committee in Charge:

Professor Jay Sharping, Chair
Professor Arnold Kim
Professor Michael Scheibner, Advisor

2020

The dissertation of Cameron L. Jennings, titled Spin Coherence and Vibrational Tunneling in Coupled Quantum Dot Pairs, is approved, and it is acceptable in quality and form for publication on microfilm and electronically:

Chair _____ Date _____
Professor Jay Sharping

_____ Date _____
Professor Arnold Kim

Advisor _____ Date _____
Professor Michael Scheibner

University of California, Merced

2020

Dedicated to my wife, Duky.

Table of Contents

List of Symbols

α	Electronic band index (e, h)
$a(a^\dagger)$	Photon annihilation (creation) operator
a_α	Deformation potential
β	Electric polarizability
B	Bottom QD, or bright spin state
$b(b^\dagger)$	Phonon annihilation (creation) operator
$c(c^\dagger)$	Electron/hole annihilation (creation) operator
c	Speed of light in vacuum
c_s	Phonon mode velocity
Δ	Field-induced exciton detuning
D	Dark spin state
$d(d^\dagger)$	Hole annihilation (creation) operator
d	Interdot distance, or direct recombination
d_P	Piezoelectric constant
ϵ	Dielectric constant ($\epsilon_0\epsilon_r$)
ϵ_0	Vacuum dielectric constant
ϵ_r	Relative dielectric constant
$\vec{E}$	Optical electric field
$\mathcal{E}$	Optical electric field amplitude
E	Energy
$\vec{e}$	Photon/photon polarization direction
e	Electron, or elementary electric charge
$\mathcal{F}$	Phonon coupling form factor
F	Electric field, or phonon coupling matrix element
F^+	Entanglement fidelity
Γ	Linewidth, or transition rate
γ	Transition/dephasing rate
g	Crystal ground state, or bulk phonon coupling matrix element
$\hbar$	Reduced Planck constant
H	Hamiltonian
h	Hole
I	Optical PL/PLE intensity
i, j	Bound state orbital index (B, T, $0, 1, 2, \ldots$), or indirect recombination

iX	Indirect (interdot) exciton
iXX	Indirect (interdot, or molecular) biexciton
$\mathcal{J}$	Bessel function of the first kind
J	Exchange interaction matrix element, or total angular momentum, or phonon spectral density
$\vec{k}$	Electron/photon wave vector
k_B	Boltzmann constant
λ	Wavelength
$\mathscr{L}$	Lindblad time evolution superoperator
l	Photon mode index (ω,$\vec{e}$)
$\vec{\mu}$	Optical/electric dipole moment
M	Envelope wavefunction overlap, or time dependence tensor/matrix, or directional dependence of PE phonon coupling
m_0	Free electron rest mass
m_α	Effective mass
n	Population, number operator, or index of refraction
n_B	Bose distribution
ω	Angular frequency
ϕ	Azimuthal coordinate, or phase shift
Ψ	Total wavefunction
ψ	Envelope wavefunction
P	Probability, or laser excitation power, or effective pumping rate
p	Permanent electric dipole moment
$\vec{q}$	Phonon wave vector
q	Electric charge
$\vec{r}$	Position
r	Radial position coordinate
ρ	Density matrix, or lattice mass density
σ, χ	Spin state index ($\uparrow, \downarrow, \Uparrow, \Downarrow$), or transition operator, or standard deviation
S	Singlet spin state, or bright state exchange interaction
s	Phonon mode polarization (LA, TA_1, TA_2)
Θ	Heaviside step function
θ	Polar coordinate
τ	Lifetime
T	Top QD, or triplet spin state, or lattice temperature
t	Interdot tunnel coupling
U	Applied (reverse) bias voltage
u	Bloch wavefunction
V	Coulomb interaction matrix element, or mode volume
W	Optical interaction matrix element
X	Direct (intradot) exciton
XX	Direct (intradot) biexciton
x, y, z	Cartesian coordinates, or alloy composition (x)

List of Abbreviations

AC	Anticrossing	
CB	Conduction band	
CCD	Charge-coupled device	
CQD	Coupled quantum dot pair	
DP	Deformation potential	(phonon coupling mode)
FM	Frank-van der Merwe	(QD growth mode)
HH	Heavy hole	(electronic band)
LA	Longitudinal acoustic	(phonon mode)
LH	Light hole	(electronic band)
LO	Longitudinal optical	(phonon mode)
MBE	Molecular beam epitaxy	
ML	Monolayer	
PE	Piezoelectric	(phonon coupling mode)
PL	Photoluminescence	
PLE	Photoluminescence excitation	
QD	Quantum dot	
SK	Stranski-Krastanov	(QD growth mode)
SPDC	Spontaneous parametric downconversion	
TA	Transverse acoustic	(phonon mode)
VB	Valence band	
VW	Volmer-Weber	(QD growth mode)
ZPL	Zero-phonon line	

List of Figures

List of Tables

Abstract

Spin Coherence and Vibrational Tunneling in Coupled Quantum Dot Pairs

by

Cameron L. Jennings

Doctor of Philosophy in Physics

University of California, Merced, 2020

Professor Jay Sharping, Chair

Quantum dots (QDs) are semiconductor nanoparticles that trap electrons and holes in all three dimensions, resulting in discrete energy levels with strong optical transitions. InAs/GaAs QDs are grown by molecular beam epitaxy of lattice-mismatched InAs on a GaAs substrate, resulting in strain-induced island formation on a two-dimensional wetting layer. In addition to optoelectronic applications such as lasing, infrared detection, and photovoltaics, QDs are capable of hosting optically-controlled spin qubits and emitting photonic qubits for quantum communication and quantum computation.

This dissertation focuses on InAs/GaAs coupled quantum dot pairs (CQDs) formed by strain-induced alignment of QDs in nearby layers, resulting in interdot charge tunneling that can be controlled with an applied electric field. We use a combination of theoretical modeling and optical spectroscopy to understand dynamical processes of bound photoexcited charges, aiming to enhance their usefulness for quantum information and sensing technologies and help overcome difficulties preventing their implementation.

We develop a model of electron and hole confinement in CQDs, including Coulomb and spin interactions, phonon coupling, and optical transitions. This model is used to simulate relaxation dynamics during neutral molecular biexciton cascades, identifying parameter regimes where two-photon polarization entanglement can be expected. While this process has been demonstrated in single QDs, we find that charge separation in interdot states of CQDs allows for tunable emission energies and a higher tolerance to anisotropic electron-hole exchange splitting.

Using low-temperature optical photoluminescence spectrosopy, we identify charge and spin states in single CQDs and investigate their interactions. Two-laser photoluminescence excitation spectroscopy demonstrates two-photon excitation into the molecular biexciton state via a stepwise process, while calculations identify conditions required for efficient simultaneous two-photon absorption. Further investigations find decoherence by electric field fluctuations from charged lattice defects, and identify a novel enhancement of acoustic phonon coupling at hole tunneling resonances from piezoelectric interactions.

Acknowledgements

I thank Dr. Michael Scheibner for his advice and support throughout my nine years of research in his group, which guided my development as a scientist. He encouraged ambitious research projects while allowing me to decide on their implementation, enabling me to fully explore techniques of theoretical modeling, numerical simulation, and automation of data collection and analysis as needed.

I thank Dr. Jay Sharping for teaching me quantum mechanics, optics, and quantum optics, and for encouraging my continued research in these fields. I also thank my entire committee, including Dr. Arnold Kim as well as Dr. Scheibner and Dr. Sharping, for sitting through all of my research presentations and asking challenging questions to guide my investigations.

I thank the current and former members of the Quantum Matter Group for discussing all of my research and providing feedback, and for helping to make the experiments happen. In particular, I would like to thank Dr. Mark Kerfoot for building much of the initial spectroscopy setup, Dr. Cyprian Czarnocki for teaching me how to use it, Dr. Joshua Casara for teaching me useful alignment techniques, Dr. Parveen Kumar for collecting much of the experimental data in Chapter 5, and Mark Woodall for lending me his expert machining and soldering skills.

I thank our collaborators Dr. Samuel Carter, Dr. Allan Bracker, and Dr. Daniel Gammon at the Naval Research Laboratory for developing and fabricating our quantum dot samples, discussing our research regularly, and hosting Cyprian and I at their lab.

I thank my family for their continual support and encouragement throughout my time at UC Merced and before. In particular, my dad, Keith, has enabled my academic advancement since kindergarten, negotiating skipped grades when school was too slow, getting me into college programming classes as early as seventh grade, and sharing his enthusiasm for my progress ever since. My mom, Kim, and stepdad, Joe, enabled my studies by allowing me to live with them through much of my time in Merced, giving me countless rides to campus and back over the years, and supporting me the whole way.

Most of all, I thank my wife Duky for her endless love, support, and encouragement. She dispels my concerns and inspires me to excellence.

Finally, I would like to acknowledge financial support from UC Merced, the Defense Threat Reduction Agency (grant HDTRA1-15-1-0011), and the Air Force Office of Scientific Research (grant FA9550-16-1-0278).

Curriculum Vitae

Cameron L. Jennings

cjennings2@ucmerced.edu

Education

University of California, Merced (Merced, CA)
Ph.D. Physics (3.93 GPA) Fall 2012 - Spring 2020

University of California, Merced (Merced, CA)
B.S. Physics (3.74 GPA) Spring 2010 - Spring 2012

Merced College (Merced, CA)
Undeclared Major Summer 2008, Fall 2009

Mount San Jacinto College (San Jacinto, CA)
Undeclared Major Spring 2005 - Spring 2009

Research Experience

Graduate Researcher Summer 2012 - Spring 2020
University of California, Merced (Merced, CA)
Quantum Matter Group - Dr. Michael Scheibner (PI)

- Theoretically and experimentally investigated phonon-assisted formation of biexciton and charged exciton states in tunnel-coupled pairs of self-assembled semiconductor quantum dots, as well as two-photon transitions and spin-photon entanglement, using a density matrix model and micro-photoluminescence spectroscopy.

Visiting Graduate Researcher Summer 2015
Naval Research Laboratory (Washington, DC)
Electronics Science and Technology Division - Dr. Daniel Gammon (PI)

- Performed photoluminescence spectroscopy to characterize semiconductor samples with quantum dots in photonic crystal cavity membranes and distributed Bragg reflector structures.

Undergraduate Researcher Fall 2011 - Spring 2012
University of California, Merced (Merced, CA)
Quantum Matter Group - Dr. Michael Scheibner (PI)

- Researched the use of magnetic flux vortices in a mixed-state niobium foil (a type II superconductor) as potential wells to form quantum dots in an adjacent semiconductor layer.

Publications

P. Kumar*, C. Jennings*, M. Scheibner, A. S. Bracker, S. G. Carter, and D. Gammon, *Spectral broadening of optical transitions at tunneling resonances in InAs/GaAs coupled quantum dot pairs*, Submitted for publication (2020)
* These authors contributed equally.

C. Jennings, X. Ma, T. Wickramasinghe, M. Doty, M. Scheibner, E. Stinaff, and M. Ware, *Self-assembled InAs/GaAs coupled quantum dots for photonic quantum technologies*, Adv. Quantum Tech. **3**, 1900085 (2019)

C. Jennings and M. Scheibner, *Entanglement dynamics of molecular exciton states in coupled quantum dots*, Phys. Rev. B **93**, 115311 (2016)

C. Czarnocki, M. L. Kerfoot, J. Casara, A. R. Jacobs, C. Jennings, and M. Scheibner, *High resolution phonon-assisted quasi-resonance fluorescence spectroscopy*, J. Vis. Exp. **112**, e53719 (2016)

M. Scheibner, S. Economou, I. Ponomarev, C. Jennings, A. Bracker, and D. Gammon, *Two-photon absorption by a quantum dot pair*, Phys. Rev. B **92**, 081411(R) (2015)

Conference Presentations

C. Jennings, P. Kumar, C. Czarnocki, A. Bracker, S. Carter, D. Gammon, and M. Scheibner, *Charge noise in InAs/GaAs coupled quantum dot devices*
APS March Meeting (Los Angeles, CA) Mar. 2018

C. Jennings, P. Kumar, C. Czarnocki, A. Bracker, S. Carter, D. Gammon, and M. Scheibner, *Charge noise in InAs/GaAs coupled quantum dot devices* (Poster)
APS Far West Section Meeting (Merced, CA) Nov. 2017

C. Jennings, M. Scheibner, *Two-photon transitions in coupled quantum dots* (Invited)
EMN Meeting on Quantum Communication and Quantum Imaging
(Berlin, Germany) Aug. 2016

C. Jennings, A. Jacobs, and M. Scheibner, *Entanglement dynamics of molecular exciton states in coupled quantum dots* (Poster)
International Conference on Modulated Semiconductor Structures
(Sendai, Japan) July 2015

C. Czarnocki, C. Jennings, M. Kerfoot, J. Casara, A. Jacobs, A. Bracker, S. Carter, D. Gammon, and M. Scheibner, *Phonon and strain measurements for quantum-enhanced motion sensing using entangled spins in quantum dots* (Joint Poster)
DTRA Basic Research Technical Review (Springfield, VA) July 2015

C. Jennings, A. Jacobs, and M. Scheibner, *Entangled photon generation in an asymmetric quantum dot molecule* (Poster)
MRS Electronic Materials Conference (Santa Barbara, CA) June 2014

C. Jennings, A. Jacobs, and M. Scheibner, *Entangled photon pairs via two-photon transitions in a quantum dot molecule*
APS March Meeting (Denver, CO) Mar. 2014

Chapter 1

Introduction

In the solid state, semiconductor materials (such as Si, GaAs, InAs, AlAs, etc.) support a series of continuous electronic bands with a band gap around the Fermi level, resulting in a filled valence band and unfilled conduction band under equilibrium conditions. Over the course of the last century, advances in semiconductor electronics have led to unprecedented technological development. By layering different semiconductors and/or intentionally doping them with impurity atoms, heterostructures can be grown with precisely-engineered band structures. The development of solid-state electronic devices such as diodes and transistors has enabled a multitude of applications which now power the modern world: communication, information processing and storage, photodetection, sensing, light emission, and solid-state lasing, to name a few.

The ever-increasing speed and capacity of such devices is primarily achieved by miniaturizing the basic components to fit more of them on a smaller integrated chip. The ultimate limits of this miniaturization are nanostructures which confine electrons quantum mechanically, on a length scale smaller than their spatial extent (35 nm for excitons in InAs). Full three-dimensional confinement is realized in quantum dots (QDs), which can be fabricated in a monolithic planar geometry by epitaxial deposition of atomic layers on a lattice-mismatched substrate (e.g. InAs on a GaAs substrate) to form strain-induced islands on a two-dimensional wetting layer. While other fabrication methods exist, such as chemical synthesis of colloidal nanoparticles, epitaxially-grown QDs are particularly well-suited to integration in optoelectronic devices as photoemitters, photodetectors, or other sensing elements.

Applications are being developed for QDs which leverage their unique capabilities, including **generation of useful quantum light** (e.g. entangled photon pairs) and **sensitive detection of the solid-state environment** (e.g. electric field, lattice strain). Here we focus primarily on epitaxial InAs/GaAs dots grown by molecular beam epitaxy. While InAs/GaAs QDs must be kept at cryogenic temperatures (< 100 K) to prevent significant thermal broadening and carrier escape, they show strong, stable optical transitions between exciton ground states in the near-infrared wavelength range ($900 - 1200$ nm). In addition, dot size and density can be precisely controlled by modifying growth parameters, individual dots can be

addressed using lithographically-defined apertures, and dots can easily be integrated in electrical diodes or photonic cavity structures.

As a result of their discrete energy levels with strong optical transitions, QDs have been used to enhance existing optoelectronic and sensing technologies.[2, 3, 4] QDs have been used as gain elements in lasers, achieving electrically-pumped room-temperature emission at various wavelengths (including 1.31 μm and 1.55 μm emission for fiber-based telecommunications applications) with lower threshold current density, longer operation lifetime, and better temperature stability than quantum well-based lasers.[5, 6] QDs have been used as absorptive elements in infrared photodetectors operating in the $1-12$ μm wavelength range, achieving higher-temperature operation (up to ~ 80 K) than comparable quantum well detectors, but lower responsivity than quantum well or commercial $Hg_xCd_{1-x}Te$ detectors. QDs have been investigated for intermediate-band solar cell applications, though theoretically predicted efficiency enhancements have not yet been attained. QDs have shown promise in electronic memory applications with hole storage times of 1.6 s at room temperature [7, 8], and have been used for electric field sensing with a fiber-coupled scanning probe [9] and lattice strain sensing with driven mechanical resonators [10, 11].

QDs can also be used for quantum information applications such as quantum computation or quantum communication, with data represented as the state of a localized spin qubit or an emitted photonic qubit.[12, 13, 7, 14, 15] Localized qubits can be implemented using the spin state of a bound electron, hole, or electron-hole pair in an optically dark state, with coherent control by pulsed optical excitation. QDs can emit single photons on-demand by pulsed optical or electrical pumping of neutral exciton states, with high single-photon purity and brightness when coupled to an optical cavity or microlens structure.[16] Electrically-pumped single-photon emission at room temperature has also been achieved using InGaN QDs.[17] Neutral biexciton states can be generated by optical or electrical pumping, resulting in emission of polarization-entangled photon pairs after cascaded recombination.[18, 19, 20]

QDs can be stacked during growth to form coupled quantum dot pairs (CQDs), with two QDs separated by a thin ($\sim 2-15$ nm) barrier to allow trapped charges to tunnel between them. This results in a larger variety of accessible states with different spatial configurations of bound charges. In particular, CQDs support interdot states with charges separated between QDs, resulting in a high degree of tunability when an electric field is applied during operation.

CQDs offer several advantages for quantum information applications as a result of charge separation in interdot states.[21] Electric field control allows tuning of photon energies from interdot states, as well as magnetic field coupling strength, exchange coupling strength, and radiative recombination rate. Two spin qubits can be stored in separate QDs, allowing execution of single- or two-qubit logic gates by pulsed laser excitation.[22] The possibility of generating extended entanglement in two-dimensional cluster states of sequentially-emitted photons has also been theoretically predicted.[23, 24]

Since the size and composition of QDs and CQDs can be modified during growth, external electric or magnetic fields can be applied as needed, and optical spectroscopy can sensitively probe charge confinement and interactions, these systems constitute an ideal test bed for studying the behavior and interactions of individual charged particles trapped in a semiconductor environment. By advancing our understanding of CQDs, we hope to enhance their usefulness for quantum information and sensing technologies and help overcome difficulties preventing their implementation.[21]

This dissertation focuses on InAs/GaAs CQDs, using a combination of theoretical modeling and optical spectroscopy to understand dynamical processes of bound photoexcited charges. In particular, we use simulations to investigate the generation of polarization-entangled photon pairs from a two-step cascaded emission process requiring undisturbed coherent evolution of spin states. We also investigate two particular mechanisms by which coherent evolution is interrupted, with combined experimental and theoretical studies identifying a fluctuating local charge environment and a novel enhancement of phonon coupling near tunneling resonances.

Chapter 2 develops the theoretical model used to understand the CQD system and interpret the remainder of the research, starting with a description of electronic conduction and valence bands in bulk semiconductors. A model of QD confinement is then described and used to calculate energies and wavefunctions of bound electrons and holes, followed by an explanation of interactions between multiple bound particles and between bound particles and external electric fields. This finally leads to a model of optical interactions and the calculation of absorption and emission spectra. Portions of this model were published as part of a review of quantum technology applications using CQDs [21].

Chapter 3 describes the growth process used to fabricate the CQD samples and the structure of the samples presented in this dissertation. The various procedures used to perform optical spectroscopy on individual CQDs is described with potential variations, followed by an analysis of bias-dependent spectroscopy guided by the theoretical model and the description of a laser-scanning absorption spectroscopy technique.

Chapter 4 details a method to obtain polarization-entangled photon pairs from the radiative cascade of a neutral biexciton state in a CQD. A model of coherent spin evolution in the presence of relaxation processes is described, with numerical simulations of the fidelity of photon entanglement as a function of temperature and electric field. This work was published in Physical Review B [25]. Calculations of the two-photon absorption process needed to generate the initial biexciton state are then presented, followed by experiments verifying absorption into the biexciton state under two-laser excitation.

Chapter 5 discusses two types of decoherence processes observed experimentally. First, local electric field fluctuations due to charge-trapping lattice defects are seen to cause line wandering and broadening of optical transitions, with the method verified by a series of Monte Carlo simulations. Second, phonon-assisted transitions

between bound states are observed, with a novel phonon coupling enhancement observed at tunneling resonances and reproduced in numerical simulations. This second study was compiled into a manuscript, and is currently under peer review [26].

Chapter 6 concludes by summarizing the theoretical and experimental findings of the preceding chapters, with suggested directions of future research relating to each project. Appendix A lists all possible CQD charge configurations and their allowed spin states for the case of neutral and ± 1 charged states with up to two electron-hole pairs for the case of hole tunneling only. Appendix B lists the values of material and structural parameters used in numerical simulations.

Chapter 2

Theory of Optical Transitions in CQDs

2.1 Electronic Band Structure

Under Stranski-Krastanov (SK) epitaxial crystal growth, InAs quantum dots (QDs) grown on a GaAs (001) substrate form on top of a wetting layer driven by strain from the lattice mismatch of 6.7% between the two crystal lattices. The InAs wetting layer and the QD islands introduce both a localized strain field and a confinement potential for excited electrons and holes due to the smaller band gap energy of InAs relative to GaAs. QDs formed by strain-induced SK growth tend to self-assemble into lens- or pyramid-shaped islands with faceted surfaces[27, 7] protruding from a planar wetting layer when more than 1.5 monolayers of InAs is deposited on a GaAs substrate.[28] The indium-flush technique is often used to precisely control QD height through partial capping and annealing, producing flat QDs whose shape resembles a disk, truncated lens, or truncated pyramid.[29, 1, 30] In addition, indium migration during growth leads to a nonuniform profile of alloy composition, with a higher indium concentration in the center of each QD forming an inverted cone or trumpet distribution.[31, 32, 33, 34, 35]

Coupled quantum dot pairs (CQDs) are formed by depositing a second QD layer on top of the first, with a tunneling barrier layer in between. The strain fields due to QD formation in the first layer cause vertical alignment with QDs in the second and any subsequent layers,[36, 37, 38, 39] though some degree of lateral misalignment is often present in vertically-coupled QD pairs.[40] This strain field also results in an asymmetry in the QD height and lateral width even under nominally identical growth conditions for each layer, with the top QD in a pair being generally wider and thinner than the bottom QD.[29, 30]

The equilibrium strain distribution in a given CQD nanostructure can be found by varying the atomic displacements to minimize the total elastic energy. This minimization is often performed numerically using the continuum elasticity model, achieving a satisfactory description comparable to atomistic valence force field or pseudopo-

tential methods with considerably less computational complexity, and with a clear connection to elasticity parameters measured accurately in bulk materials.[41, 42, 43] Within the continuum elasticity model, the strain distribution is defined as

$$\varepsilon_{ij}(\vec{r}) = \frac{1}{2}\left(\frac{du_i(\vec{r})}{dr_j} + \frac{du_j(\vec{r})}{dr_i}\right) \tag{2.1}$$

in terms of the atomic displacement field $\vec{u}(\vec{r})$, with derivatives calculated as finite differences within a symmetrization scheme averaging over each direction. With an $In_xGa_{1-x}As$ alloy composition distribution described by $x(\vec{r})$ (where $x = 0(1)$ corresponds to GaAs (InAs)), the total elastic energy to be minimized can be expressed as[42]

$$\begin{aligned} E_e = \int dV \Big[&\frac{1}{2}C_{11}(\varepsilon_{xx}^2 + \varepsilon_{yy}^2 + \varepsilon_{zz}^2) + \frac{1}{2}C_{44}(\varepsilon_{yz}^2 + \varepsilon_{xz}^2 + \varepsilon_{xy}^2) \\ &+ C_{12}(\varepsilon_{yy}\varepsilon_{zz} + \varepsilon_{xx}\varepsilon_{zz} + \varepsilon_{xx}\varepsilon_{yy}) - x(\vec{r})(C_{11} + 2C_{12})(\varepsilon_{xx} + \varepsilon_{yy} + \varepsilon_{zz})\varepsilon_0\Big], \end{aligned} \tag{2.2}$$

where C_{ij} are the components of the elastic stiffness tensor and the last term accounts for the intrinsic strain $\varepsilon_0 = (a_{InAs} - a_{GaAs})/a_{GaAs}$ due to mismatched lattice constants when represented in the coordinates of the GaAs barrier. The elastic stiffness varies with material, and can be linearly interpolated with the composition as $C_{ij}(\vec{r}) = C_{ij}^{GaAs} + x(\vec{r})(C_{ij}^{InAs} - C_{ij}^{GaAs})$.

Due to the lack of inversion symmetry in InAs and GaAs, shear strain induces a piezoelectric polarization field. Including linear and quadratic contributions, this field can be expressed in the case of zinc-blende lattices as [44, 45, 46]

$$\vec{P}(\vec{r}) = 2e_{14}\begin{pmatrix}\varepsilon_{yz}\\ \varepsilon_{xz}\\ \varepsilon_{xy}\end{pmatrix} + 2B_{114}\begin{pmatrix}\varepsilon_{xx}\varepsilon_{yz}\\ \varepsilon_{yy}\varepsilon_{xz}\\ \varepsilon_{zz}\varepsilon_{xy}\end{pmatrix} + 2B_{124}\begin{pmatrix}\varepsilon_{yz}(\varepsilon_{yy}+\varepsilon_{zz})\\ \varepsilon_{xz}(\varepsilon_{xx}+\varepsilon_{zz})\\ \varepsilon_{xy}(\varepsilon_{xx}+\varepsilon_{yy})\end{pmatrix} + 4B_{156}\begin{pmatrix}\varepsilon_{xy}\varepsilon_{xz}\\ \varepsilon_{xy}\varepsilon_{yz}\\ \varepsilon_{xz}\varepsilon_{yz}\end{pmatrix}, \tag{2.3}$$

where e_{14} and B_{ijk} are the material-dependent linear and quadratic piezoelectric coefficients, respectively. From this polarization, the piezoelectric charge distribution can be calculated using Gauss's law as $\rho_p(\vec{r}) = -\vec{\nabla}\cdot\vec{P}(\vec{r})$, leading to a piezoelectric potential

$$V_p(\vec{r}) = \frac{1}{4\pi\epsilon_0\epsilon_r}\int d^3\vec{r}\,' \frac{\rho_p(\vec{r}\,')}{|\vec{r} - \vec{r}\,'|} \tag{2.4}$$

acting on bound charges. This piezoelectric potential can be significant in QDs with a pyramidal or otherwise faceted shape, but is not present in an axially symmetric structure due to the lack of shear strain.

Electronic excitations can be described using several approaches with varying degrees of complexity, including the single-band effective mass approximation, multiband $\vec{k}\cdot\vec{p}$ methods, or atomistic tight-binding and pseudopotential methods.[47, 48]

The single-band effective mass model is the simplest approximation, and describes much of the essential physics of confined charges in QDs by treating the lowest energy conduction and heavy hole valence bands independently. Near the center of the Brilluoin zone where the wave vector $\vec{k} = 0$, each band labeled by $\alpha = (e, h)$ shows a parabolic energy dispersion described by an effective mass m_α. The effective mass of each band is anisotropic, with a value of $m_{\alpha,z}$ in the [001] direction and $m_{\alpha,r}$ in perpendicular directions, though this anisotropy is much weaker for the conduction band and is often neglected.[47] In this single-band model, the wavefunction for each particle in the i'th bound state with spin σ is written as $\Psi^\alpha_{i\sigma}(\vec{r}) = \psi^\alpha_i(\vec{r})u^\alpha_\sigma(\vec{r})$ in terms of lattice-periodic zone-center Bloch wavefunctions $u^\alpha_\sigma(\vec{r})$ and envelope wavefunctions $\psi^\alpha_i(\vec{r})$ which vary slowly compared to the lattice spacing. The single-particle energies E^α_i and envelope wavefunctions $\psi^\alpha_i(\vec{r})$ are found by solving the Schrödinger equation

$$\left[-\frac{\hbar^2}{2}\vec{\nabla}\frac{1}{m_\alpha(\vec{r})}\vec{\nabla} + V_\alpha(\vec{r})\right]\psi^\alpha_i(\vec{r}) = E^\alpha_i\psi^\alpha_i(\vec{r}) \tag{2.5}$$

for each band, where $V_\alpha(\vec{r})$ is the confinement potential including band offset, strain-induced shifts, and the piezoelectric potential, and the symmetric ordering of derivatives ensures continuity with a spatially varying effective mass.[49, 50] Note that the energies E^h_i of bound holes are defined such that a lower energy state is closer to the band edge and more strongly confined. With this convention, the confinement potentials are given by [51, 42, 48]

$$\begin{aligned} V_e(\vec{r}) &= V_{CB}(\vec{r}) + a_c(\varepsilon_{xx} + \varepsilon_{yy} + \varepsilon_{zz}) + V_p(\vec{r}) \\ V_h(\vec{r}) &= V_{VB}(\vec{r}) - a_v(\varepsilon_{xx} + \varepsilon_{yy} + \varepsilon_{zz}) - \frac{b}{2}(\varepsilon_{xx} + \varepsilon_{yy} - 2\varepsilon_{zz}) - V_p(\vec{r}), \end{aligned} \tag{2.6}$$

where V_{CB} (V_{VB}) is the unstrained conduction (valence) band edge energy and a_c, a_v, and b are deformation potentials.

The multiband $\vec{k}\cdot\vec{p}$ method incorporates the effects of coupling between bands and has often been used to successfully explain experimental observations with minimal computational complexity compared to atomistic methods. In this method, the wave function of a bound carrier is expressed as a superposition of N Bloch wavefunctions $\Psi_i(\vec{r}) = \sum_n \psi_{i,n}(\vec{r})u_n(\vec{r})$ with envelope wavefunction components $\psi_{i,n}(\vec{r})$. The energies and envelope wavefunctions are found by solving the Schrödinger equation for the coupled bands.[51, 47] The matrix elements of the Hamiltonian are expressed in the chosen basis of Bloch wavefunctions $u_n(\vec{r})$ and evaluated by integrating over a unit cell. The resulting matrix equation can be expressed in the eight-band basis consisting of one conduction band $|s\rangle$ with an s-like atomic orbital and three valence bands $|x\rangle$, $|y\rangle$, and $|z\rangle$ with p-like orbitals, each with two spin states $|\uparrow\rangle$ and $|\downarrow\rangle$. The spin-orbit interaction couples valence bands with different spin and orbital degrees of freedom, and is diagonalized by a unitary transformation to the eigenstates $|j, m\rangle$ of the total angular momentum operators J^2 and J_z. In this basis, the resulting bands

can be classified as electron $\left|\frac{1}{2},\pm\frac{1}{2}\right\rangle$, heavy hole (HH) $\left|\frac{3}{2},\pm\frac{3}{2}\right\rangle$, light hole (LH) $\left|\frac{3}{2},\pm\frac{1}{2}\right\rangle$, and split-off $\left|\frac{1}{2},\pm\frac{1}{2}\right\rangle$, where the split-off band is 340 (380) meV away from the valence band edge in bulk GaAs (InAs), with similar values in QD structures.[51]

When analyzing the dynamics of ground states relevant for coherent processes, the coupling to distant bands is expected to have little impact. As a result, a four-band model described by Luttinger and Kohn[52] is often used to describe valence band coupling between HH and LH bands, with modifications due to strain described by Bir and Pikus[53] and the conduction band treated independently. In the four-band basis $|m\rangle = \left\{\left|\frac{3}{2}\right\rangle, \left|\frac{1}{2}\right\rangle, \left|-\frac{1}{2}\right\rangle, \left|-\frac{3}{2}\right\rangle\right\}$, the valence band Hamiltonian is [51, 54]

$$H_h = E_v(\vec{r})\mathcal{I} - \begin{pmatrix} P+Q & -S & R & 0 \\ -S^* & P-Q & 0 & R \\ R^* & 0 & P-Q & S \\ 0 & R^* & S^* & P+Q \end{pmatrix}, \tag{2.7}$$

where $E_v(\vec{r})$ is the unstrained valence band edge energy with identity matrix $\mathcal{I}$, and the remaining terms describe coupling to wave vector and strain with a similar form:

$$\begin{aligned} P =& \frac{\hbar^2}{2m_0}\gamma_1(k_x^2+k_y^2+k_z^2) - a_v(\varepsilon_{xx}+\varepsilon_{yy}+\varepsilon_{zz}) \\ Q =& \frac{\hbar^2}{2m_0}\gamma_2(k_x^2+k_y^2-2k_z^2) - \frac{1}{2}b(\varepsilon_{xx}+\varepsilon_{yy}-2\varepsilon_{zz}) \\ R =& \frac{\hbar^2}{2m_0}\sqrt{3}\left[-\gamma_2(k_x^2-k_y^2)+2i\gamma_3 k_x k_y\right] + \frac{\sqrt{3}}{2}b(\varepsilon_{xx}-\varepsilon_{yy}) - id\varepsilon_{xy} \\ S =& \frac{\hbar^2}{2m_0}2\sqrt{3}\gamma_3(k_x-ik_y)k_z - d(\varepsilon_{xz}-i\varepsilon_{yz}), \end{aligned} \tag{2.8}$$

where γ_1, γ_2, and γ_3 are Luttinger parameters, and a_v, b, and d are deformation potentials coupling to hydrostatic, biaxial, and shear strain, respectively. The $\vec{k}$-dependent terms are present in bulk semiconductors with cubic symmetry, leading to degenerate valence bands when $\vec{k}=0$. InAs QDs typically have a large compressive biaxial strain, which can split the HH and LH bands by 100-200 meV.[55, 47] HH-LH coupling is mediated by shear strain or unequal lateral strain components, leading to a ground state with 3-14% LH composition depending on QD shape and size.[45] Since the hole ground states are primarily composed of HH bands, their spin states can be labeled as $|\Uparrow\rangle$ ($|\Downarrow\rangle$), corresponding to $m=\frac{3}{2}\,(-\frac{3}{2})$ with a small $m=-\frac{1}{2}\,(\frac{1}{2})$ LH component. For many situations, considering the hole ground states as purely HH with spin $\pm\frac{3}{2}$ is entirely appropriate. However, the richness of the underlying band structure can have observable consequences, such as the partial relaxation of optical selection rules.[40]

Figure 2.1 shows the band energies of strained InAs and unstrained GaAs calculated using the effective mass and multiband $\vec{k}\cdot\vec{p}$ models. We use the intrinsic compressive strain value of 6.7% for InAs lattice-matched to the unstrained GaAs substrate to approximate QD and barrier materials in the absence of strain relaxation.

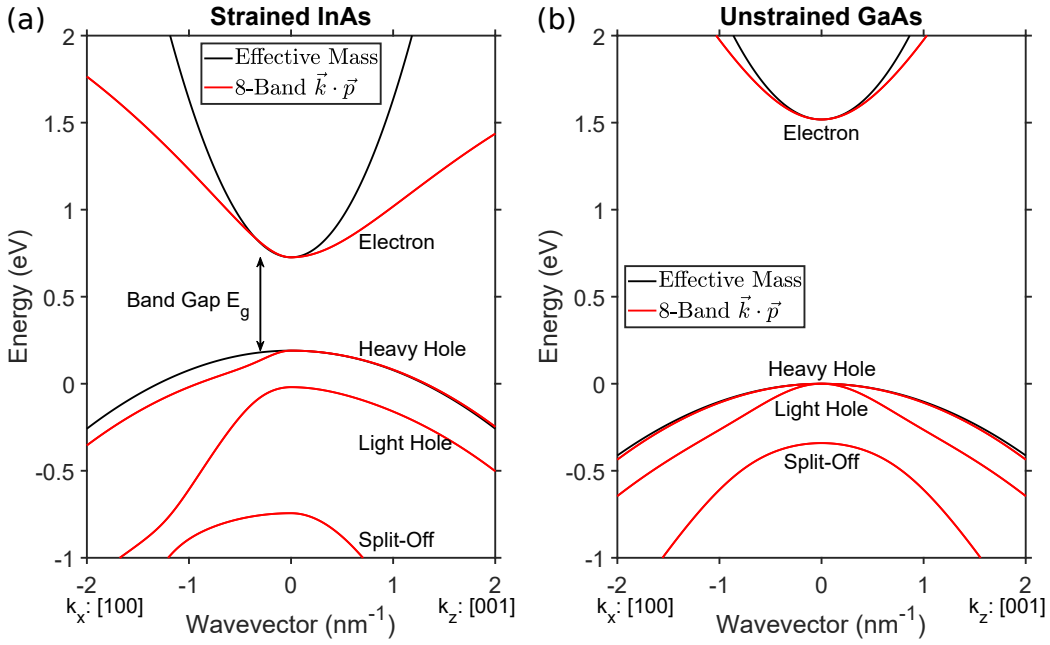

Figure 2.1: Energies of electronic bands for wavevectors along the [100] (x) and [001] (z) directions calculated using the effective mass (black curves) and $\vec{k}\cdot\vec{p}$ (red curves) models, for the case of (a) InAs under 6.7% compressive strain and (b) unstrained GaAs.

The effective mass model is a good approximation for small wavevector values relevant for bound states, though additional deviations occur in the in-plane [100] and [010] directions when an isotropic value of effective mass is used.

2.2 Bound Exciton States

In CQDs, a series of single-particle bound states $|i,\sigma\rangle_\alpha$ are formed with the electron or hole localized in the bottom (B) or top (T) QD, labeled with respect to the growth direction. This gives rise to a variety of potential charge configurations labeled by QD occupancy ${}^{e_B\ e_T}_{h_B\ h_T}X^q$ with total charge q. These states are subject to the Pauli exclusion principle, so that each localized orbital can be populated by a maximum of two electrons or two holes. With two charges in a single orbital, their spin state is restricted to an antisymmetrized singlet state $|S\rangle = (|\uparrow\downarrow\rangle - |\downarrow\uparrow\rangle)/\sqrt{2}$, while a charge in a singly occupied orbital retains its spin degree of freedom.

The multiparticle Hamiltonian can be written in the general form

$$H = H_e + H_h + H_{Coulomb} + H_{exchange} + H_{Stark}(\vec{F}) + H_{Zeeman}(\vec{B}), \qquad (2.9)$$

with each component expressed in the basis of localized single-particle states with annihilation (creation) operators $c_{\alpha i\sigma}$ ($c^\dagger_{\alpha i\sigma}$).

2.2.1 Single-Particle States

The energies and envelope wavefunctions of bound single-electron or single-hole states can be found within the single-band effective mass model by solving the time-independent Schrödinger equation in the form of Eq. 2.5. We model the confinement potential of each QD as a finite well in the growth (z) direction due to strained band-edge offsets between materials, with InAs inside the QD and GaAs outside. We use different effective mass values in each region, matching those measured for pure crystals of each material. Confinement in the lateral ($x-y$) directions is determined by strain-induced self-assembly and is not well-controlled during QD growth, so we model this as a harmonic oscillator with InAs effective mass values and angular frequency ω_α determined by the experimentally measured energy spacing $\hbar\omega_\alpha$ between the ground and first excited states of electrons or holes. To allow for in-plane asymmetry, we introduce a parameter β to scale y-direction confinement to have energy spacing $\beta\hbar\omega_\alpha$. Setting the origin at the center of the QD results in the confinement potential

$$V_\alpha(x,y,z) = \mathcal{E}_\alpha \Theta\left(|z| - \frac{h}{2}\right) + \frac{1}{2} m_\alpha \omega_\alpha^2 (x^2 + \beta^2 y^2), \tag{2.10}$$

where $\mathcal{E}_\alpha$ is the confinement energy due to strained band-edge offset, h is the height of the QD, and $\Theta(x)$ is the Heaviside step function.

Eq. 2.5 can then be solved using separation of variables with

$$\psi^\alpha_{lmn}(x,y,z) = X^\alpha_l(x) Y^\alpha_m(y) Z^\alpha_n(z), \tag{2.11}$$

subject to the boundary conditions that the wavefunction and its slope is continuous at material interfaces and decays to zero far from the QD. The lateral components are determined by the similar differential equations

$$-\frac{\hbar^2}{2m_\alpha}\frac{d^2 X^\alpha_l(x)}{dx^2} = \left(E^\alpha_{x,l} - \frac{1}{2} m_\alpha \omega_\alpha^2 x^2\right) X^\alpha_l(x) \tag{2.12}$$

$$-\frac{\hbar^2}{2m_\alpha}\frac{d^2 Y^\alpha_m(x)}{dx^2} = \left(E^\alpha_{y,m} - \frac{1}{2} m_\alpha \omega_\alpha^2 \beta^2 y^2\right) Y^\alpha_m(y), \tag{2.13}$$

with Hermite-Gaussian solutions being the product of a Hermite polynomial of order l or m and a Gaussian function. Note that references to the effective mass constant m_α use the value for InAs, unless otherwise specified. The wavefunction component in the growth direction is determined by

$$-\frac{\hbar^2}{2}\frac{d}{dz}\left[\frac{1}{m_\alpha(z)}\frac{dZ^\alpha_n(z)}{dz}\right] = \left[E^\alpha_{z,n} - \mathcal{E}_\alpha \Theta\left(|z| - \frac{h}{2}\right)\right] Z^\alpha_n(z), \tag{2.14}$$

with the solutions being a series of symmetric or antisymmetric piecewise functions due to the symmetry and piecewise nature of the confinement potential in this direction. For bound states, the solutions are sinusoidal within the InAs QD region and exponentially decaying within the GaAs barrier region. To enforce continuity of

the full wavefunction $\Psi^{\alpha}_{i,\sigma}(\vec{r}) = \psi^{\alpha}_{i}(\vec{r})u^{\alpha}_{\sigma}(\vec{r})$, the boundary conditions in terms of the envelope wavefunction component $Z^{\alpha}_{n}(z)$ with varying effective mass are expressed as

$$\lim_{z\to(\pm h/2)^-} Z^{\alpha}_{n}(z) = \lim_{z\to(\pm h/2)^+} Z^{\alpha}_{n}(z) \tag{2.15}$$

$$\lim_{z\to(\pm h/2)^-} \frac{1}{m_{\alpha}(z)}\frac{dZ^{\alpha}_{n}(z)}{dz} = \lim_{z\to(\pm h/2)^+} \frac{1}{m_{\alpha}(z)}\frac{dZ^{\alpha}_{n}(z)}{dz}. \tag{2.16}$$

The full solution for bound states of a single QD within this model is

$$\begin{aligned}\psi^{\alpha}_{lmn}(x,y,z) =& A^{\alpha}_{lmn} H_l\left(\sqrt{\frac{m_{\alpha}\omega_{\alpha}}{\hbar}}x\right) H_m\left(\sqrt{\frac{m_{\alpha}\omega_{\alpha}\beta}{\hbar}}y\right) \\ &\times \exp\left[-\frac{m_{\alpha}\omega_{\alpha}}{2\hbar}(x^2+\beta y^2)\right] Z^{\alpha}_{n}(z),\end{aligned} \tag{2.17}$$

where $H_l(x)$ is the Hermite polynomial of order l and the constant A^{α}_{lmn} is determined by the normalization condition $\int |\psi^{\alpha}_{lmn}(\vec{r})|^2\, d^3\vec{r} = 1$. For symmetric solutions, the wavefunction in the growth direction is given by

$$Z^{\alpha}_{n}(z) = \begin{cases} \cos(k_n h/2)e^{-\kappa_n(z-h/2)} & \text{if } z > h/2 \\ \cos(k_n z) & \text{if } |z| \le h/2 \\ \cos(k_n h/2)e^{\kappa_n(z+h/2)} & \text{if } z < -h/2 \end{cases} \tag{2.18}$$

with k_n determined by the transcendental equation

$$\tan\left(\frac{k_n h}{2}\right) = \sqrt{\frac{m_{\alpha,\mathrm{InAs}}}{m_{\alpha,\mathrm{GaAs}}}\left(\frac{k_0^2}{k_n^2}-1\right)} \tag{2.19}$$

obtained from the boundary conditions and the definitions $k_0 = \sqrt{2m_{\alpha}\mathcal{E}_{\alpha}}/\hbar$ and $\kappa_n = \sqrt{m_{\alpha,\mathrm{GaAs}}/m_{\alpha,\mathrm{InAs}}(k_0^2-k_n^2)}$. For antisymmetric solutions, the z-component wavefunction is given by

$$Z^{\alpha}_{n}(z) = \begin{cases} \sin(k_n h/2)e^{-\kappa_n(z-h/2)} & \text{if } z > h/2 \\ \sin(k_n z) & \text{if } |z| \le h/2 \\ -\sin(k_n h/2)e^{\kappa_n(z+h/2)} & \text{if } z < -h/2 \end{cases} \tag{2.20}$$

with k_n determined by the alternate transcendental equation

$$-\cot\left(\frac{k_n h}{2}\right) = \sqrt{\frac{m_{\alpha,\mathrm{InAs}}}{m_{\alpha,\mathrm{GaAs}}}\left(\frac{k_0^2}{k_n^2}-1\right)}. \tag{2.21}$$

The total energy of each bound state is given by

$$E^{\alpha}_{lmn} = E^{\alpha}_{x,l} + E^{\alpha}_{y,m} + E^{\alpha}_{z,n} = \frac{\hbar^2 k_n^2}{2m_{\alpha}} + \hbar\omega_{\alpha}\left[(l+\frac{1}{2}) + \beta(m+\frac{1}{2})\right]. \tag{2.22}$$

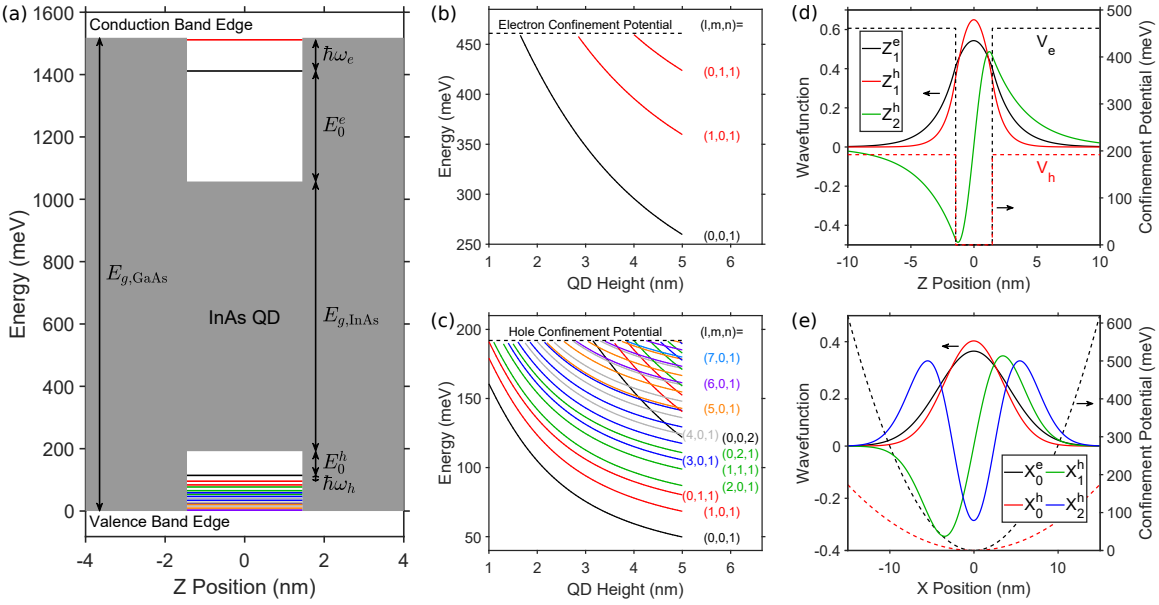

Figure 2.2: (a) Model band edge diagram of a single QD with 2 bound electron states and 17 bound hole states, with relevant energies indicated ($h = 2.9$ nm, $\hbar\omega_e = 100$ meV, $\hbar\omega_h = 18.6$ meV, $\beta = 1.64$). (b) Energy levels of all 3 bound electron states as a function of QD height, with values of (l, m, n) indices indicated. (c) Energy levels of all 32 bound hole states as a function of QD height, with selected values of (l, m, n) indices indicated. (d) Z-component wavefunction of the electron ground state and hole ground and first excited states, with confinement potentials. (e) X-component wavefunction of the electron ground state and hole ground and first two excited states, with confinement potentials.

The x and y indices l and m can take values $0, 1, 2, \ldots$, while the z index $n = 1, 2, 3, \ldots$ labels the solutions to the transcendental equations 2.19 and 2.21 in order of increasing k_n and energy. The three indices (l, m, n) are related to the single index $i = 0, 1, 2, \ldots$ when sorted by increasing energy.

The model confinement potential and solutions for energy levels and wavefunctions are shown in Fig. 2.2. These model calculations use averaged parameter values obtained from a previous study of InAs/GaAs CQDs in a Schottky diode[30], with height $h = 2.9$ nm and hole excited state spacing $\hbar\omega_h = 18.6$ meV corresponding to the bottom QD, asymmetry parameter $\beta = 1.64$ extracted from the top QD, and an estimated value of electron excited state spacing $\hbar\omega_e = 100$ meV. As the QD height increases, the number of electron or hole bound states increases while each of their energies decrease. Many more bound hole states are obtained than electron states as a result of their difference in effective mass ($m_h/m_e = 8.1$ in InAs) and the assumed lateral confinement strengths. The ground state of each wavefunction component is symmetric with a single peak at the center of the QD, while each additional level of excitation introduces a node where the wavefunction crosses zero and the particle is unlikely to be found.

In the laterally symmetric case with $\beta = 1$, the ground state wavefunction can be written in cylindrical coordinates as

$$\psi_0^\alpha(r,\phi,z) = A_0^\alpha \exp\left[-\frac{m_\alpha \omega_\alpha}{2\hbar} r^2\right] Z_1^\alpha(z). \tag{2.23}$$

This expression greatly simplifies the evaluation of integrals for interaction matrix elements between ground states, since the azimuthal coordinate ϕ can be factored out to reduce the dimensionality of the problem.

The wavefunctions given in Eq. 2.17 for a single QD can be used to form CQD wavefunctions in the localized basis, with the electron or hole localized entirely in either the bottom (B) or top (T) QD. With the origin set at the center between the two QDs, localized CQD wavefunctions are given by $\psi_{B/T,i}^\alpha(x,y,z) = \psi_i^\alpha(x,y,z\mp d/2)$ with center-to-center QD separation d and the substitution $h \mapsto h_{B/T}$ to account for the different height of each QD. It is also possible for each QD to have a different lateral confinement strength as a result of strain propagation during growth, which can be included with the substitution $\omega_\alpha \mapsto \omega_{\alpha,B/T}$.

2.2.2 Tunnel Coupling

The single-particle terms of Eq. 2.9

$$H_e + H_h = \sum_{\alpha,i} E_i^\alpha n_{\alpha i} - \sum_{\alpha,\sigma} \sum_{i\in B} \sum_{j\in T} t_{\alpha,ij} (c_{\alpha i\sigma}^\dagger c_{\alpha j\sigma} + c_{\alpha j\sigma}^\dagger c_{\alpha i\sigma}) \tag{2.24}$$

give the energies of isolated charges with number operators $n_{\alpha i} = c_{\alpha i\uparrow}^\dagger c_{\alpha i\uparrow} + c_{\alpha i\downarrow}^\dagger c_{\alpha i\downarrow}$ and the intrinsic interdot tunnel coupling $-t_{\alpha,ij} = \langle B_i,\sigma| H_\alpha |T_j,\sigma\rangle$ due to wavefunction overlap between QDs. As tunnel-coupled energy levels are tuned into resonance, they hybridize to form coherent symmetric and antisymmetric superpositions $(|B_i,\sigma\rangle_\alpha \pm |T_j,\sigma\rangle_\alpha)/\sqrt{2}$ with an energy splitting $\Delta E_{ij} = |2t_{\alpha,ij}|$, resulting in an anticrossing pattern. Since electrons have a much smaller effective mass than heavy holes, they show a significantly larger wavefunction overlap and tunnel coupling energy. Interestingly, in the multiband $\vec{k}\cdot\vec{p}$ model, HH-LH coupling introduces an opposing correction to t_α which can change its sign and result in an antisymmetric ground state above a critical interdot distance.[54, 56]

Tunneling resonances can be observed by applying an electric field in the growth direction to control the relative alignment of energy levels between QDs via the quantum-confined Stark effect. Assuming a constant electric field F in the vicinity of the CQD, an additional term $V_\alpha^F(\vec{r}) = -q_\alpha z F$ is added to the confinement potential of each band with charge $q_{e/h} = \mp e$. This additional term can be included when solving Eq. (2.5) for single-particle eigenstates, or it can be treated as a perturbation up to second order. In either case, the result is a quadratic Stark shift $\Delta E_i^\alpha(F) = -p_{\alpha i}F - \frac{1}{2}\beta_{\alpha i}F^2$ with static dipole moment $p_{\alpha i} = q_\alpha \langle z\rangle_i$ and polarizability $\beta_{\alpha i}$ along the direction of the applied field.[57] The corresponding Hamiltonian

$$H_{Stark}(F) = \sum_{\alpha,i} \Delta E_i^\alpha(F) n_{\alpha i} \tag{2.25}$$

simply modifies the energies of single-particle states. The energy levels in separate QDs are shifted most dramatically by the built-in interdot dipole $p_0 = ed$ due to the distance d between the center of each QD. As a result, interdot exciton states such as ${}^{10}_{01}X^0 \equiv iX^0$ show a strong linear field dependence with negligible polarizability, allowing a high degree of tunability in CQDs compared to single QDs. By controlling the CQD height asymmetry and electric field direction, a given device can be made to exhibit electron and/or hole tunneling resonances.[1]

2.2.3 Multiparticle Interactions

Each pair of particles is coupled through the Coulomb interaction

$$H_{Coulomb} = \frac{1}{2}\sum_{\alpha\beta}\sum_{ijkl}\sum_{\sigma\chi} V^{\alpha\beta}_{ijkl} c^\dagger_{\alpha i\sigma} c^\dagger_{\beta k\chi} c_{\alpha j\sigma} c_{\beta l\chi} \tag{2.26}$$

with matrix elements given by the integral

$$V^{\alpha\beta}_{ijkl} = \frac{q_\alpha q_\beta}{4\pi\epsilon_0\epsilon_r}\iint d^3\vec{r}\, d^3\vec{r}\,' \frac{\psi^{\alpha *}_i(\vec{r})\psi^\alpha_j(\vec{r})\psi^{\beta *}_k(\vec{r}\,')\psi^\beta_l(\vec{r}\,')}{|\vec{r}-\vec{r}\,'|}, \tag{2.27}$$

and a preceding factor of 1/2 to account for double counting as particle indices α and β are varied. The largest contributions are the diagonal terms $V^{\alpha\beta}_{ij} = V^{\alpha\beta}_{iijj}$, which shift the relative energies of multiparticle states and are responsible for the observed energy ordering of excitons with different charge configurations.[58, 59] Off-diagonal terms such as $V^{\alpha\beta}_{ijkk}$ with $i \neq j$ contribute to tunnel coupling between states $|i,\sigma\rangle_\alpha$ and $|j,\sigma\rangle_\alpha$, increasing the tunnel coupling of charged exciton states relative to that of a bare electron or hole.

Electrons and holes are additionally coupled through the pairwise exchange interaction

$$H_{exchange} = \sum_{ijkl}\sum_{\sigma\sigma'\chi\chi'} J^{eh}_{i\sigma,j\sigma',k\chi,l\chi'} c^\dagger_{ei\sigma} c^\dagger_{hk\chi} c_{ej\sigma'} c_{hl\chi'} \tag{2.28}$$

with matrix elements defined similarly to the Coulomb interaction, but with an exchange of spatial coordinates and an additional spin dependence from the Bloch wavefunction components:

$$J^{eh}_{i\sigma,j\sigma',k\chi,l\chi'} = \frac{e^2}{4\pi\epsilon_0\epsilon_r}\iint d^3\vec{r}\, d^3\vec{r}\,' \frac{\Psi^{e*}_{i\sigma}(\vec{r})\Psi^e_{j\sigma'}(\vec{r}\,')\Psi^{h*}_{k\chi}(\vec{r}\,')\Psi^h_{l\chi'}(\vec{r})}{|\vec{r}-\vec{r}\,'|}. \tag{2.29}$$

The exchange interaction can be decomposed into a short-range component with $\vec{r}$ and $\vec{r}\,'$ in the same unit cell of the lattice, and a long-range component with $\vec{r}$ and $\vec{r}\,'$ in different unit cells.[60, 61] The short-range component is typically dominant in QDs, giving a matrix element

$$J^{eh(SR)}_{i\sigma,j\sigma,k\chi,l\chi} = A^{eh}_{\sigma\sigma',\chi\chi'}\int d^3\vec{r}\,\psi^{e*}_i(\vec{r})\psi^e_j(\vec{r})\psi^{h*}_k(\vec{r})\psi^h_l(\vec{r}) \tag{2.30}$$

with the spin-dependent prefactor $A^{eh}_{\sigma\sigma',\chi\chi'}$ determined by integration over the Bloch wavefunctions within a unit cell. The short-range exchange introduces a splitting δ_0 between optically bright states with antiparallel electron and hole spins and optically dark states with parallel spins, as well as a coupling between the dark spin states which forms new eigenstates split by δ_d. The long-range component can be expressed in the form of a dipole-dipole interaction between interband transition dipole moments $\vec{\mu}_{\sigma\chi} = \langle u^e_\sigma | \, \vec{r} \, | u^h_\chi \rangle$, giving the integral

$$J^{eh(LR)}_{i\sigma,j\sigma',k\chi,l\chi'} = \frac{e^2}{4\pi\epsilon_0\epsilon_r} \iint d^3\vec{r}\, d^3\vec{r}\,' \, \psi^{e*}_i(\vec{r})\psi^e_j(\vec{r}\,')\psi^{h*}_k(\vec{r}\,')\psi^h_l(\vec{r}) \times \frac{\vec{\mu}_{\sigma\chi}\cdot\vec{\mu}_{\sigma'\chi'} - 3(\vec{\mu}_{\sigma\chi}\cdot\hat{n})(\vec{\mu}_{\sigma'\chi'}\cdot\hat{n})}{|\vec{r}-\vec{r}\,'|^3} \tag{2.31}$$

with unit vector $\hat{n}$ in the direction of $\vec{r} - \vec{r}\,'$.[60] The long-range exchange introduces a coupling between the bright spin states to form new eigenstates split by δ_b, though this component cancels to zero when the envelope wavefunctions are symmetric in the lateral directions. The effects of the exchange interaction can be succinctly expressed by introducing a hole pseudospin $S_h = \frac{1}{2}$ with S_{hz} eigenstates $\left|\frac{1}{2}\right\rangle = |\Downarrow\rangle$ and $\left|-\frac{1}{2}\right\rangle = |\Uparrow\rangle$, so that electron and hole spin operators are related to the Pauli matrices by $\vec{\sigma}^\alpha = 2\vec{S}_\alpha$. The anisotropic exchange Hamiltonian is then given by

$$H_{exchange} = \frac{\delta_0}{2}\sigma^e_z\sigma^h_z + \frac{\delta_b}{4}(\sigma^e_x\sigma^h_x - \sigma^e_y\sigma^h_y) + \frac{\delta_d}{4}(\sigma^e_x\sigma^h_x + \sigma^e_y\sigma^h_y) \tag{2.32}$$

in terms of the splitting parameters defined above for a single electron-hole pair.[62]

In CQDs, the nature of spin interactions in different charge states is revealed by a characteristic spin fine structure pattern near tunneling resonances. A single-particle state will form a simple anticrossing between states localized in each QD. A neutral exciton state X^0 with one electron and one hole will form a total of four anticrossings between pairs of bright or dark spin states separated by exchange splittings. In a two-electron or two-hole charge state, the singlet spin states are coupled by $\sqrt{2}t_\alpha$ due to spin-conserving tunneling of either indistinguishable particle, while the triplet states remain unaffected. The resulting singlet-triplet splitting, referred to as kinetic exchange, arises solely from a combination of tunneling and the Pauli exclusion principle.[63] In a three-particle trion state, the electron-hole and kinetic exchange interactions combine to produce a more complex pattern.

A comprehensive list of charge configurations and spin states can be found in Table A.1, for states with a total charge $q = 0, \pm 1$, two or less electron-hole pairs, and hole tunneling only, corresponding to the states observed experimentally in samples presented in this report.

2.3 Optical Spectra

Optical transitions can be described by adding an interaction between bound charges and propagating electromagnetic field modes—photons, when treated quantum me-

chanically. The photon interaction Hamiltonian can generally be expressed within the electric dipole approximation as

$$H_{photon} = -\vec{\mu} \cdot \vec{E}(t), \tag{2.33}$$

with electric field $\vec{E}(t)$ and electric dipole moment operator $\vec{\mu} = e\vec{r}$ in terms of electron charge e and position operator $\vec{r}$. For the case of calculating absorption or stimulated emission under monochromatic excitation, the electric field can be treated semiclassically with

$$\vec{E}(\vec{r}, t) = \vec{e}\,\mathcal{E}\cos(\omega t - \vec{k} \cdot \vec{r} + \phi), \tag{2.34}$$

where $\vec{k}$ is the wavevector in the direction of propagation, $\vec{e}$ is the unit vector indicating polarization within the plane perpendicular to $\vec{k}$, $\mathcal{E}$ is the field amplitude, ω is the frequency, and ϕ is the phase shift relative to $t = 0$. For propagation in the $\hat{z}$ direction, the polarization can be expressed in the linear basis with horizontal $\vec{e}_H = \hat{x}$ and vertical $\vec{e}_V = \hat{y}$ components. The polarization can equivalently be transformed to the circular basis, with right-circular $\vec{e}_L = (\hat{x} + i\hat{y})/\sqrt{2}$ and left-circular $\vec{e}_R = (\hat{x} - i\hat{y})/\sqrt{2}$ components which rotate along the $\hat{z}$ direction during propagation.

The maximum spatial extent of a typical CQD system is about 15 nm, as determined by QD size and separation.[30] In comparison, the wavelength in GaAs of photons relevant for QD optical transitions ($\hbar\omega_X \sim 1.25\,eV$) is on the order of $\lambda = 2\pi c/n_{\mathrm{GaAs}}\omega_X = 280\,nm$. Over the extent of the CQD, the magnitude of the sinusoidal fields can change by a factor of 0.58%. We neglect this spatial variation by employing the long-wavelength approximation and evaluating the fields at the midpoint between the QDs, which we take as the origin of the coordinate system.

To analyze spontaneous emission of single photons, the electric field must be regarded as an operator and quantized into modes $l = (\omega_l, \vec{e}_l)$ with frequency ω_l and polarization $\vec{e}_l$, giving[64, 65]

$$\vec{E}(t) = \sum_l i\vec{e}_l\mathcal{E}_l(a_l e^{-i\omega_l t} - a_l^\dagger e^{i\omega_l t}) = \sum_l (\vec{E}_l^{(+)} + \vec{E}_l^{(-)}), \tag{2.35}$$

where a_l ($a_l^\dagger$) is the annihilation (creation) operator of a photon in mode l and $\mathcal{E}_l = \sqrt{\hbar\omega_l/2\epsilon V}$ is the vacuum field amplitude for mode volume V.

The dipole moment operator can be expanded in the basis of electron and hole bound states as

$$\vec{\mu} = \sum_{ij}\sum_{\sigma\chi} \langle i, \sigma|\, e\vec{r}\,|j, \chi\rangle\, (c_{ei\sigma}c_{hj\chi} + c_{ei\sigma}^\dagger c_{hj\sigma}^\dagger). \tag{2.36}$$

The position operator acts most strongly on the lattice-periodic Bloch part of the wavefunctions, giving the expression

$$\langle i, \sigma|\, e\vec{r}\,|j, \chi\rangle \approx \left(\int d^3\vec{r}\,\psi_i^{e*}(\vec{r})\psi_j^h(\vec{r})\right)\left(\frac{1}{\Omega_0}\int_{\Omega_0} d^3\vec{r}\,u_\sigma^{e*}(\vec{r})\, e\vec{r}\,u_\chi^h(\vec{r})\right) = M_{ij}\,\vec{\mu}_{\sigma\chi}, \tag{2.37}$$

where Ω_0 is the volume of a lattice unit cell, M_{ij} is the electron-hole envelope wavefunction overlap, and $\vec{\mu}_{\sigma\chi}$ is the optical dipole moment of the corresponding bulk interband transition.

While Eq. 2.36 in the single-particle basis clarifies the physical mechanism of optical transitions, with an electron-hole pair being either created or destroyed, it is more useful to transform to the basis of multiparticle charge and spin states for the purposes of analyzing CQD optical transitions. In the basis of multiparticle bound states indexed by n, the photon interaction is expressed

$$H_{photon} = \sum_l \sum_{nm} W^l_{nm}(\sigma_{nm} + \sigma_{mn})(a_l e^{-i\omega_l t} - a_l^\dagger e^{i\omega_l t}), \tag{2.38}$$

with interaction matrix element $W^l_{nm} = -i\mathcal{E}_l M_{nm}(\vec{e}_l \cdot \vec{\mu}_{nm})$ and transition operator $\omega_{nm} = |n\rangle \langle m|$ describing a transition from state $|m\rangle$ to state $|n\rangle$ with an additional electron-hole pair.

The symmetry properties of the transition dipole moment integral $\vec{e}_l \cdot \vec{\mu}_{nm}$ lead to the selection rules $\Delta J = 1$ and $\Delta J_z = \pm 1$ for circularly polarized light and $\Delta J_z = 0$ for linearly polarized light. This is simply an expression of angular momentum conservation, since circularly-polarized photons carry angular momentum $(J, J_z) = (1, \pm 1)$ and linearly-polarized photons carry angular momentum $(J, J_z) = (1, 0)$ (represented in units of $\hbar$, as with electrons and holes). Any transition that does not satisfy these selection rules has $W^l_{nm} \propto \vec{e}_l \cdot \vec{\mu}_{nm} = 0$ and is forbidden by the electric dipole interaction, though it could be partially allowed when valence band mixing or higher-order electric or magnetic multipole transitions are considered.

The Hamiltonian of the electron-hole subspace H_0 (Eq. 2.9) introduces an oscillating phase to the transition operators, which can be seen by transforming to the interaction picture $H^I_{photon} = \exp(iH_0 t/\hbar) H_{photon} \exp(-iH_0 t/\hbar)$. The resulting Hamiltonian

$$H^I_{photon} = \sum_l \sum_{nm} W^l_{nm}(\sigma_{nm} e^{i\omega_{nm} t} + \sigma_{mn} e^{-i\omega_{nm} t})(a_l e^{-i\omega_l t} - a_l^\dagger e^{i\omega_l t}), \tag{2.39}$$

with transition frequency $\omega_{nm} = (E_n - E_m)/\hbar > 0$, has multiple terms with widely varying oscillation frequencies. For photons near resonance with the transition frequency $\omega_l \sim \omega_{nm}$, cross-terms with $e^{\pm i(\omega_l + \omega_{nm})t}$ oscillate quickly and average to zero on timescales relevant for optical transitions. We therefore make the rotating-wave approximation by neglecting these terms and keeping only the slowly-oscillating terms to obtain

$$H^{RWA}_{photon} = \sum_l \sum_{nm} W^l_{nm}(\sigma_{nm} a_l e^{-i(\omega_l - \omega_{nm})t} - \sigma_{mn} a_l^\dagger e^{i(\omega_l - \omega_{nm})t}), \tag{2.40}$$

describing photon absorption accompanied by electron-hole pair generation and photon emission accompanied by electron-hole pair recombination.

The absorption rate under quasi-resonant monochromatic excitation can be determined using semiclassical perturbation theory. Assuming that the driving field

is weak, so that the interaction Hamiltonian $H_I = H_{photon}$ is small compared to H_0, the state of the system can be expanded in the numbers of transitions induced by the field. We expect the first-order terms (with one interaction) to dominate the system evolution, while second-order terms can be included to analyze two-photon transitions (as in Section 4.2). To keep track of the different terms of the perturbation, we pull out a small factor λ:

$$H_I = W\cos(\omega t) \equiv \lambda H', \tag{2.41}$$

such that $\lambda \ll 1$ and the elements of H' are the same order of magnitude as H_0.

In the basis of eigenstates $|n\rangle$ of the Hamiltonian, with

$$H_0 |n\rangle = E_n |n\rangle = \hbar\omega_n |n\rangle , \tag{2.42}$$

the state of the system at time t can be written

$$|\psi(t)\rangle = \sum_n \phi_n(t) |n\rangle . \tag{2.43}$$

The time-dependent Schrödinger equation applied to this state then yields

$$i\hbar\frac{d}{dt}|\psi(t)\rangle = (H_0 + \lambda H'(t))|\psi(t)\rangle . \tag{2.44}$$

Now, each coefficient can be expanded in powers of λ as $\phi_k = \sum_{n=0}^{\infty}\lambda^n\phi_k^{(n)}$. Additionally, we factor out evolution under H_0 by replacing each $|n\rangle$ by $e^{-i\omega_n t}|n\rangle$ (equivalent to transforming to the interaction picture in Eq. 2.39) and take an inner product with an arbitrary state $\langle k|$, which gives

$$i\hbar\dot{\phi}_k = \lambda\sum_n \langle k| H' |n\rangle \phi_n(t)e^{i\omega_{kn}t}. \tag{2.45}$$

Collecting terms with similar powers of λ gives a system of differential equations

$$\begin{aligned} i\hbar\dot{\phi}_k^{(0)} &= 0 \\ i\hbar\dot{\phi}_k^{(1)} &= \sum_n \langle k| H' |n\rangle \phi_n^{(0)}(t)e^{i\omega_{kn}t}. \end{aligned} \tag{2.46}$$

With the initial condition $|\psi(t=0)\rangle = |i\rangle$, these equations can be solved iteratively to obtain

$$\begin{aligned} \phi_k^{(0)}(t) &= \delta_{ik} \\ \lambda\phi_k^{(1)}(t) &= \frac{1}{i\hbar}\int_0^t dt'\ \langle k| H' |i\rangle\ e^{i\omega_{kn}t}. \end{aligned} \tag{2.47}$$

With the above considerations, the probability of transitioning from state $|i\rangle$ to state $|k\rangle$ after a time T through one field-induced transition is given by

$$P_{i\to k}^{(1)}(T) = |\langle k|\psi(T)\rangle^{(1)}|^2 = \frac{1}{\hbar^2}\left|\int_0^T dt\, W_{ki}\cos(\omega t)e^{i\omega_{ki}t}\right|^2,$$

with transition matrix elements $W_{ki} = \langle k| W |i\rangle$. Since this probability will only increase with longer interaction times, and transitions between several states must be accounted for, the more interesting quantity to extract is the transition *rate*, defined as the transition probability per unit time. The identity $\cos(\theta) = \frac{1}{2}\left(e^{i\theta} + e^{-i\theta}\right)$ can be used to rewrite the oscillatory terms as complex exponentials. Performing the integration yields a general expression for the transition rate:

$$\Gamma^{(1)}_{i\to k}(T) = \frac{P^{(1)}_{i\to k}(T)}{T} = \frac{1}{T}\frac{|W_{ki}|^2}{4\hbar^2}\left|\frac{e^{i(\omega+\omega_{ki})T}-1}{\omega+\omega_{ki}} - \frac{e^{-i(\omega-\omega_{ki})T}-1}{\omega-\omega_{ki}}\right|^2 \tag{2.48}$$

This expression contains two terms with denominators $\omega \pm \omega_{ki}$, accounting for resonance/antiresonance of the laser with the transition of interest. When one of these resonance conditions (or at least quasi-resonance) is satisfied, that term will dominate the transition (equivalent to applying the rotating wave approximation in Eq. 2.39). If $\omega \approx \omega_{ki}$, the expression simplifies to

$$\Gamma^{(1)}_{i\to k} \approx \frac{1}{T}\frac{|W_{ki}|^2}{4\hbar^2}\frac{\sin^2(\frac{\omega-\omega_{ki}}{2}T)}{\left(\frac{\omega-\omega_{ki}}{2}T\right)^2}T^2 \equiv \frac{1}{T}\frac{|W_{ki}|^2}{4\hbar^2}g_T(\omega-\omega_{ki}). \tag{2.49}$$

As the interaction time $T \to \infty$, the function $g_T(\omega)$ becomes a delta function with amplitude $2\pi T$. Therefore, the transition rate can be written

$$\Gamma^{(1)}_{i\to k} \approx \frac{\pi}{2\hbar^2}\,|W_{ki}|^2\;\delta_T(\omega-\omega_{ki}),$$

where the function $\delta_T(\omega)$ has width $2\pi/T$ and unit area, becoming a δ-function as $T \to \infty$. This is an expression of Fermi's golden rule, where the transition rate due to any interaction with a specified coupling matrix element follows the same general form. Note that $\Gamma^{(1)}_{i\to k} = \Gamma^{(1)}_{k\to i} = \Gamma^{(1)}_{ik}$: a sinusoidal field is equally likely to cause absorption or stimulated emission between two levels.

Real CQD systems are subject to relaxation and decoherence processes, so that the coherent phase decays at a rate $\tilde{\gamma}$. As a result, each transition is broadened from a delta function to a Lorentzian with frequency width $2\tilde{\gamma}$. Ref. [66] uses a single-particle Green's function description of linear susceptibility within the electric dipole and rotating wave approximations to obtain an expression for the optical absorption spectrum as a sum of Lorentzian contributions

$$I_{abs}(\omega) \propto \sum_n |W_{0n}|^2 \frac{\tilde{\gamma}_n(\omega)}{\left(\omega - E_n/\hbar\right)^2 + \tilde{\gamma}_n(\omega)^2}, \tag{2.50}$$

where W_{0n} is the interaction matrix element of transition $|0\rangle \to |n\rangle$. The general expression for the energy linewidth of each exciton state

$$\Gamma_n(\omega) = 2\hbar\tilde{\gamma}_n(\omega) = \hbar\sum_{m\neq n}\gamma_{nm} + \hbar\gamma_{nn}(\omega) \tag{2.51}$$

contains contributions from real transitions to other states as well as virtual single-state transitions associated with phonon-assisted optical absorption, resulting in phonon sidebands around the Lorentzian zero-phonon line (ZPL) and pure dephasing. The frequency-dependent pure dephasing rate is calculated as a phonon-assisted transition rate, with the phonon energy determined by the detuning $\Delta\omega_n = \omega - \omega_n$ of the optical frequency from resonance:

$$\gamma_{nn}(\omega) = \frac{2\pi}{\hbar^2}\left[n_B(T, \Delta\omega_n) + \Theta(\Delta\omega_n)\right] J_{nn}(\Delta\omega_n). \tag{2.52}$$

The optical emission spectrum is also calculated similarly to the absorption spectrum, with only the pure dephasing rates modified by changing the sign of detuning terms $\Delta\omega_n$ to $-\Delta\omega_n$ to reflect the reversal of phonon absorption and emission processes.

Experimentally, the emission spectrum is detected using a spectrometer with a finite resolution. As a result, the detected spectrum is convolved with the typically Gaussian spectrometer response function of width Γ_{spect}, leading to a Voigt ZPL profile with phonon sidebands. In the presence of a fluctuating electric field due to many charged lattice defects near the CQD, an additional Gaussian broadening is present, with a width $\Gamma_{fluct} = \Delta U_{fluct}|\partial E/\partial U|$ proportional to the bias slope of the transition energy $E(U)$. With both of these broadening mechanisms, the combined Gaussian ZPL broadening is given by

$$\Gamma_g = \sqrt{(\Gamma_{fluct})^2 + (\Gamma_{spect})^2}. \tag{2.53}$$

Chapter 3

CQD Growth and Spectroscopy

3.1 CQD Growth

Quantum dots can be grown by molecular beam epitaxy (MBE), a fabrication technique which allows precisely-controlled deposition of atomic layers on the surface of a crystal substrate.[67, 68] By heating solid atomic sources in a vacuum chamber, sublimation produces atomic vapor which can condense on the substrate and crystallize to grow epitaxial layers. Crystal growth conditions can be tuned by controlling the substrate temperature with an attached heating element, and the growth can be monitored *in-situ* using Resonant High-Energy Electron Diffraction. Individual crystal monolayers (MLs) can be deposited with appropriately designed source chambers and automated shutters, at a rate of $1\,\mathrm{ML}$ per $1-5\,\mathrm{s}$. To obtain high-purity epitaxial crystals with minimal contaminants, the growth chamber must be maintained in ultra-high vacuum conditions ($\sim 10^{-10}$ Torr, or 10^{-13} atm). This places a series of stringent requirements on an MBE apparatus, including cryogenic cooling and careful choice of design and materials to prevent outgassing. MBE is therefore an expensive fabrication technique to implement, though its atomic precision coupled with design improvements for higher throughput have led to its widespread use in research and commercial production of high-performance optical and magnetic sensing devices, as well as quantum well lasers and other developing nanotechnology.

The morphology of epitaxial layer growth depends on the relative energy of electrostatic interactions between the deposited layer and substrate surface. When the deposited material is the same as the substrate, or forms a crystalline structure with the same lattice spacing, surface atoms bind much more strongly to the substrate than to each other. Growth then proceeds by sequential crystallization of planar atomic layers covering the substrate, a phenomenon known as Frank-van der Merwe (FM) or layer-by-layer growth. However, when a different material is deposited which has a different lattice spacing than the substrate, strain due to lattice mismatch accumulates at the material interface which counteracts surface adhesion. When deposited atoms

are more strongly bound to each other than to the substrate, this effective surface tension causes nucleation and growth of separate islands across the substrate surface, a growth mode known as Volmer-Weber (VW) or island growth.

Under conditions of small lattice mismatch, such as InAs/GaAs with a 7 % difference in lattice spacing, competition between surface tension and interface strain leads to a combination of FM and VW growth modes. Initial growth takes place by formation of a thin planar wetting layer (WL) on the substrate surface. At a critical WL thickness (1.6 ML for InAs deposited on GaAs), the accumulated strain causes the formation and growth of small islands on the WL surface, a process known as Stranski-Krastanov (SK) or layer-plus-island growth. With properly chosen growth conditions, SK growth produces coherently strained islands free of lattice defects and of sufficiently small size to exhibit three-dimensional quantization of bound charge states. These SK islands constitute self-assembled QDs with strong, discrete optical transitions and relatively homogeneous size distributions.

When multiple QD layers are grown sequentially, separated by tunneling barriers, propagation of lattice strain results in self-alignment of QDs in different layers to form stacks of tunnel-coupled QDs (CQDs).[36, 37, 38, 39] Indium migration during growth typically results in gradually expanding QD sizes as additional layers are deposited. This effect is mitigated by using the indium-flush technique, wherein each QD layer is partially capped and annealed to truncate QDs to a precisely controlled height.[67]

3.2 Sample Structure

The experiments reported in this dissertation were performed on one of four InAs/GaAs CQD samples, each grown in a diode structure on an n-doped substrate with a larger bottom QD to produce hole tunneling resonances as the applied bias is tuned. While many other QD and CQD samples were investigated, we limit the discussion to those with the highest quality data and most extensive analysis for the projects presented here.

Sample A (B) contains two InAs QD layers separated by a 4 nm (6 nm) barrier, embedded in a planar n-type GaAs Schottky diode with interdot hole tunneling. The layer structure is shown in Fig. 3.1(a). A 500 nm n-doped GaAs buffer layer is grown on an n-doped GaAs substrate, with n-type doping achieved by introducing silicon impurities during MBE growth. An 80 nm intrinsic (undoped) GaAs layer is then deposited, followed by two nominally 2.5 nm InAs QD layers separated by a 4 nm (6 nm) GaAs tunnel barrier. Strain propagation and indium migration during growth results in CQD asymmetry, with a slightly thicker (∼2.9 nm) bottom QD and a slightly thinner (∼2.1 nm) top QD [30]. A 230 nm GaAs capping layer is then added, followed by a 40 nm $Al_{0.3}Ga_{0.7}As$ blocking layer, a final 10 nm GaAs layer, and a transparent 8 nm titanium layer as the top Schottky contact. A 120 nm aluminum shadow mask layer is then grown on top, with ∼1 μm apertures etched by electron-beam lithography to allow individual CQDs to be optically addressed without external

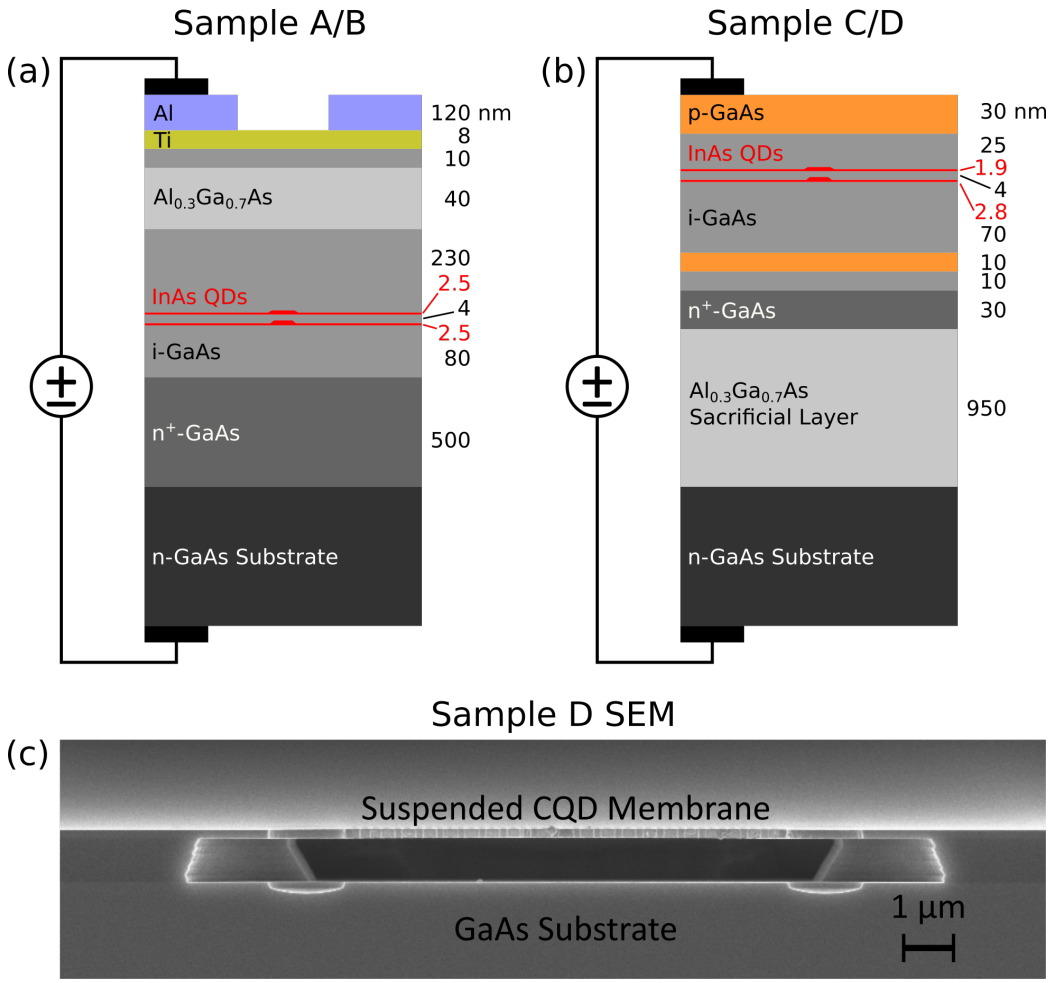

Figure 3.1: Layer structures of samples (a) A and B, and (b) C and D, not drawn to scale. (c) Cross-sectional scanning electron micrograph of a typical suspended membrane structure patterned onto sample D.

spatial filtering.

Sample C and D contain QDs separated by a 4 nm barrier, embedded in a delta-doped nipip diode. The layer structure is shown in Fig. 3.1(b) A 950 nm n-doped $Al_{0.3}Ga_{0.7}As$ buffer layer is grown on an n-doped GaAs substrate, followed by an additional 30 nm n-doped GaAs buffer layer. A 10 nm intrinsic GaAs layer is then grown, following by delta doping with a 10 nm p-doped GaAs layer. Here, p-doping is achieved using beryllium impurity atoms. Another 70 nm intrinsic GaAs layer is grown, followed by the InAs CQD layers with a 2.8 nm bottom QD and 1.9 nm top QD separated by a 4 nm GaAs tunneling barrier. A further 25 nm intrinsic GaAs capping layer is then grown, followed finally by a 30 nm p-doped GaAs top layer to form an nipip diode structure.

Sample C and D are grown identically, while sample D is further patterned by electron beam lithography and inductively coupled plasma etching. This patterning

is followed by an undercut with hydrofluoric acid to remove the sacrificial AlGaAs layer and leave the top layers with CQDs suspended in a nipip diode membrane. The result is a wide array of mechanical resonator structures, including diving-board cantilevers with different lengths ($\sim 5 - 15$ μm) and widths ($\sim 1 - 4$ μm), all with suspended CQD-embedded diode membranes as seen in Fig. 3.1(c).

3.3 Experimental Methods

The most basic requirements of single-CQD spectroscopy are a light source for optical excitation, a high-magnification objective lens to focus excitation light and maximize collection of photoluminescence (PL) emission, and a spectrally-dispersed detection method. We use continuous-wave semiconductor diode lasers for excitation, with most experiments presented here using one of two similar external cavity diode lasers (Toptica DL Pro) with $890 - 980$ nm single-mode output tunable by changing the angle of a motorized grating, and occasional experiments using separate diode lasers fixed at 532 nm or 660 nm for excitation above bulk bandgap energies. We use one of three 20/50/100× infinity-corrected objectives (Mitutoyo M Plan Apo NIR) with high numerical aperture ($NA = 0.4/0.42/0.5$) and long working distance ($WD = 20/17/12$ mm) to collect PL emission into a collimated beam.

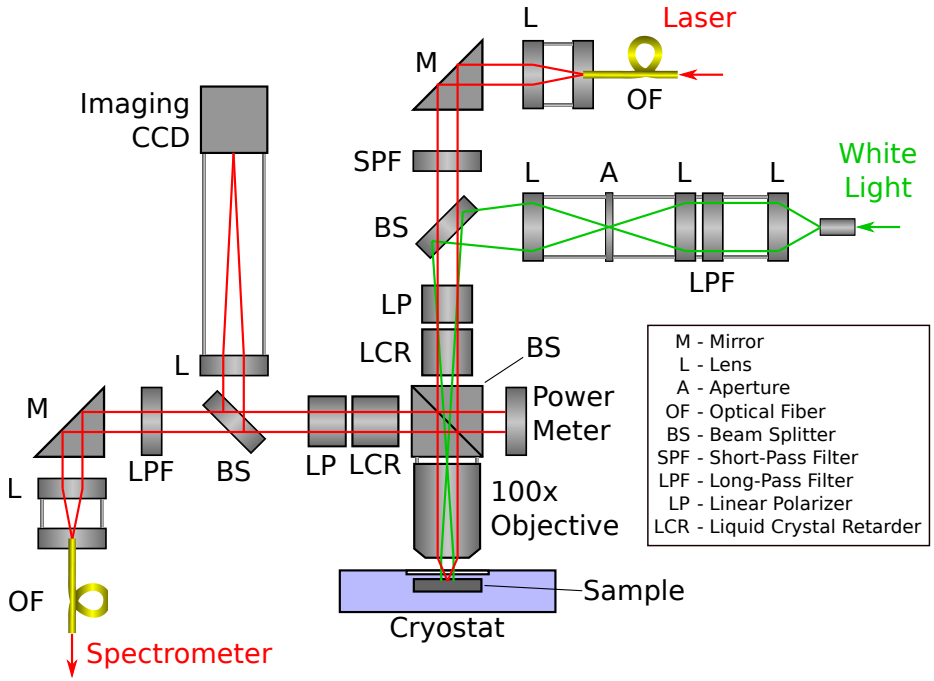

Figure 3.2: Schematic diagram of confocal spectroscopy setup, with fiber-coupled excitation and detection, spectral filtering, polarization control, and white-light imaging capability.

Spectral detection is accomplished using a three-stage spectrometer (Princeton Instruments TriVista) consisting of three Czerny-Turner monochromators with reflective diffraction gratings (900 mm^{-1} or 1100 mm^{-1} groove density) and 750 mm focal length mirrors for collimation and focusing onto a liquid nitrogen-cooled 1340×100 CCD array detector with 20×20 μm pixels (Princeton Instruments Spec-10). The spectrometer can be operated in one of three primary modes:

Single Spec uses only the final monochromator stage to maximize collection efficiency with $80 - 100$ μeV spectral resolution.

Triple Additive uses all three monochromator stages with sequential dispersion to maximize spectral resolution ($25 - 40$ μeV) at the cost of collection efficiency.

Triple Subtractive uses the first and second monochromator stages with opposite dispersion and a narrow exit slit width to minimize stray laser light and the final monochromator stage for dispersion, giving a similar spectral resolution as single spec with a slightly lower collection efficiency.

CQD samples must be cooled to prevent thermal excitation of bound electrons and holes to excited states and maintain narrow ground-state PL linewidths with high intensity. This can be ensured by keeping the temperature T such that the thermal energy k_BT (Boltzmann constant $k_B = 86.2$ μeV/K) is far below the excited state energy splitting $\hbar\omega_\alpha$ ($T \ll 116$ K for $\hbar\omega_h = 10$ meV). In practice we find that ground-state PL transitions can be resolved below ∼80 K, with lower temperatures preferable due to higher intensity and lower linewidth. This is accomplished using a continuous-flow helium cryostat system (Cryo Industries Cryocool G2 with CFM Microscopy Cryostat) capable of maintaining the sample at temperatures as low as 20 K for weeks at a time with a room-temperature supply of helium gas. The sample is held in a high vacuum chamber pumped out to $< 10^{-4}$ mbar using an external turbopump (Pfeiffer HiCube 80 ECO) and mounted with vacuum grease to a copper cold finger in contact with the cooled helium gas stream. The sample chamber has a 1.59 mm-thick quartz window on either side to allow optical access for laser excitation and PL collection, and the connected helium transfer lines are flexible to minimize vibration transfer from the compressor and refrigeration pumps.

Another requirement for single-CQD spectroscopy is the ability to adjust and maintain alignment of all optical components for the duration of an experiment (from ∼1 minute to ∼10 hours depending on scanning parameters). To achieve this, all optical components are attached to a heavy optical table with pneumatic vibration damping on each leg and an array of tapped holes for reconfigurable rigid mounting. Each mirror, beam splitter, and optical fiber coupler is held in a spring-loaded kinematic mount with two-axis thumbscrew control for stable angular and translational alignment of each optical path. The cryostat sample chamber is mounted on two linear translation stages for positioning in the lateral ($x - y$) directions and scanning across the sample surface, while the objective lens is mounted on another linear translation stage for focusing and collimation in the normal (z) direction.

The laser excitation and spectrometer detection beams can be collimated and directed through free space, or coupled through single-mode optical fibers (as in Fig. 3.2) by focusing onto the 5 μm fiber core and re-collimating the output with small anti-reflection-coated aspheric lenses. The fiber-coupled arrangement is convenient for rapid exchange of excitation source or detector without significant misalignment, and the small fiber core acts as a spatial filter limiting PL collection to a $\sim$1.5 μm spot on the sample surface for confocal microscopy. However, cryostat pump vibrations combined with $1-2$ K fluctuations of laboratory room temperature leads to measured sample drift up to 10 μm over minutes or hours, often limiting stable PL collection times to $10-30$ minutes for fiber-coupled confocal microscopy with this cryostat setup. This situation was improved dramatically by switching to a new cryostat (Attocube attoDRY1100) which has a mechanically isolated sample chamber with a low-temperature objective lens and stacked piezoelectric translation stages for *nm*-scale control of sample position in all three dimensions. The new cryostat was installed and made functional within the last year, so most of the long-duration scans presented here were performed using the old cryostat and free-space coupling.

Visual inspection of the sample surface was accomplished by coupling a white light source (Schott KL200) into the excitation path and focusing onto an imaging CCD (Watec WAT-902H2 Ultimate) in the detection path with beam splitters on flip mounts to allow unimpeded PL signal transmission when not in use, with the arrangement shown in Fig. 3.2. The white light excitation is focused onto the back aperture of the objective lens using Köhler illumination, resulting in an unfocused beam at the sample plane for even lighting without forming an image of the light source. Once an individual CQD is identified spectroscopically, visual inspection is used to mark its location on the sample by reference to scratches or other visible surface features so it can be returned to for future study.

The laser wavelength is continuously monitored with a beamsplitter coupling $\sim$5% of the source power into a wavemeter (Bristol 621A), with the laser's internal grating angle tunable in energy steps as small as 80 μeV with motorized positioning and 2 neV with piezoelectric positioning. Wavelength tuning is complicated by occasional instability and hopping between stable output modes of the laser, so that experiments scanning laser wavelength can miss some wavelength ranges where the output could not be stabilized. The laser power is monitored using a power meter (Thorlabs PM100) at the output of a beamsplitter with wavelength-calibrated transmission and reflection spectra so the power transmitted to the sample can be accurately estimated at each wavelength. A series of exchangeable neutral density filters are used for coarse power control, cutting power at all wavelengths by orders of magnitude as needed. When the excitation laser is coupled through an optical fiber, the fiber coupling efficiency can be tuned through careful misalignment to give finer control of transmitted power. Laser output power fluctuations of $\sim$5% were stabilized to $< 0.5\%$ using a liquid crystal variable retarder (Meadowlark LVR-100) in combination with a linear polarizer as a custom power controller, giving stable output with fine automated control over three orders of magnitude. Later experiments replaced

this arrangement with a commercial power controller (Thorlabs NEL03) with better frequency response and lower output fluctuations ($< 0.05\%$).

Since the tunable diode laser can emit over a wide wavelength range, single-mode emission is accompanied by a broad background spectrum with interference due to the many suppressed modes, referred to as sideband emission. For standard nonresonant PL experiments with the laser wavelength ($890 - 920$ nm) far below the expected range of CQD PL wavelengths ($940 - 960$ nm), laser sideband emission can still be strong enough to obscure PL signal in the absence of spectral filtering. The laser sideband emission can be selectively blocked by placing a short-pass filter in the excitation path, set to allow the main laser peak and block any sideband which would interfere with PL detection. The remaining laser light can also interfere with PL detection as stray light within the spectrometer, so this can be prevented by placing a long-pass filter in the detection path to block the main laser peak while allowing as much PL signal as possible. For experiments with the laser and PL wavelengths too close for efficient edge-pass filtering (within $\sim$15 nm), we use the triple-subtractive spectrometer detection mode to block laser light with a narrow transmission cutoff (< 0.5 nm).

The polarization of photons involved in CQD optical transitions is closely related to the exciton spin states, with the intensity of PL with different polarization orientations (left- or right-circular, or linear at some angle) indicating the population of different spin states. The strength of a beam's polarization is quantified by the extinction ratio, the ratio of power transmitted through a polarizer oriented along its polarization axis to the power transmitted through a perpendicularly-oriented polarizer. The laser output is polarized vertically with an extinction ratio of $\sim$5000, and rotated 45° by a Faraday isolator (Thorlabs IO-5-TIS2-HP) to block reflected light and prevent it from destabilizing the laser. The excitation polarization incident on the sample and detection polarization of collected PL is controlled electronically using a linear polarizer and liquid crystal variable retarder on each path (as shown in Fig. 3.2), allowing access to orthogonal linear (vertical/horizontal) and circular (left/right) polarization of each path without requiring realignment. Polarization-maintaining single-mode optical fibers are used to maximize transmission of polarized light for polarization-dependent experiments, while other experiments can use standard single-mode optical fibers with no significant loss.

A cross-polarized configuration can also be used to help block laser sideband emission in near-resonant PL experiments, with polarized excitation and oppositely-polarized detection. Earlier experiments use a side-incidence geometry with the excitation beam focused onto the sample at a 45° angle with a separate 50 mm lens to minimize scattered laser light collected into the spectrometer, but we found that depolarization from angled glass interfaces reduces the extinction ratio to $\sim$10 and prevents cross-polarized sideband suppression. Near-resonant PL experiments are made possible by using normal incidence (as shown in Fig. 3.2) with cross-polarized detection, and ensuring a slight misalignment between excitation and detection paths to prevent collection of specular reflections.

Finally, an electric field is applied to diode-embedded CQDs by mounting the sample in a ceramic chip header with electrical contact to the top and bottom conductive layers. The electric field strength is controlled using a sourcemeter (Keithley 2611A) to apply a bias voltage across the sample with electrical feedthrough lines into the sample chamber and measure the resulting current. Device parameters and measurements are monitored and controlled during experiments using a graphical programming software (LabVIEW) installed on a computer connected to each device by USB (or RS232 serial connection converted to USB). Earlier experiments use a simple looped sequence to change parameters and record the resulting data, with the most common experiment measuring the PL spectrum as a function of applied bias voltage. Later improvements extended this functionality to establish a standard format (queued state machine) for parallel control of multiple instruments, allowing continuous control during experiments (e.g. stabilization of laser power), remote control of devices connected to different computers, and simplified installation and usage of new devices.

3.4 Photoluminescence Spectroscopy

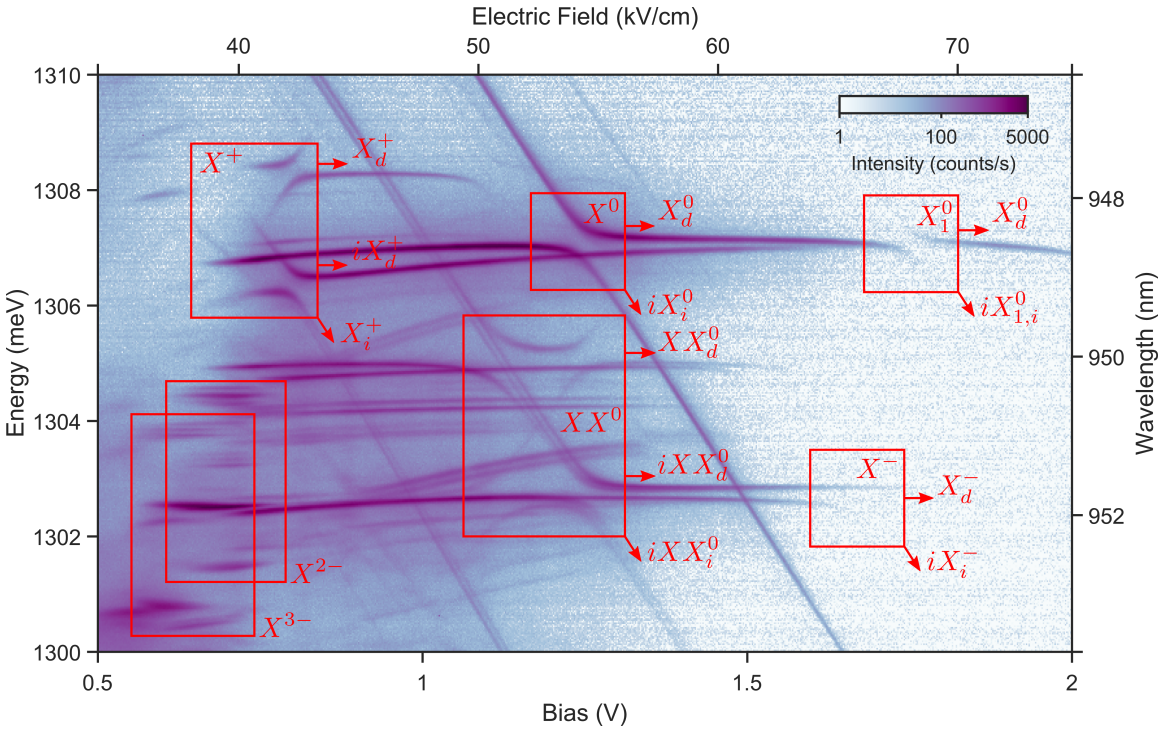

Figure 3.3: Photoluminescence bias map of a CQD under nonresonant excitation at 909.4 nm, with intensity represented as color on a logarithmic scale. Each prominent charge state is labeled by its anticrossings (red squares) and the involved transitions in the localized basis (arrows).

Basic non-resonant photoluminescence (PL) experiments use high-energy laser excitation to generate electron-hole pairs in CQD excited states which quickly relax to one of several ground states before recombining optically as detected PL. We typically generate electron-hole pairs directly in CQD excited states with $890 - 920$ nm excitation, but higher-energy excitation of free excitons in the wetting layer or surrounding GaAs barrier is also possible (requires subsequent capture into CQD states, reducing efficiency). PL is typically seen with the diode under reverse bias, with minimal current to allow generated charges to recombine optically rather than tunnel out of the CQD. Any reference to bias voltages presented here should therefore be understood as being applied in the reverse-bias direction. Since charge confinement is heavily influenced by applied electric field, the bias is stepped through a range of values to map out changes in the PL spectrum. At each bias value, the spectrally-dispersed PL signal is recorded as the number of counts registered in each CCD pixel, with vertical binning over the central $11 - 25$ pixels where the detection beam is focused. These spectra are then compiled into a two-dimensional PL bias map, showing the number of counts on a chosen color scale as a function of PL energy and applied bias.

One example of a PL map with particularly clear and identifiable transitions is shown in Fig. 3.3. The defining feature of QD PL is the presence of multiple narrow transitions (linewidth < 500 μeV), indicating recombination from stable bound charge states. Each transition is only visible over a limited range of bias voltages where the associated charge states are stable. Outside of this range, excess charges tunnel into or out of the QDs faster than they can recombine optically, with the QDs relaxing to the lowest-energy stable charge state at each bias voltage. The nearby n-doped GaAs buffer layer provides an excess of electrons at low bias voltages, while electrons successively tunnel out in a series of charging steps as the bias voltage is increased. Though many PL energies appear to remain constant with bias, a slight quadratic shift due to the quantum-confined Stark effect can be seen in transitions with an extended charge stability range. Each of these features is common to bias maps of single QDs as well as CQDs.

CQDs can be identified by the presence of spatially indirect (interdot) transitions with a large linear Stark shift in the PL bias map, in addition to the spatially direct (intradot) transitions with a much smaller quadratic Stark shift. At the intersection of some pairs of direct and indirect transitions, the formation of an avoided crossing—referred to as an anticrossing (AC)—indicates a tunnel coupling between two of the involved charge states. Multiple ACs can be observed at different energies and bias values corresponding to different charge states, with the size of the AC indicating the tunnel coupling strength (minimum energy difference $\Delta E = 2t$). In addition, transitions with two initial and two final states possible due to interdot tunneling form a connected pattern with two pairs of ACs, referred to as an X-pattern due to its appearance on a bias map. Two of these X-patterns can be seen in Fig. 3.3 for recombination of neutral biexciton (XX^0) and positive trion (X^+) states, though only one half of the positive trion X-pattern can be seen due to electron tunneling from the n-doped substrate at the onset of forward bias.

Some transitions are composed of multiple parallel peaks with a small energy difference, indicating different spin states separated by a spin exchange interaction. The behavior of these spin states near ACs can be used to uniquely identify the charge states involved by matching observations to a theoretical model. The relative energy shifts of $1 - 5$ meV between direct transitions due to Coulomb interactions can also help identify charge states, though the exact values of Coulomb shifts depend sensitively on CQD geometry and confinement with significant variations even between CQDs in the same sample.

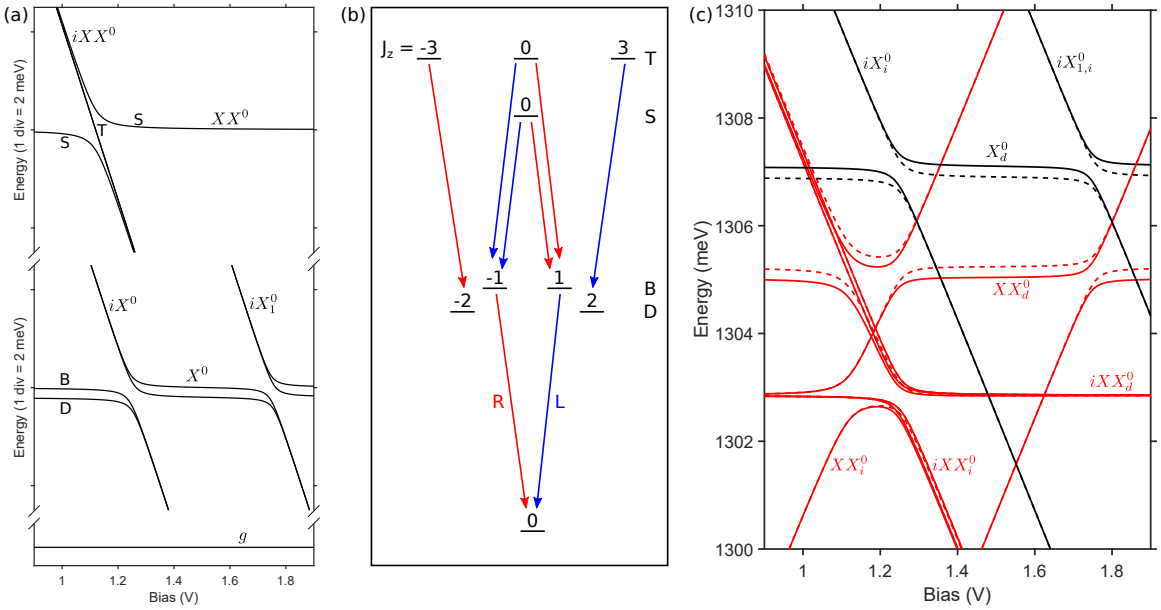

Figure 3.4: (a) Calculated energies of neutral exciton and biexciton states as a function of bias, with charge and spin states labeled. (b) Spin states and allowed optical transitions with left (blue) and right (red) circular polarizations. (c) Calculated transition energies of optically allowed (solid lines) and forbidden (dashed lines) as a function of bias, with exciton (black) and biexciton (red) recombinations labeled.

The theoretical model of PL transitions resulting from the various possible charge and spin states listed in Table 3.1 is outlined in Fig. 3.4 for the neutral exciton and biexciton. The neutral exciton, with one electron and one hole, has two bright spin states ($J_z = \pm 1$) with optical recombination to the ground state allowed and two dark spin states ($J_z = \pm 2$) with optical recombination forbidden by conservation of angular momentum ($\Delta J_z = 0, \pm 1$). Neglecting the small exchange splitting between bright states and between dark states, the interdot exchange splitting, and the Stark shift of the direct exciton state, the neutral exciton Hamiltonian as a function of bias

q	n_X	Charge State	$\left(\begin{smallmatrix} e_B & e_T \\ h_B & h_T \end{smallmatrix}\right)$	Spin States	J_z
0	0	g	$\left(\begin{smallmatrix} 0 & 0 \\ 0 & 0 \end{smallmatrix}\right)$	$\|0\rangle$	0
	1	X^0	$\left(\begin{smallmatrix} 1 & 0 \\ 1 & 0 \end{smallmatrix}\right)$	$\|\downarrow\Uparrow\rangle, \|\uparrow\Downarrow\rangle$	±1
				$\|\uparrow\Uparrow\rangle, \|\downarrow\Downarrow\rangle$	±2
		iX^0	$\left(\begin{smallmatrix} 1 & 0 \\ 0 & 1 \end{smallmatrix}\right)$	$\|\downarrow\Uparrow\rangle, \|\uparrow\Downarrow\rangle$	±1
				$\|\uparrow\Uparrow\rangle, \|\downarrow\Downarrow\rangle$	±2
	2	XX^0	$\left(\begin{smallmatrix} 2 & 0 \\ 2 & 0 \end{smallmatrix}\right)$	$\|\uparrow\downarrow_S \Uparrow\Downarrow_S\rangle$	0
		iXX^0	$\left(\begin{smallmatrix} 2 & 0 \\ 1 & 1 \end{smallmatrix}\right)$	$\|\uparrow\downarrow_S \Uparrow\Downarrow_S\rangle, \|\uparrow\downarrow_S \Uparrow\Downarrow_T\rangle$	0
				$\|\uparrow\downarrow_S \Uparrow\Uparrow_T\rangle, \|\uparrow\downarrow_S \Downarrow\Downarrow_T\rangle$	±3
		$iXiX^0$	$\left(\begin{smallmatrix} 2 & 0 \\ 0 & 2 \end{smallmatrix}\right)$	$\|\uparrow\downarrow_S \Uparrow\Downarrow_S\rangle$	0

Table 3.1: List of all possible CQD charge and spin states with total charge $q = 0$ and number of excitons $n_X \leq 2$, limited to ground-state orbitals and hole tunneling only (electrons fixed in lower-energy bottom QD).

U can be written as

$$H_X = E_X + \frac{\delta_0}{2} - \begin{array}{c} \begin{array}{cccccc} |X_B^0\rangle & |X_D^0\rangle & |iX_B^0\rangle & |iX_D^0\rangle & \left|iX_{1,B}^0\right\rangle & |iX_{1.D}^0\rangle \end{array} \\ \left(\begin{array}{cccccc} 0 & 0 & t_h & 0 & t_{h1} & 0 \\ 0 & \delta_0 & 0 & t_h & 0 & t_{h1} \\ t_h & 0 & p(U-U_0) & 0 & 0 & 0 \\ 0 & t_h & 0 & p(U-U_0) & 0 & 0 \\ t_{h1} & 0 & 0 & 0 & p(U-U_1) & 0 \\ 0 & t_{h1} & 0 & 0 & 0 & p(U-U_1) \end{array}\right) \end{array}, \tag{3.1}$$

with part of the exchange splitting factored out to simplify notation and for the AC bias values to correspond to the observed bright state transitions. The various parameters can be determined by fitting to the observed peak energies, including the neutral exciton energy $E_X = 1307.0$ meV, the bright-dark exchange splitting $\delta_0 = 200$ μeV, the ground state hole tunnel coupling $t_h = 292$ μeV, the excited state hole tunnel coupling $t_{h1} = 253$ μeV, the indirect transition slope $p = 17.79$ meV/V, the ground state AC bias $U_0 = 1.242$ V, and the excited state AC bias $U_1 = 1.746$ V. Within the same approximations, the neutral biexciton Hamiltonian can be written as

$$H_{XX} = 2E_X - E_b - \begin{array}{c} \begin{array}{ccc} |XX_S^0\rangle & |iXX_S^0\rangle & |iXX_T^0\rangle \end{array} \\ \left(\begin{array}{ccc} 0 & \sqrt{2}t_h & 0 \\ \sqrt{2}t_h & p(U-U_2) & 0 \\ 0 & 0 & p(U-U_2) \end{array}\right) \end{array}. \tag{3.2}$$

The same experimental parameters are used, along with the biexciton Coulomb binding energy $E_b = 1.98$ meV and the biexciton AC bias $U_2 = 1.12$ V. Note that the extra

factor of $\sqrt{2}$ in the tunnel coupling results from the presence of two indistinguishable holes available for tunneling, while the spin-conserving nature of tunnel coupling prevents tunneling between different spin states. As a result, the three iXX_T^0 triplet spin states pass through the biexciton AC unaffected.

The calculated PL transition energies match the patterns observed in the experimental bias map, except where limited charge stability ranges prevent visibility of transitions. Transitions resulting from direct recombination (X_d^0, XX_d^0, and iXX_d^0) and those resulting from indirect recombination (iX_i^0, $iX_{1,i}^0$, and iXX_i^0) are all visible. Even the indirect recombination of the direct biexciton state (XX_i^0), requiring a two-step hole tunneling and optical recombination process and having an opposite bias slope, is visible near the biexciton X-pattern with a much lower intensity. A similar process can be followed to match the positive trion or any other observed X-patterns to theoretical predictions to confirm their identification as particular CQD charge states.

3.5 Photoluminescence Excitation Spectroscopy

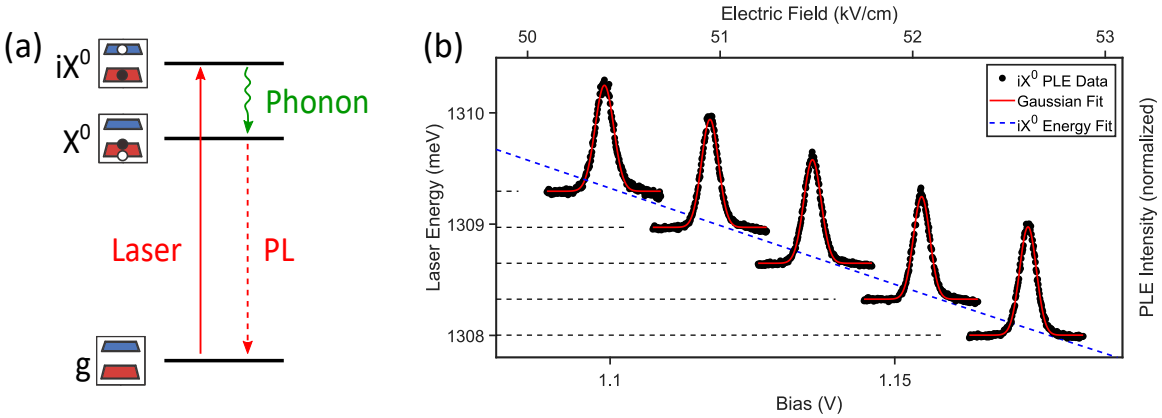

Figure 3.5: (a) Diagram of photoluminescence excitation experiment, exciting indirect exciton and detecting direct exciton emission after phonon relaxation. (b) Series of iX^0 PLE spectra at different laser excitation energies.

Photoluminescence excitation (PLE) spectroscopy is performed by tuning the excitation laser across a transition—directly, by changing the laser wavelength, or indirectly, by changing the applied bias to Stark-shift the transition through resonance with the laser—and monitoring a spectrally separate recombination pathway, such as the LO phonon-assisted emission when probing direct exciton states, or direct exciton emission following phonon-assisted tunneling when probing indirect exciton states [69]. The resulting PLE spectrum indicates optical absorption, with a resolution limited by the linewidth of the excitation laser ($\lesssim 0.1$ μeV) rather than the resolution of the spectrometer ($\sim 25-100$ μeV). Figure 3.5 shows an example of iX^0 PLE spectra obtained by Stark-shifting the transition through resonance with the excitation laser

at a series of different laser energies, detecting X^0 PL at 1306.64 meV after relaxation by phonon-assisted tunneling. Two-laser PLE is performed similarly, using two lasers resonant with each step of a biexciton absorption pathway, tuning one laser through a resonance (or tuning the bias to step both transitions through resonance) and monitoring the recombination from a different pathway.

Chapter 4

Entanglement Generation

Quantum mechanics allows for the unique possibility of instantaneous non-local correlation, or entanglement, between particles. Several technologies have emerged which use quantum entanglement as a fundamental resource, including quantum computation[70, 71, 13, 72, 73, 74] and cryptography,[13, 74, 75, 76, 77, 78] as well as entangled-photon microscopy.[79] Quantum information technologies can be implemented by using the orthogonal polarization states of a photon to encode binary information in a "dual-rail" qubit scheme,[80] which allows for simple manipulation and distribution of photonic qubits using linear optical elements,[81] or using spin states of bound charges.[82] However, a source of entanglement between photons or distant spins is needed to implement two-qubit gates or two-photon quantum cryptography protocols.

Entangled photon pairs are routinely produced by nonlinear optical processes such as spontaneous parametric downconversion (SPDC), in which one photon interacts with a bulk crystal to produce two lower-energy photons with opposite polarizations. However, due to the probabilistic nature of such an interaction, SPDC-based entangled photon sources can always produce zero, one, or multiple photon pairs from each incident pulse, which can introduce errors in entanglement-based quantum information.[83] Semiconductor quantum dots (QDs) are promising candidates for on-demand sources of entangled photon pairs, as well as spin-photon entanglement.[84, 85] Two-photon emission can be achieved by optically exciting the neutral biexciton state, consisting of two bound excitons. Radiative decay from this state can proceed along one of two pathways corresponding to the two optically active single-exciton spin states. Coherence between these two oppositely-polarized (but otherwise indistinguishable) emission processes results in a pair of polarization-entangled photons. In single QDs, however, the degeneracy of the intermediate exciton spin states is often removed by the anisotropic electron-hole exchange splitting, which is due to asymmetry in the self-assembled QD system.[86, 87, 88] If this splitting is larger than the optical transition linewidths, the emitted photons are distinguishable by their energy and exhibit correlated—but not entangled—polarizations.[89] Several techniques have been implemented to avoid this problem, including postselection via spectral filtering[90] and minimization of the exchange splitting by post-

growth thermal annealing[91] or application of external fields.[92, 93] Alternative QD growth methods have also been demonstrated to exhibit a systematically smaller exchange splitting, including interface fluctuation QDs[94] and QDs grown on the (111) surface of GaAs.[95, 96] Aside from neutral biexciton decay, negatively-charged states in QDs can also be used to create a chain of entangled photons in a one-dimensional cluster state.[97] This procedure can be generalized to two dimensions using two vertically-stacked coupled quantum dots (CQDs).[23] Here we discuss a scheme in which entangled photon pairs are obtained straightforwardly through a cascaded biexciton-exciton decay.

Section 4.1 describes a theoretical model of cascaded optical recombination from an interdot biexciton state in a CQD in the presence of phonon-assisted tunneling and spin-flip relaxation processes, and the results of numerical simulations identifying parameter regimes where two-photon polarization entanglement can be expected. Section 4.2 outlines a theoretical model of two-photon absorption into the interdot biexciton state under resonant two-laser driving, and describes the results of initial experiments demonstrating two-photon absorption.

4.1 Molecular Biexciton Cascade

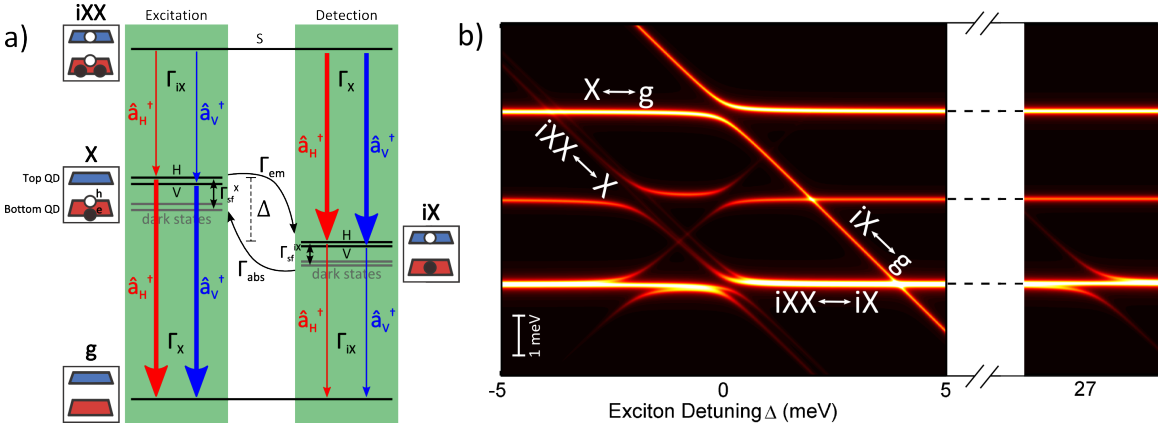

Figure 4.1: (a) Energy level diagram of the molecular biexciton radiative cascade, depicting polarizations of all allowed recombination pathways, as well as spin-flip and phonon-assisted hole tunneling channels. Thick vertical arrows indicate direct exciton recombination, while thin vertical arrows indicate a slower interdot recombination. Excitation and detection pathways are indicated by green shading. (b) Simulated electric field-dispersed photoluminescence spectrum, mapping out each of the relevant transition energies in the vicinity of the exciton and biexciton hole tunneling resonances. Single-exciton hole tunneling resonance occurs at $\Delta = 0$ meV, while biexciton hole tunneling resonances occur at $\Delta = -1.9$ and 27.2 meV.

Our scheme for on-demand entangled photon pairs uses CQDs grown in an electric field-effect structure, such as a Schottky diode.[98, 99, 100, 101] The CQD structure permits two types of neutral excitons: direct excitons, with the electron and hole in the same dot, and indirect excitons, with the electron and hole separated in different dots. Because of their spatial charge separation, the energies of indirect states can easily be tuned by applying an electric field.[102, 57, 103] In addition, spatial charge separation greatly reduces both the short-range isotropic and long-range anisotropic exchange splitting of indirect exciton spin states.[100, 63] This property can potentially be used for generation of entangled photon pairs by preparing the CQD in an indirect biexciton spin singlet state, with one direct (single-dot) exciton and one indirect exciton. In an effort to determine the utility of this proposal, we theoretically calculate the fidelity of entangled photon generation in a CQD system.

We consider an asymmetric CQD system of two vertically stacked, tunnel-coupled, self-assembled InAs/GaAs QDs (referred to here as the bottom and top dots) with respective heights h_B and h_T and center-to-center separation d, grown in a diode structure to allow application of an electric field F along the growth direction. Depending on the dot asymmetry and applied field direction, either electron or hole levels can be tuned into resonance, causing electrons or holes to tunnel coherently.[1] For the remainder of this work and without loss of generality we will assume a CQD diode structure is chosen that promotes hole tunneling, with any excited electrons confined to the bottom dot.

We restrict the CQD Hilbert space to that of the crystal ground state $|g\rangle$, direct exciton $|X\rangle$, indirect exciton $|iX\rangle$, and molecular biexciton $|iXX\rangle$ (consisting of one direct and one indirect exciton). Each of the single-exciton charge states can exist in one of four spin states: two optically active bright states $|H/V\rangle = |{\downarrow}{\Uparrow} \pm {\uparrow}{\Downarrow}\rangle$, and two optically inactive dark states $|H_d/V_d\rangle = |{\uparrow}{\Uparrow} \pm {\downarrow}{\Downarrow}\rangle$ (single (double) arrows denote spin-1/2 electrons (spin-3/2 heavy holes)). The molecular biexciton can exist in a singlet $|S\rangle = |{\uparrow}{\downarrow} - {\downarrow}{\uparrow}\rangle\,|{\Uparrow}{\Downarrow} - {\Downarrow}{\Uparrow}\rangle$ or one of three triplet spin states $|T_+\rangle = |{\uparrow}{\downarrow} - {\downarrow}{\uparrow}\rangle\,|{\Uparrow}{\Uparrow}\rangle$, $|T_0\rangle = |{\uparrow}{\downarrow} - {\downarrow}{\uparrow}\rangle\,|{\Uparrow}{\Downarrow} + {\Downarrow}{\Uparrow}\rangle$, or $|T_-\rangle = |{\uparrow}{\downarrow} - {\downarrow}{\uparrow}\rangle\,|{\Downarrow}{\Downarrow}\rangle$.

While a CQD exhibits many optical transitions, we focus on the molecular biexciton spin singlet state $|iXX, S\rangle$, which can produce correlated photon pairs by sequential recombination to the ground state due to the optical selection rules. As depicted in Fig. 4.1(a), this state is optically coupled to the ground state through the bright spin states of the direct and indirect exciton, forming two pairs of oppositely-polarized decay pathways.

Photon emission events can be described within the CQD and photon subspaces using transition operators $\hat{\sigma}_{1H/V,D/I}$ ($\hat{\sigma}_{2H/V,D/I}$) and photon creation operators $\hat{a}^\dagger_{H/V}$, which act on the system to produce the first (second) H/V-polarized photon by direct/indirect recombination of the biexciton (exciton) state (see Table 4.1 for details). Assuming that the system has been prepared in the molecular biexciton spin singlet state $|\Psi_0\rangle = |iXX, S\rangle$ and that recombination occurs via the indirect exciton

Table 4.1: List of incoherent processes included in the master equation, with corresponding transition rates and operators. Exciton spin states are indexed by $m = H, V, H_d, V_d$.

Process	Rate	Operator
Recombination	Γ_X	$\hat{\sigma}_{1H/V,D} = \lvert iX, H/V\rangle \langle iXX, S\rvert$
		$\hat{\sigma}_{2H/V,D} = \lvert g\rangle \langle iX, H/V\rvert$
	Γ_{iX}	$\hat{\sigma}_{1H/V,I} = \lvert X, H/V\rangle \langle iXX, S\rvert$
		$\hat{\sigma}_{2H/V,I} = \lvert g\rangle \langle iX, H/V\rvert$
Phonon-assisted tunneling	Γ_{abs}	$\lvert X, m\rangle \langle iX, m\rvert$
	Γ_{em}	$\lvert iX, m\rangle \langle X, m\rvert$
Phonon-assisted spin-flip	Γ_{sf}^{X}	$\lvert X, H_d/V_d\rangle \langle X, H/V\rvert$, H.c.
	Γ_{sf}^{iX}	$\lvert iX, H_d/V_d\rangle \langle iX, H/V\rvert$, H.c.
Pure dephasing	γ_p^X	$\sum_m \lvert X, m\rangle \langle X, m\rvert$
	γ_p^{iX}	$\sum_m \lvert iX, m\rangle \langle iX, m\rvert$

pathway without nonradiative transitions, the first recombination produces the state

$$\begin{aligned} |\Psi_1\rangle &= \frac{1}{\sqrt{2}}(\hat{a}_H^\dagger \hat{\sigma}_{1H,D} + \hat{a}_V^\dagger \hat{\sigma}_{1V,D}) \, |\Psi_0\rangle \\ &= \frac{1}{\sqrt{2}}(|H\rangle_1 \, |iX, H\rangle + |V\rangle_1 \, |iX, V\rangle). \end{aligned} \tag{4.1}$$

During the time τ before the second photon is emitted, the system undergoes coherent evolution, acquiring a phase difference due to the exchange interaction:

$$\begin{aligned} |\Psi_1(\tau)\rangle &= e^{-i\hat{H}\tau/\hbar} \, |\Psi_1(0)\rangle \\ &= \frac{1}{\sqrt{2}}(|H\rangle_1 \, |iX, H\rangle + e^{iS_I\tau/\hbar} \, |V\rangle_1 \, |iX, V\rangle), \end{aligned} \tag{4.2}$$

to within a global phase factor, where S_I is the exchange splitting between indirect exciton bright spin states. Finally, the second recombination results in

$$\begin{aligned} |\Psi_2\rangle &= \frac{1}{\sqrt{2}}(\hat{a}_H^\dagger \hat{\sigma}_{2H,I} + \hat{a}_V^\dagger \hat{\sigma}_{2V,I}) \, |\Psi_1(\tau)\rangle \\ &= \frac{1}{\sqrt{2}}(|H\rangle_1 \, |H\rangle_2 + e^{iS_I\tau/\hbar} \, |V\rangle_1 \, |V\rangle_2) \, |g\rangle \\ &\equiv |\Psi_{2P}\rangle \, |g\rangle \, , \end{aligned} \tag{4.3}$$

with the two photons in a pure polarization-entangled state $|\Psi_{2P}\rangle$. However, since recombination can occur via multiple pathways, the result is a mixed state, described by the two-photon density matrix $\hat{\rho}_{2P}$.

In the absence of anisotropic electron-hole exchange splitting, each pair of oppositely-polarized decay pathways are energetically indistinguishable, resulting in the maximally-entangled Bell state $|\Psi^+\rangle = (|H\rangle_1 |H\rangle_2 + |V\rangle_1 |V\rangle_2)/\sqrt{2}$ for the polarizations of the emitted photon pair.[104, 105] Under generic conditions, we quantify the quality of entanglement by the fidelity of the two-photon polarization state to the target Bell state. This fidelity is determined by the projection

$$\begin{aligned} F^+ &= \left\langle \Psi^+ \right| \hat{\rho}_{2P} \left| \Psi^+ \right\rangle \\ &= \frac{1}{2}(\rho_{|HH\rangle\langle HH|} + \rho_{|VV\rangle\langle VV|}) + \mathrm{Re}(\rho_{|HH\rangle\langle VV|}). \end{aligned} \tag{4.4}$$

A fidelity higher than 0.5 indicates polarization entanglement, while a lower fidelity is acheivable by classical correlation alone. Uncorrelated photons, such as background light not originating from the CQD, give a baseline fidelity of 0.25.[105, 106]

The CQD system interacts with the finite-temperature phonon bath of the surrounding crystal lattice, as well as the vacuum electromagnetic field via spontaneous emission. We assume Markovian behavior, such that the environment always remains at equilibrium (emitted particles cannot be reabsorbed). This assumption requires that any system-environment correlations decay on a much faster time scale than the system dynamics, which could introduce some inaccuracies at the lowest temperatures simulated ($T = 1$ K) due to long-lived reservoir correlations. Using the Rotating Wave Approximation to average over quickly-oscillating terms, we can then describe the dissipative dynamics of this open quantum system using the Lindblad master equation[107] for the reduced density matrix $\hat{\rho}$ of the system:

$$\frac{\partial}{\partial t}\hat{\rho} = \frac{1}{i\hbar}[\hat{H}, \hat{\rho}] + \sum_i \Gamma_i \left(\hat{\sigma}_i \hat{\rho} \hat{\sigma}_i^\dagger - \frac{1}{2}\hat{\sigma}_i^\dagger \hat{\sigma}_i \hat{\rho} - \frac{1}{2}\hat{\rho}\hat{\sigma}_i^\dagger \hat{\sigma}_i \right) \tag{4.5}$$

We assume that an initial state of $\hat{\rho}(0) = |iXX, S\rangle \langle iXX, S|$ is prepared by pulsed excitation, and do not explicitly include interaction with the optical pulse. By projecting onto the basis states, Eq. (4.5) can be written as $\langle i| \dot{\hat{\rho}} |j\rangle \equiv \dot{\rho}_{ij} = \sum_{kl} M_{ij,kl}\rho_{kl}$, where the elements of the time-dependence tensor $M_{ij,kl}$ contain the various coherent phase evolution, transition and decay rates. Vectorizing the elements of $\hat{\rho}$ results in the matrix differential equation $\dot{\vec{\rho}} = M\vec{\rho}$, leading to the solution $\vec{\rho}(t) = e^{Mt}\vec{\rho}(0)$. In terms of the superoperator $\mathscr{L}\hat{\rho} = \partial_t \hat{\rho}$ defined by Eq. (4.5), this solution can also be written as $\hat{\rho}(t) = e^{\mathscr{L}\tau}\hat{\rho}(0)$.

For a given decay pathway, with the first (second) photon generated by $\alpha(\beta) = D/I$ recombination after a time delay τ, the density matrix element $\langle ij| \hat{\rho}_{2P}(\tau) |kl\rangle$ in the two-photon linear polarization basis is related to the CQD dynamics by the two-time correlation function[108, 109]

$$\begin{aligned} g^{(2)}_{ijkl,\alpha\beta}(\tau) &= \langle \hat{\sigma}^\dagger_{1i,\alpha}(0)\hat{\sigma}^\dagger_{2j,\beta}(\tau)\hat{\sigma}_{2l,\beta}(\tau)\hat{\sigma}_{1k,\alpha}(0)\rangle \\ &= \mathrm{Tr}\left[\hat{\sigma}_{2l,\beta}\, e^{\mathscr{L}\tau}(\hat{\sigma}_{1k,\alpha}\hat{\rho}(0)\hat{\sigma}^\dagger_{1i,\alpha})\, \hat{\sigma}^\dagger_{2j,\beta} \right], \end{aligned} \tag{4.6}$$

where the last line follows from the quantum regression theorem.[107] These polarization correlations can be measured experimentally using time-correlated single-photon counting in a Hanbury Brown-Twiss setup,[110] where each detection pathway contains polarization optics and a monochromator to spectrally select the relevant transitions and perform polarization cross-correlation measurements.[90, 104] Since recombination can occur via several pathways with a random time delay, the elements of $\hat{\rho}_{2P}$ are calculated by using a time-averaged statistical mixture

$$\rho_{|ij\rangle\langle kl|} = A \sum_{\alpha,\beta=D,I} \int_0^{T_d} d\tau \, P_{1\alpha} P_{2\beta}(\tau) g^{(2)}_{ijkl,\alpha\beta}(\tau), \tag{4.7}$$

where T_d is the detection time window, A is a normalization constant set to enforce the condition $\mathrm{Tr}\,(\hat{\rho}_{2P}) = 1$, $P_{1D(I)} = \Gamma_{X(iX)}/(\Gamma_X + \Gamma_{iX})$ is the probability of direct (indirect) recombination of the first exciton, $P_{2D(I)}(\tau) = \Gamma_{X(iX)} n_{X(iX)}(\tau)$ is the probability per unit time of the second direct (indirect) recombination, and $n_{X(iX)}(\tau)$ is the population of bright states $|X(iX), \pm 1\rangle$ at time τ. Transition rates for direct and indirect exciton recombination are denoted by Γ_X and Γ_{iX}, respectively.

The critical dynamics determining photon entanglement occurs during the time τ between photon emission events, when the dynamics is limited to the single-exciton subspace. Truncating to the bright spin states, the simplified exciton Hamiltonian can be written

$$\hat{H} = \begin{array}{c} \begin{array}{cccc} |iX,H\rangle & |iX,V\rangle & |X,H\rangle & |X,V\rangle \end{array} \\ \begin{pmatrix} S_I/2 & 0 & t_h & 0 \\ 0 & -S_I/2 & 0 & t_h \\ t_h & 0 & \Delta + S_D/2 & 0 \\ 0 & t_h & 0 & \Delta - S_D/2 \end{pmatrix} \end{array}, \tag{4.8}$$

where $\Delta = ed(F - F_0)$ is the exciton detuning due to the applied electric field, F_0 is the field value at the $|X\rangle - |iX\rangle$ anticrossing, and t_h is the resonant hole tunnel coupling including Coulomb correction. The magnitude of the exchange splitting $S_{D/I}$ is a critical factor for entangled photon emission, as a splitting larger than the radiative linewidth of the corresponding exciton is expected to render the two decay pathways distinguishable and prevent entanglement. The bright-state exchange splitting is approximated using the dipole interaction term of the long-range multipole expansion:[60]

$$\begin{aligned} S_{D(I)} \approx & \frac{1}{\pi\epsilon} \iint d^3\vec{r}\, d^3\vec{r}\,' \frac{\vec{\mu}^{\dagger}_{\uparrow\Downarrow}(\mathbb{1} - \hat{n}\hat{n}^{\dagger})\vec{\mu}_{\downarrow\Uparrow}}{|\vec{r} - \vec{r}\,'|^3} \\ & \times \psi^{e*}_B(\vec{r})\psi^{e}_B(\vec{r}\,')\psi^{h*}_{B(T)}(\vec{r}\,')\psi^{h}_{B(T)}(\vec{r}), \end{aligned} \tag{4.9}$$

where ϵ is the average permittivity of InAs and GaAs, $\mathbb{1}$ is the 3×3 identity matrix, $\hat{n}$ is a unit vector in the direction of $(\vec{r} - \vec{r}\,')$, and $\vec{\mu}_{\sigma\chi} = e\,\langle u^e_\sigma |\, \hat{\vec{r}}\, | u^h_\chi \rangle$ is the interband transition dipole moment. Since S_D varies widely in self-assembled QDs in the range $0 - 100$ μeV depending on detailed growth conditions, we leave it as a variable parameter in the model and numerically evaluate Eq. (4.9) to obtain S_I/S_D.

Incoherent transitions, described by operators $\hat{\sigma}_i$ and occuring at rates Γ_i, include optical recombination, phonon-assisted hole tunneling, spin-flip, and pure dephasing (see Table 4.1). These transitions are incoherent in the sense that they occur at random times, because we trace over the photonic and phononic environment degrees of freedom to obtain the reduced density matrix of the CQD system. We assume a direct exciton recombination rate $\Gamma_X = 1$ ns^{-1} similar to experimentally observed rates in InAs/GaAs QDs. Indirect recombination rates Γ_{iX} are found to be slower than direct recombination by a factor of $(M_{BT}/M_{BB})^2 \sim 100 - 1000$ due to a smaller electron-hole wavefunction overlap $M_{ij} = \left\langle \psi_i^e | \psi_j^h \right\rangle$ for the interdot state.[111]

Holes undergo incoherent spin-conserving tunneling transitions via emission or absorption of a phonon, causing transitions between direct and indirect exciton states at rates given by Fermi's golden rule as

$$\Gamma_{abs} = \frac{2\pi}{\hbar} J(\Delta) n_B(\Delta, T) \tag{4.10}$$

$$\Gamma_{em} = \frac{2\pi}{\hbar} J(\Delta)(n_B(\Delta, T) + 1), \tag{4.11}$$

where $J(E) = \sum_{\vec{q}} |\langle X| \hat{H}_{el-ph} |iX\rangle|^2 \delta(E_{\vec{q}} - E)$ is the phonon spectral density of the interdot transition, $n_B(E,T) = 1/(e^{E/k_B T} - 1)$ is the Bose distribution, giving the population of phonon modes at energy E and temperature T, $\vec{q}$ denotes the phonon wave vector, $\hat{H}_{el-ph}$ is the electron-phonon interaction Hamiltonian, and we use a linear dispersion relation $E_{\vec{q}} = \hbar c_{LA} |\vec{q}|$ for acoustic phonons. We assume here that $\Delta \equiv E_X - E_{iX} > 0$, so that tunneling to the direct exciton is partially suppressed, requiring absorption of a phonon. Since the detuning in the region of interest is much less than the LO phonon energy in GaAs, we consider only acoustic phonon-mediated transitions and neglect coupling to LO phonons. Including only interaction via the acoustic deformation potential, which is usually found to dominate for electronic transitions in quantum dots, leads to the expression[112]

$$J(\Delta) = \frac{\Delta a_V^2}{16\pi^3 \rho c_{LA}^2} \int d^3\vec{q} \left| \int d^3\vec{r}\, \psi_{hB}^* e^{i\vec{q}\cdot\vec{r}} \psi_{hT} \right|^2 \delta(E_{\vec{q}} - \Delta), \tag{4.12}$$

where a_V is the valence-band deformation potential, ρ is the mass density of the crystal, c_{LA} is the speed of the LA phonon mode in GaAs, and $\psi_{h\alpha}$ is the single-particle wavefunction for a hole localized in dot $\alpha = B, T$. We note that multiphonon and LO-phonon tunneling transitions are not included, which may become important at higher temperatures and exciton detunings than considered here.

Spin-flip transitions are also known to occur between exciton spin states, via phonon and spin-orbit coupling.[113, 114, 115, 116] In particular, spin relaxation occurs in direct (indirect) excitons primarily via phonon-assisted transitions between bright and dark spin states at a rate $\Gamma_{sf}^{X(iX)}$. Since our two-band effective mass model does not account for spin-orbit coupling, we include spin relaxation phenomenologically. We include only transitions between bright and dark spin states, since bright-bright and dark-dark transitions are at least an order of magnitude slower due to their

smaller transition energies.[113] We use the temperature-dependence of the spin-flip rate measured by Fras et al.[117], scaled to fit the behavior measured by Hudson et al.[105]: $\Gamma_{sf}^{X}(T) = (0.27\ \mathrm{ns}^{-1}) + (0.29\ \mu\mathrm{s}^{-1}\,\mathrm{K}^{-2})T^2$, corresponding to a thermally-activated two-phonon process. In the low-temperature regime where single-phonon transitions dominate and for small bright-dark splittings $\Delta_{bd}^{D(I)}$, $\Gamma_{sf}^{X(iX)}$ is given by Fermi's golden rule as in Eq's (4.10) and (4.11), with $J(\Delta_{bd}^{D(I)}) \propto (\Delta_{bd}^{D(I)})^3$ and $n(\Delta_{bd}^{D(I)}, T) \approx k_B T/\Delta_{bd}^{D(I)}$.[118] Since the bright-dark splitting scales with electron-hole wavefunction overlap, we predict the relationship $\Gamma_{sf}^{iX} = (M_{BT}/M_{BB})^2\,\Gamma_{sf}^{X}$ between direct and indirect spin-flip rates.

The Coulomb interaction energy between particles α and β in dots i and j, respectively, is given by

$$V_{ij}^{\alpha\beta} = \frac{e^2}{4\pi\epsilon}\iint d^3\vec{r}\,d^3\vec{r}\,'\,\frac{|\psi_{\alpha i}(\vec{r})|^2|\psi_{\beta j}(\vec{r}\,')|^2}{|\vec{r}-\vec{r}\,'|}, \tag{4.13}$$

where e is the charge of an electron, ϵ is the average permittivity of InAs and GaAs, and the 6-dimensional integral is directly evalutated by numerical integration over a Cartesian grid. The Coulomb interaction terms modify the energy of multiparticle exciton states, as does the local electric field F due to the large permanent dipole moment $p = ed$ of indirect exciton states. The energies of the various charge states considered are then

$$\begin{aligned} E_X =& E_g + E_{eB} + E_{hB} - V_{BB}^{eh} \\ E_{iX} =& E_g + E_{eB} + E_{hT} - V_{BT}^{eh} - edF \\ E_{iXX} =& 2E_g + 2E_{eB} + E_{hB} + E_{hT} \\ &+ V_{BB}^{ee} + V_{TT}^{hh} - 2V_{BB}^{eh} - 2V_{BT}^{eh} - edF, \end{aligned} \tag{4.14}$$

where E_g is the band gap of the strained InAs comprising each QD.

Eq. (4.9) is expanded using the interband dipole moments

$$\vec{\mu}_{\uparrow\Downarrow(\downarrow\Uparrow)} = \frac{\mu}{\sqrt{2}}(\pm 1, -i, 0) \tag{4.15}$$

to obtain the expression

$$\begin{aligned} S_{D(I)} = \frac{\mu^2}{2\pi\epsilon}\iint d^3\vec{r}\,d^3\vec{r}\,'\,&\frac{2\Delta z^2 - \Delta x^2 - \Delta y^2 + 6i\Delta x\Delta y}{\Delta r^5} \\ &\times \psi_{eB}^*(\vec{r})\psi_{eB}(\vec{r}\,')\psi_{hB(T)}^*(\vec{r}\,')\psi_{hB(T)}(\vec{r}), \end{aligned} \tag{4.16}$$

where $\Delta\vec{r} = \vec{r} - \vec{r}\,'$. Since the exchange splitting varies widely between QDs and small values are required for entanglement generation, we choose values of S_D and numerically integrate Eq. (4.16) to obtain the ratio S_I/S_D.

We use the value of Γ_X listed in Table B.1 and the electron-hole wavefunction overlap

$$M_{ij} = \int d^3\vec{r}\,\psi_{ei}^*(\vec{r})\psi_{hj}(\vec{r}) \tag{4.17}$$

obtained by numerical integration to calculate $\Gamma_{iX} = \Gamma_X (M_{BT}/M_{BB})^2$. The phonon-assisted tunneling rates Γ_{abs} and Γ_{em} are calculated using Eq's 5.18, 5.19 and 5.20, where the phonon wave vector $\vec{q}$ is expressed in spherical coordinates and its magnitude is constrained by the delta function to be $q = \Delta/\hbar c_{LA}$. To calculate the phonon-assisted spin-flip rate of the direct exciton, we use the experimentally-determined temperature dependence $\Gamma^X_{sf} = (.27\ \mathrm{ns}^{-1}) + (.29\ \mu\mathrm{s}^{-1}\mathrm{K}^{-2})T^2$ [117], and from it determine the indirect exciton spin-flip rate $\Gamma^{iX}_{sf} = \Gamma^X_{sf}(M_{BT}/M_{BB})^2$. For the pure dephasing rate, we use the empirical temperature dependence $\hbar\gamma^X_p = (71\ \mu\mathrm{eV}) n_B(6\ \mathrm{meV}, T) + (4.5\ \mathrm{meV}) n_B(28\ \mathrm{meV}, T)$ [119] corresponding to phonon-assisted pure dephasing processes involving excited hole states, and assume the same pure dephasing rate for indirect excitons: $\gamma^{iX}_p = \gamma^X_p$.

By projecting Eq. 4.5 onto each combination of basis states, it becomes $\dot{\rho}_{ij} = \sum_{kl} M_{ij,kl}\rho_{kl}$ and we determine the elements of the time-dependence tensor $M_{ij,kl}$. We then vectorize $\hat{\rho}$ by mapping the matrix elements ρ_{ij} to a one-dimensional vector $\vec{\rho}$. The time-dependence tensor $M_{ij,kl}$ is then transformed into a matrix M_{ij}, and the solution is expressed by a matrix exponential as $\vec{\rho}(\tau) = e^{\mathcal{L}\tau}\vec{\rho}(0) = e^{Mt}\vec{\rho}(0)$. With this matrix exponential describing time evolution of the CQD density matrix, we use Eq's 4.6 and 4.7 to calculate the various elements of the two-photon polarization density matrix $\hat{\rho}_{2P}$ in the linear polarization basis $\{|HH\rangle, |HV\rangle, |VH\rangle, |VV\rangle\}$, averaging over delay times up to $T_d = 200$ ns. With these density matrix elements, the fidelity to the entangled Bell state is finally calculated using Eq. 4.4.

The results of the numerical simulation are summarized in Fig. 4.2. The fidelity approximately exhibits a Lorentzian dependence on the direct exciton exchange splitting S_D, similar to the behavior reported in the case of a single QD.[105, 109, 120, 121, 122] To characterize this behavior, we record the maximum fidelity F^+_{max} at $S_D = 0$ and the fidelity width $\Delta F^+_{.9}$, defined as the largest value of $|S_D|$ with $F^+ > .9$. By plotting these fidelity characteristics as a function of the experimentally tunable exciton detuning Δ and temperature T, we obtain a map of possible behaviors observable in a single CQD pair. In general, we observe that the quality of entanglement depends primarily on the total dephasing rate

$$\gamma^{iX}_d = \Gamma_{iX} + \Gamma_{abs} + \Gamma^{iX}_{sf} \tag{4.18}$$

describing decay of the indirect exciton bright state coherence $\langle iX, +1| \hat{\rho} |iX, -1\rangle$, as well as the effective decay rate Γ_{eff} of the indirect exciton population $\langle iX| \hat{\rho} |iX\rangle$, determined by an exponential fit of the bright state density matrix dynamics. For low temperatures ($T < 40$ K) and large detunings ($\Delta > 3$ meV), entanglement fidelity can reach values above 0.99 for small exchange splittings, with a width $\Delta F^+_{.9} \approx 1.5 - 2.7\ \mu$eV. Note that the CQD system exhibits this high-fidelity behavior with S_D values up to a factor of 5 greater than in the single QD case ($\Delta F^+_{.9,SQD} \approx 0.4 - 0.6\ \mu$eV). In this region, the decoherence is radiatively-limited ($\gamma^{iX}_d < 2\,\Gamma_{iX}$), allowing coherent evolution between photon emission events. With increasing lattice temperature, the overall fidelity decreases due to phonon-assisted tunneling and spin-flip. At detuning values below 3 meV, the large dephasing rate

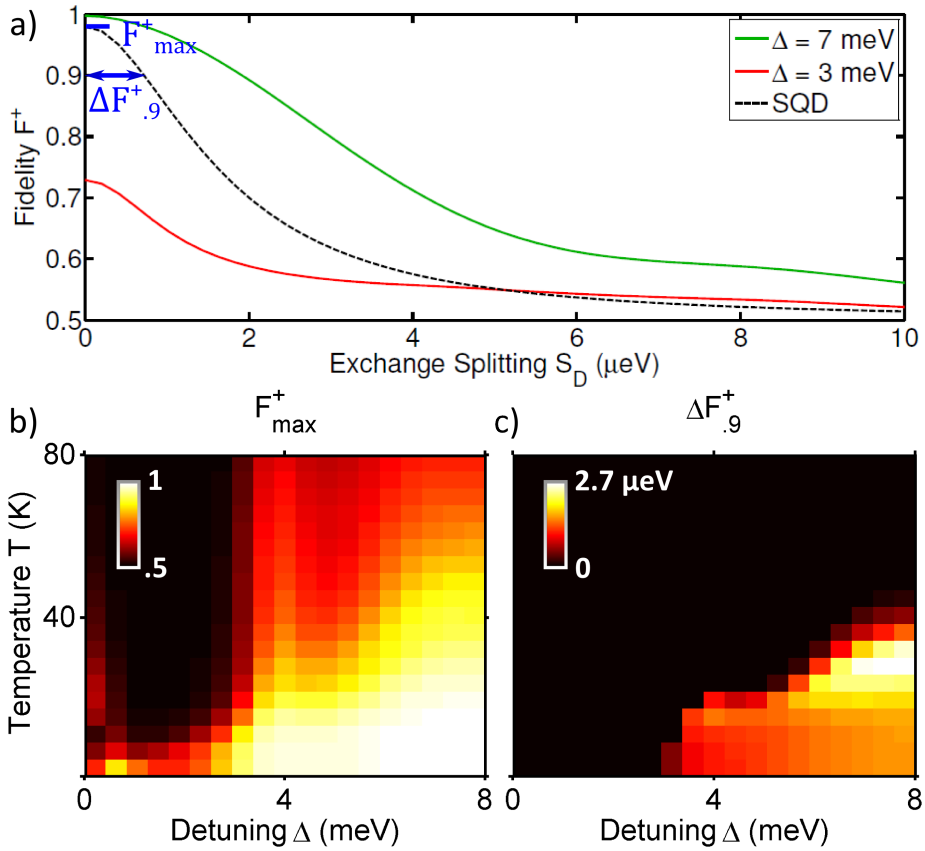

Figure 4.2: (a) Dependence of entanglement fidelity on direct exciton bright state splitting at $T = 20$ K, $t_h = 0.2$ μeV, and $\Delta = 7$ meV (green, top curve) and $\Delta = 3$ meV (red, bottom curve), compared to the analogous SQD case. (b) Maximum fidelity and (c) width of $F^+(S_D)$ curve as a function of exciton detuning and temperature.

($\gamma_d^{iX} > 100\,\Gamma_{iX}$) prevents photon entanglement even in the absence of anisotropic exchange splitting, giving a maximum fidelity near 0.5.

Fig's 4.3(a) and (b) isolate the effect of exciton detuning and temperature, respectively, on the different fidelity characteristics. Fig's 4.3(c) and (d) show the dephasing rate γ_d^{iX} over the same ranges, along with each of the contributing transition rates and the effective indirect exciton population decay rate Γ_{eff}. As in Fig. 4.2, regions of high fidelity correlate with a radiatively-limited dephasing rate. The significant drop in fidelity at low exciton detunings is therefore due to a phonon-assisted hole tunneling rate which surpasses radiative emission by up to 3 orders of magnitude. Note that the oscillations in the tunneling rates are due to the phase $e^{i\vec{q}\cdot\vec{r}}$ appearing in the phonon coupling (Eq. (5.11)), and depend on the distance d between QDs.[123] The peak in fidelity width as a function of temperature occurs when Γ_{eff} increases, while γ_d^{iX} remains low. The increased decay rate of the indirect exciton causes the time-integration in Eq. (4.7) to sample shorter time delays, maintaining high fidelity

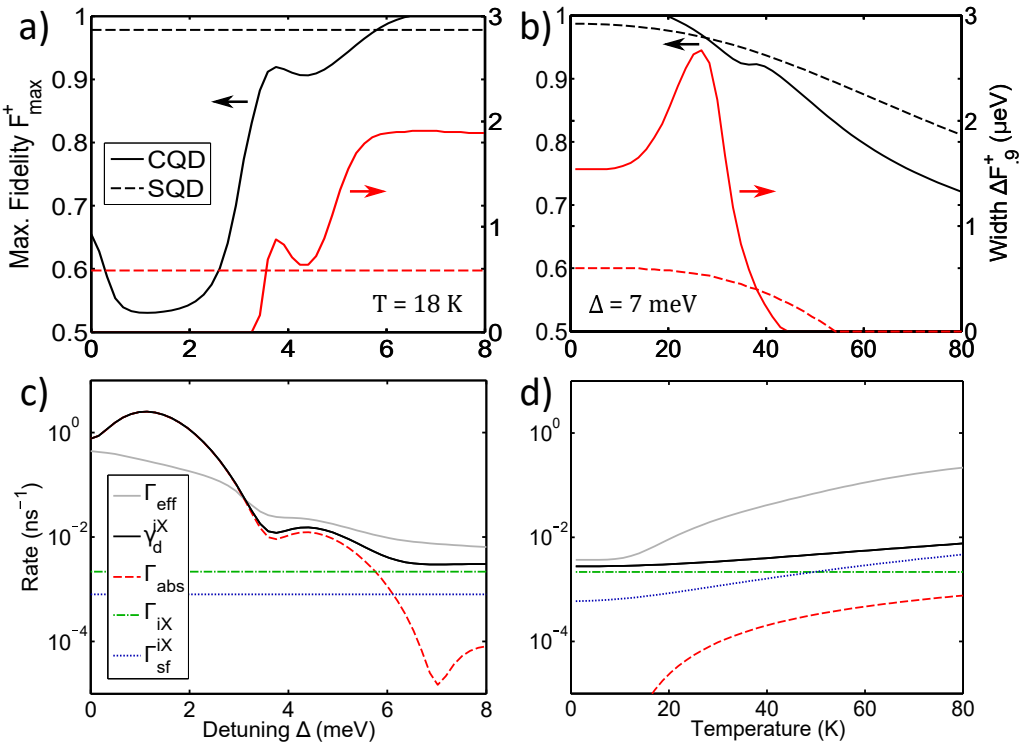

Figure 4.3: (a) (b) Dependence of fidelity parameters F^+_{max} (black, left y-axis) and ΔF^+ (red, right y-axis) on (a) detuning and (b) temperature, with $t_h = 0.2$ μeV. (c) (d) Total dephasing rate γ_d^{iX} of the indirect exciton bright state coherence, including contributions from incoherent transitions, as a function of detuning and temperature, respectively. Also included is the effective $|iX\rangle$ population decay rate Γ_{eff}.

over a larger range of exchange splittings. While hole tunneling can be adequately suppressed by simply maintaining a large enough detuning between exciton states or increasing the tunnel barrier, phonon-assisted spin-flip surpasses radiative emission and reduces fidelity at temperatures above ~ 50 K.

Fig. 4.4 shows the fidelity characteristics as a function of hole tunnel coupling and temperature, at a fixed exciton detuning. The effective indirect exciton decay rate Γ_{eff} depends strongly on both temperature and tunnel coupling, and is demonstrated to have a substantial effect on the entanglement fidelity. F^+_{max} remains higher than 0.9 where $\Gamma_{eff} < 30\,\Gamma_{iX}$, which occurs at low temperature and tunnel coupling values. The fidelity width $\Delta F^+_{.9}$ peaks at intermediate values of Γ_{eff} ($\Gamma_{eff} \approx 5 - 10\,\Gamma_{iX}$) and increases with decreasing tunnel coupling, reaching values above 3.0 μeV at small tunnel couplings ($t_h \leq .1$ meV) and temperatures up to 70 K. As tunnel coupling increases, the indirect exciton gains more of a direct exciton character, decreasing the fidelity width and requiring lower temperatures to suppress recombination.

Our results indicate that by maintaining a large enough exciton detuning to suppress phonon-assisted tunneling, CQD-based entangled photon sources can produce entangled photon pairs with higher fidelity than single QD-based sources, over

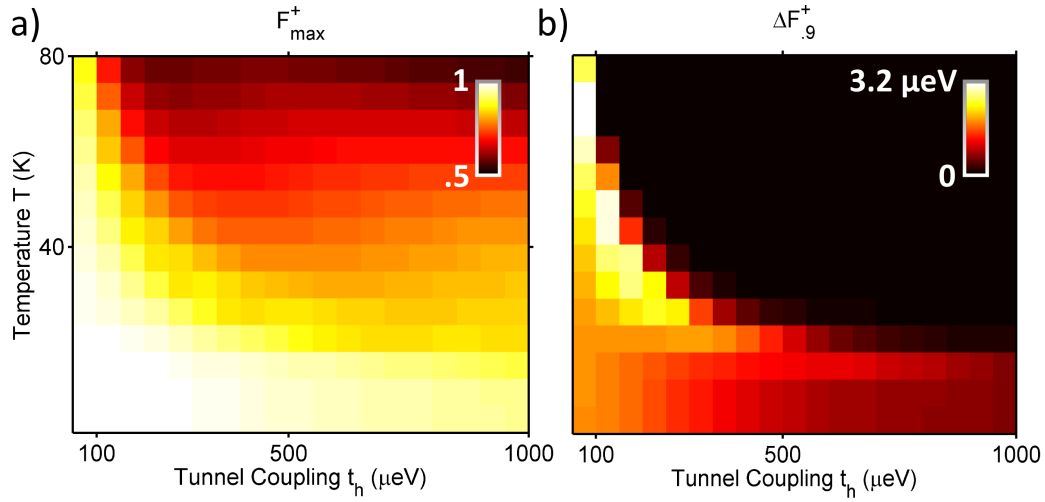

Figure 4.4: (a) Maximum fidelity and (b) width of $F^+(S_D)$ curve as a function of hole tunnel coupling and temperature, with $\Delta = 7$ meV.

a wider range of direct exciton exchange splittings. While this helps reduce the strict symmetry requirement for entanglement generation, the photons are separated by a relatively long time delay of $100 - 1000$ ns due to the low indirect exciton recombination rate. In the intermediate state, however, the indirect exciton spin is entangled with the polarization of the first emitted photon (Eq. 4.2). As a result, this scheme could potentially be used to entangle spins in remote CQDs by tuning each of the first emitted photons into resonance via electric or strain fields and performing a joint polarization correlation measurement.[124, 125, 85]

We have used a simple theoretical model to simulate the radiative cascade of the molecular biexciton state in a vertically stacked tunnel-coupled quantum dot pair. The entanglement fidelity of the resulting two-photon polarization state is determined, accounting for phonon-assisted tunneling and spin-flip processes. From numerical simulations, we find an approximately Lorentzian dependence of fidelity on anisotropic electron-hole exchange splitting and mapped the behavior over a range of electric field and temperature values. Our results show that near-unity maximum fidelity can be achieved over a range of exchange splittings $|S_D| < 2.7$ μeV at large exciton detunings and low temperatures, where dephasing due to phonon-assisted hole tunneling and spin-flip processes is suppressed. This suggests that coupled quantum dots can generate photon pairs with a high degree of entanglement and over a wider range of exchange splittings compared to single dots, provided the tunnel coupling is low enough to maintain charge separation in the indirect exciton state. In addition, the spin-photon entanglement generated by the first recombination could be used to entangle spins in remote CQDs.

A similar radiative biexciton cascade has been shown to produce entangled photon pairs in single QDs, but only those with a sufficiently small exchange coupling between the $|\pm 1\rangle$ bright spin states.[90, 105, 126] The primary advantage of

CQDs in this respect is the significant reduction of exchange coupling in the indirect exciton state, in addition to the stronger tunability of interdot transitions by electric field. The remaining challenge is then the low recombination rate of the interdot transition, which generally decreases with electron-hole wavefunction overlap proportionally to the exchange coupling, except in the case of simultaneous electron and hole tunnel coupling.[99] This issue could be addressed effectively by tuning the interdot transition into resonance with a photonic cavity to enhance the recombination rate. Phonon-assisted relaxation to the direct exciton must also be suppressed, which can be achieved by working in the electric field range where the indirect exciton is sufficiently lower in energy.[25] An alternate scheme can also be used which relies on relaxation to the direct exciton state, though an additional nearby charge sensor would be needed to measure and compensate for the phase shift introduced by intradot exchange, increasing the complexity of potential implementations.[98]

4.2 Two-Photon Absorption

In order to use the molecular biexciton radiative cascade in CQDs as a source of polarization-entangled photon pairs, the system must be reliably prepared in the molecular biexciton spin singlet state $|iXX, S\rangle$. The non-resonant excitation used to excite wetting layer continuum or CQD excited states for PL spectroscopy is insufficient, since each CQD charge and spin state is populated randomly by charge capture and phonon-assisted relaxation. A resonant excitation method is desired which can selectively transfer the system from the ground state to the required biexciton state. Inadvertent population of the single-exciton states can be avoided by utilizing a simultaneous two-photon absorption process, rather than a sequential process of exciting into the single-exciton state followed by a second excitation into the biexciton state. Such a two-photon absorption process is commonly implemented with a single laser tuned to half the required transition energy, allowing efficient population of biexciton states in single QDs[126, 18] as well as spin-selective excitation into the $|iXX, S\rangle$ state in CQDs.[127] It can also be implemented using two lasers, detuned from single-photon transitions, whose energies add up to the required transition energy from the ground state to the biexciton state.

Two-photon transitions are amplified when the driving laser is near resonance with one or more intermediate single-photon transitions. To fully utilize the tunability of transition energies in CQDs with applied bias, one can use two lasers independently tuned near resonance with the changing energies of each transition. We seek to understand this two-photon absorption process in the general case of two-laser excitation, with the scheme shown in Fig. 4.5. We use a semiclassical perturbation model similar to that shown in Section 2.3 to describe transitions, with the addition of a second driving field and the inclusion of terms up to second-order in the photon coupling interaction to allow two-photon transitions.

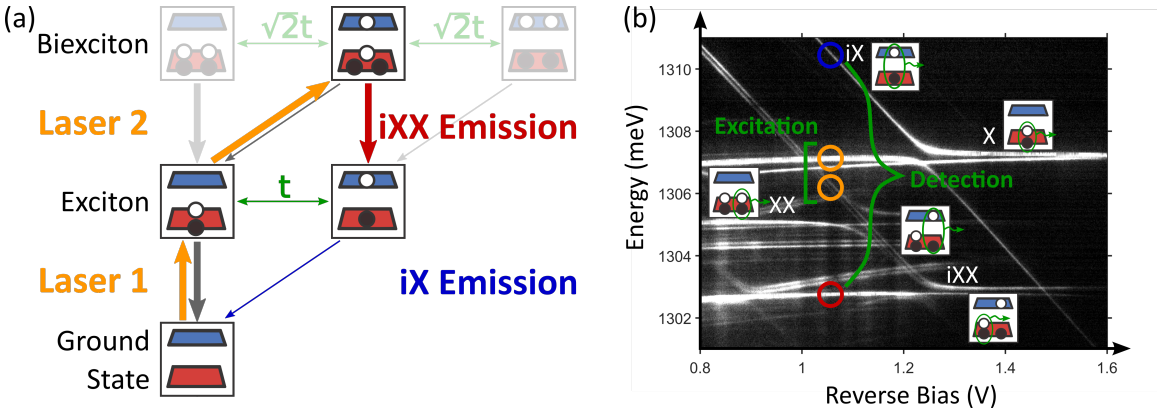

Figure 4.5: (a) Illustration of CQD charge configurations and optical transitions, with two-laser excitation and detection pathways for entangled photon pair emission. (b) PL map with two-laser excitation and detection transitions identified.

Within the long-wavelength approximation, the time-varying electric fields of the two excitation lasers at the position of the CQD can be written as

$$\begin{aligned}\vec{E}_1(t) =& \vec{e}_1\mathcal{E}_1\cos(\omega_1 t+\phi_1)\\ \vec{E}_2(t) =& \vec{e}_2\mathcal{E}_2\cos(\omega_2 t+\phi_2),\end{aligned} \tag{4.19}$$

with frequencies $\omega_{1/2}$, relative phase shifts $\phi_{1/2}$, polarizations $\vec{e}_{1/2}$, and amplitudes $\mathcal{E}_{1/2}$. For simplicity, we consider the case of co-linear horizontal polarization such that $\vec{e}_1 = \vec{e}_2 = \vec{e}_H = \hat{x}$. The electric dipole interaction Hamiltonian $H_I = H_{photon}$ can then be separated into two terms

$$H_I = W_1\cos(\omega_1 t+\phi_1) + W_2\cos(\omega_2 t+\phi_2) \equiv \lambda H' \tag{4.20}$$

describing dipole interaction with each driving field, with the small factor $\lambda \ll 1$ and the elements of H' of the same order of magnitude as H_0 as in the single-laser perturbation theory. The interaction matrix elements between eigenstates $|i\rangle$ and $|k\rangle$ due to laser 1/2 are given by

$$W_{1/2,ik} = -i\mathcal{E}_{1/2}M_{ik}(\vec{e}_{1/2}\cdot\vec{\mu}_{ik}), \tag{4.21}$$

where M_{ik} is the electron-hole envelope wavefunction overlap and $\vec{\mu}_{ik}$ is the bulk optical dipole moment between the spin state of $|i\rangle$ and $|k\rangle$. We consider the scenario where the driving lasers are quasi-resonant with the exciton and molecular biexciton transitions, so that the Hilbert space can be truncated to include only stationary states involved in H-polarized transitions of the molecular biexciton cascade: crystal ground state $|g\rangle$, H-polarized bright direct exciton spin state $|X\rangle = |X^0, H\rangle$, H-polarized bright indirect exciton spin state $|iX\rangle = |iX^0, H\rangle$, and molecular (indirect) biexciton spin singlet state $|iXX\rangle = |iXX^0, S\rangle$.

We expand the time-dependent state vector in the basis of eigenstates $|n\rangle$ of the CQD Hamiltonian H_0, giving

$$|\psi(t)\rangle = \sum_n a_n(t)\,|n\rangle\,. \tag{4.22}$$

Exactly as in Section 2.3, the time-dependent Schrödinger equation

$$i\hbar\frac{d}{dt}\,|\psi(t)\rangle = (H_0 + \lambda H'(t))\,|\psi(t)\rangle \tag{4.23}$$

can be expanded in powers of λ as $a_k = \sum_{n=0}^{\infty}\lambda^n a_k^{(n)}$. Transforming to the interaction picture by replacing each state $|n\rangle$ by $e^{-i\omega_n t}\,|n\rangle$ gives

$$i\hbar\frac{d}{dt}a_k(t) = \lambda\sum_n \langle k|\,H'\,|n\rangle\,a_n(t)e^{i\omega_{kn}t}, \tag{4.24}$$

where $\omega_{kn} = \omega_k - \omega_n$ is the transition frequency. Expanding the coefficients up to second order in the interaction Hamiltonian gives the system of differential equations

$$i\hbar\frac{d}{dt}a_k^{(0)}(t) = 0 \tag{4.25}$$

$$i\hbar\frac{d}{dt}a_k^{(1)}(t) = \sum_n \langle k|\,H'\,|n\rangle\,a_n^{(0)}(t)e^{i\omega_{kn}t} \tag{4.26}$$

$$i\hbar\frac{d}{dt}a_k^{(2)}(t) = \sum_n \langle k|\,H'\,|n\rangle\,a_n^{(1)}(t)e^{i\omega_{kn}t}. \tag{4.27}$$

With the initial condition $|\psi(t=0)\rangle = |i\rangle$, these equations can be solved iteratively to obtain

$$a_k^{(0)}(t) = \delta_{ik} \tag{4.28}$$

$$\lambda a_k^{(1)}(t) = \frac{1}{i\hbar}\int_0^t dt'\ \langle k|\,H'(t)\,|i\rangle\ e^{i\omega_{ki}t} \tag{4.29}$$

$$\lambda^2 a_k^{(2)}(t) = \left(\frac{1}{i\hbar}\right)^2\int_0^t dt'\int_0^{t'} dt''\sum_n \langle k|\,H'(t')\,|n\rangle\,\langle n|\,H'(t'')\,|i\rangle\ e^{i\omega_{kn}t'}\,e^{i\omega_{ni}t''}. \tag{4.30}$$

The two-photon transition rate can be found by solving for the second-order expansion of wavefunction coefficients, defined by

$$\Gamma_{ik}^{(2)} = \frac{P_{i\to k}^{(2)}(T)}{T} = \frac{|\langle k\,|\psi(T)\rangle^{(2)}\,|^2}{T}. \tag{4.31}$$

The probability amplitude for this transition is found by expanding Equation 4.30 to obtain

$$\lambda^2\phi_k^{(2)}(t) = \left(\frac{1}{i\hbar}\right)^2\int_0^t dt'\int_0^{t'} dt''\sum_n \left[W_{1,kn}\cos(\omega_1 t' + \phi_1) + W_{2,kn}\cos(\omega_2 t' + \phi_2)\right] \times \left[W_{1,ni}\cos(\omega_1 t'' + \phi_1) + W_{2,ni}\cos(\omega_2 t'' + \phi_2)\right] e^{i\omega_{kn}t'}e^{i\omega_{ni}t''}. \tag{4.32}$$

Expanding the cosines into complex exponentials and performing the first integration yields

$$\begin{aligned}\lambda^2\phi_k^{(2)}(t) = \frac{i}{4\hbar^2}\int_0^t dt' \sum_n \Big[& W_{1,kn}\left(e^{i[(\omega_1+\omega_k n)t'+\phi_1]} + e^{-i[(\omega_1-\omega_k n)t'+\phi_1]}\right) \\ & + W_{2,kn}\left(e^{i[(\omega_2+\omega_{kn})t'+\phi_2]} + e^{-i[(\omega_2-\omega_{kn})t'+\phi_2]}\right)\Big] \\ \times \Bigg[& W_{1,ni}\left(\frac{e^{i[(\omega_1+\omega_{ni})t'+\phi_1]} - e^{-i\phi_1}}{\omega_1+\omega_{ni}} + \frac{e^{-i[(\omega_1-\omega_{ni})t'+\phi_1]} - e^{-i\phi_2}}{\omega_{ni}-\omega_1}\right) \\ & + W_{2,ni}\left(\frac{e^{i[(\omega_2+\omega_{ni})t'+\phi_2]} - e^{-i\phi_2}}{\omega_2+\omega_{ni}} + \frac{e^{-i[(\omega_2-\omega_{ni})t'+\phi_2]} - e^{-i\phi_2}}{\omega_{ni}-\omega_2}\right)\Bigg]. \end{aligned} \tag{4.33}$$

This expression contains 32 terms for each intermediate exciton state, each with a different set of resonance conditions. Among these, resonances associated with the following processes can be identified:

$$|g\rangle \xleftrightarrow{\omega_1} |X\rangle \xleftrightarrow{\omega_2} |iXX\rangle \tag{4.34}$$

$$|g\rangle \xleftrightarrow{\omega_1} |iX\rangle \xleftrightarrow{\omega_2} |iXX\rangle \tag{4.35}$$

$$|g\rangle \xleftrightarrow{\omega_2} |iX\rangle \xleftrightarrow{\omega_1} |iXX\rangle \tag{4.36}$$

Picking out these resonant terms and performing the final integration gives

$$\begin{aligned}\lambda^2\phi_{iXX}^{(2)}(t) = \frac{i}{4\hbar^2}e^{i(\phi_1+\phi_2)}\Bigg[& \frac{W_{1;X,g}W_{2;iXX,X}}{\delta_1}\left(\frac{e^{-i\delta_{12}t}-1}{\delta_{12}} - \frac{e^{-i\delta_2 t}-1}{\delta_2}\right) \\ & + \frac{W_{1;iX,g}W_{2;iXX,iX}}{\chi_1}\left(\frac{e^{-i\delta_{12}t}-1}{\delta_{12}} - \frac{e^{-i\chi_2' t}-1}{\chi_2'}\right) \\ & + \frac{W_{2;iX,g}W_{1;iXX,iX}}{\chi_2}\left(\frac{e^{-i\delta_{12}t}-1}{\delta_{12}} - \frac{e^{-i\chi_1' t}-1}{\chi_1'}\right)\Bigg], \end{aligned} \tag{4.37}$$

where we have defined the various detunings $\delta_1 = \omega_1 - \omega_{X,g}$, $\delta_2 = \omega_2 - \omega_{iXX,X}$, $\chi_{1/2} = \omega_{1/2} - \omega_{iX,g}$, $\chi'_{1/2} = \omega_{1/2} - \omega_{iXX,iX}$, and $\delta_{12} = \delta_1 + \delta_2 = \omega_1 + \omega_2 - \omega_{iXX,g}$. Due to the quasi-resonant driving of the direct transitions, the δ detunings are assumed to be small. The χ detunings are approximately given by the difference in direct and indirect exciton energies, which is tuned with an applied electric field. In the regime of interest, where $\omega_{iX} \approx \omega_{iXX}/2$, this detuning is on the order of 2-5 meV. In any case, $\delta_i \ll \chi_j$.

To differentiate between transitions through direct and indirect exciton states, we pick out the leading terms associated with each process when calculating the total second-order transition rate, such that $\Gamma^{(2)}_{g,iXX} = \Gamma^{(2)}_X + \Gamma^{(2)}_{iX}$. Keeping only the leading-order terms in δ/χ, we end up with an expression for the two-photon transition rate through the direct exciton states

$$\Gamma_X^{(2)} \approx \frac{\pi}{8\hbar^4}\frac{|W_{1;X,g}|^2|W_{2;iXX,X}|^2}{\delta_1^2}\left[\delta_T(\delta_{12}) + \delta_T(\delta_2) - 2Q_T(\delta_{12},\delta_2)\right] \tag{4.38}$$

and through the indirect exciton states

$$\Gamma_{iX}^{(2)} \approx \frac{\pi}{8\hbar^4}\left|\frac{W_{1;iX,g}W_{2;iXX,iX}}{\chi_1} + \frac{W_{2;iX,g}W_{1;iXX,iX}}{\chi_2}\right|^2 \delta_T(\delta_{12}). \tag{4.39}$$

In these expressions, the function

$$\delta_T(\delta_A) = \frac{\sin^2(\delta_A T)}{\delta_A^2} \tag{4.40}$$

expressing the resonance condition $\delta_A = 0$ has unit area and approaches a delta function as the interaction time $T \to \infty$, but with interaction limited to a finite coherence time its width is given by $2\pi/T$. The function

$$Q_T(\delta_A, \delta_B) = \frac{1 + \cos(\delta_A - \delta_B)T - \cos\delta_A T - \cos\delta_B T}{\pi T \delta_A \delta_B} \tag{4.41}$$

arises from cross terms when taking the modulus squared. It behaves much like $\delta_T(\omega)$, but with two frequencies: its maximum value is T/π as $\delta_A, \delta_B \to 0$, and it quickly becomes zero as δ_A or δ_B are detuned from zero. In the case $\delta_B = \delta_A$, it reduces to $\delta_T(\delta_A)$.

From these calculations, we can see that efficient two-photon absorption requires resonance conditions $\delta_{12} \approx 0$ (the sum of laser energies matches the two-photon transition energy) or $\delta_2 \approx 0$ (the second laser matches the second transition energy), while the transition rate decays with detuning from the first resonance as δ_1^{-2}. If both conditions are satisfied, the third term $2Q_T(\delta_{12}, \delta_2)$ reduces the two-photon transition rate near zero while the single-photon transition rate $\Gamma_{g,X}^{(1)}$ is maximized, resulting primarily in stepwise rather than simultaneous two-photon absorption.

We have measured two-photon absorption by performing two-laser PLE spectroscopy, using two continuous-wave lasers to excite the molecular biexciton state $|iXX\rangle$ and detecting the resulting PL. With one laser resonantly exciting the direct exciton state, absorption into $|iXX\rangle$ can be measured by tuning the wavelength of the second laser and ideally monitoring emission along the other recombination pathway. However, our results thus far have been limited by insufficient rejection of the laser sidebands while detecting PL from transitions $\sim$ 2 meV away from the excitation lasers; we have only been able to clearly detect absorption through the reduction in phonon-assisted emission intensity of the direct exciton (denoted X-1LO) $\sim$ 36 meV below the excitation laser.

The original motivation for this experiment was to measure indirect transitions without the additional broadening due to electric field fluctuations. Whenever an electric field fluctuation δF shifts the energy of the X $\to$ iXX transition (denoted $\mathrm{iXX_i}$) by an amount greater than its linewidth, the resonance conditions are not satisfied and no excitation into iXX occurs. In this way, we hoped to measure the fluctuation-free indirect exciton linewidth.

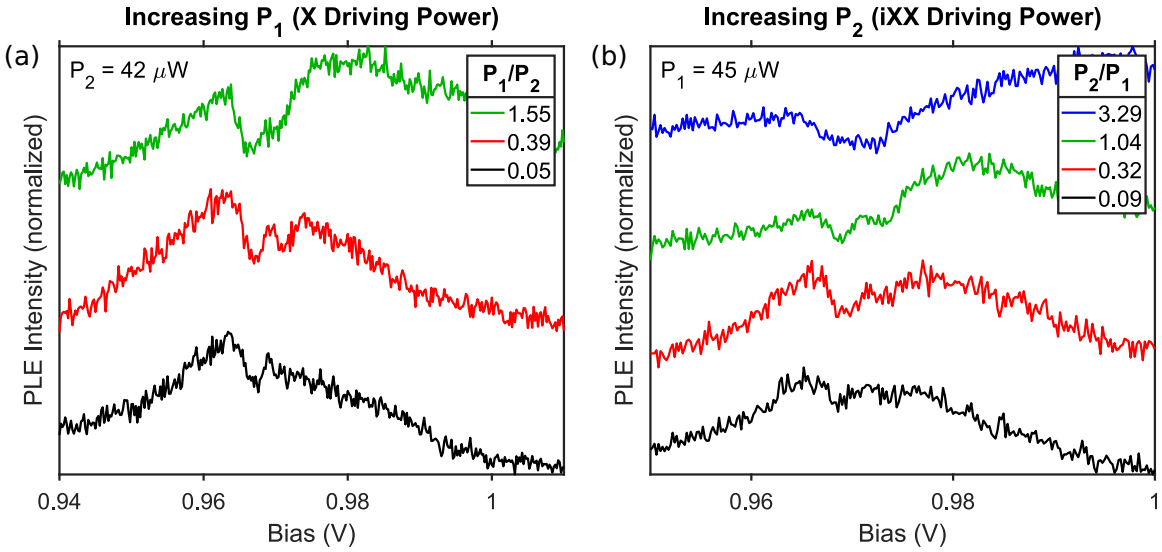

Figure 4.6: Series of X^0 -1LO PLE bias spectra under two-laser resonant excitation, varying (a) X^0 driving laser power and (b) iXX^0 laser driving power.

The experimental PLE spectra are shown in Fig. 4.6 for a series of excitation powers used for each laser, with Stark-shift bias tuning and detection on the X-1LO transition. Absorption into $|X\rangle$ appears as a broad peak due to the small bias slope of the X_d transition. Excitation into the $|iXX\rangle$ state is evidenced by two dips in the PLE peak, corresponding to excitation into one of the singlet or triplet spin states upon resonance with the second laser, resulting in a reduction of $|X\rangle$ population and X-1LO PLE intensity under continuous-wave excitation. The experiment achieved some success in reducing the measured linewidth from 85.0 ± 3.3 μeV with PL to 47.0 ± 4.3 μeV with two-laser PLE, revealing separate transitions involving the iXX singlet and triplet spin states which are obscured in the PL spectrum. As the power of the first laser driving the X_d transition is increased, the total PLE signal is increased and dips due to the second laser are made more visible. As the power of the second laser driving the iXX_i transition is increased, the dips in PLE signal become more prominent and eventually broaden to obscure the spin fine structure.

We model these experimental results using a simple rate equation model for the population dynamics of the involved states, with stepwise excitation by single-photon transitions only. Including effective pumping rates P_1 and P_2 due to each laser, recombination rates Γ_X, Γ_{iX}, Γ_{XX}, and Γ_{iXX}, and phonon-assisted tunneling rates Γ_{abs} and Γ_{em} between exciton states and Γ'_{abs} and Γ'_{em} between biexciton states yields the following system of equations for the populations n_i:

$$\frac{\mathrm{d}}{\mathrm{dt}}\begin{pmatrix} n_g \\ n_X \\ n_{iX} \\ n_{XX} \\ n_{iXX} \end{pmatrix} = M \begin{pmatrix} n_g \\ n_X \\ n_{iX} \\ n_{XX} \\ n_{iXX} \end{pmatrix}, \tag{4.42}$$

with

$$M = \begin{pmatrix} -P_1 & \Gamma_X & \Gamma_{iX} & 0 & 0 \\ P_1 & -(P_2+\Gamma_X+\Gamma_{abs}) & \Gamma_{em} & \Gamma_{XX} & 0 \\ 0 & \Gamma_{abs} & -(\Gamma_{iX}+\Gamma_{em}) & 0 & \Gamma_{iXX_d} \\ 0 & 0 & 0 & -(\Gamma_{XX}+\Gamma'_{abs}) & \Gamma'_{em} \\ 0 & P_2 & 0 & \Gamma'_{abs} & -(\Gamma_{iXX_d}+\Gamma'_{em}) \end{pmatrix}. \tag{4.43}$$

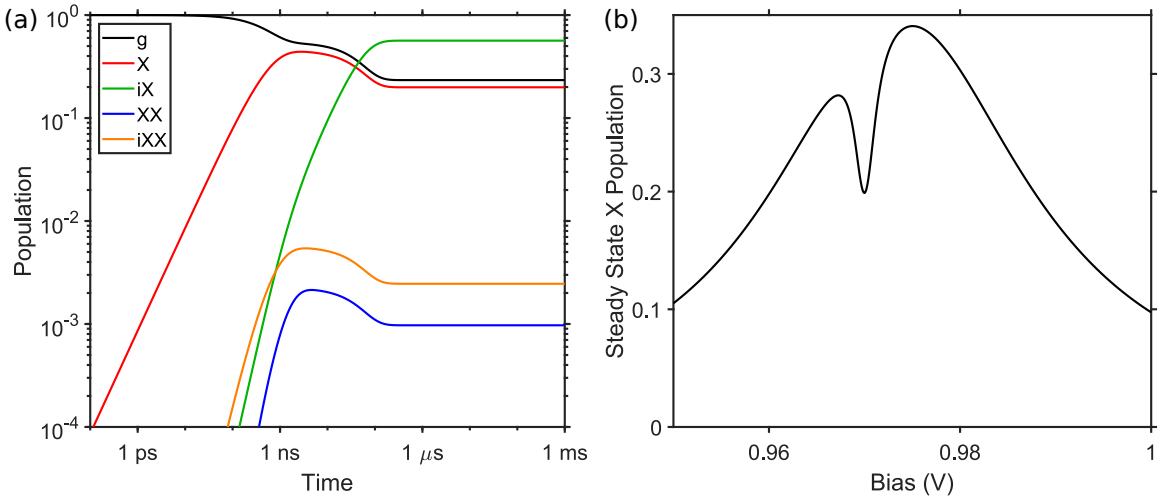

Figure 4.7: (a) Simulated population dynamics under two-laser resonant excitation at 0.97 V applied bias, with initial state $|g\rangle$. (b) Simulated steady state $|X\rangle$ population, proportional to PLE bias spectrum.

The steady-state populations are found by setting rate of change of each population to zero, $d/dt(n_i) = 0$. The resulting population dynamics are shown in Fig. 4.7(a), assuming initialization in the ground state. The calculated steady-state population n_X, proportional to the detected X-1LO PLE intensity, is shown

in Fig. 4.7(b) as a function of applied bias. The dip feature and its intensity relative to the broader peak is reproduced, though only a single dip is seen since the additional $|iXX\rangle$ spin states and their singlet-triplet splitting were neglected in the model. These simulations use effective pumping rates $P_1 = \Gamma_X = 1\,\mathrm{ns}^{-1}$ and $P_2 = 0.0432P_1 = 20\Gamma_{iX}$, and absorption linewidths $\gamma_X = 10\ \mu$eV and $\gamma_{iXX} = 40\ \mu$eV. The bias dependence is taken from

The fact that this model reproduces the experimental results indicates that stepwise excitation by single-photon transitions was the dominant process in these observations. This situation is not ideal for entangled photon pair generation, since a significant portion of the population is driven into the single exciton state, producing single photons and reducing the potential two-photon entanglement fidelity. The experiment could be improved by detuning both lasers from the single-photon transitions while keeping the sum of their energies resonant with the two-photon biexciton transition, thus suppressing stepwise single-photon transitions while maintaining two-photon excitation. The experiment could be further improved by using pulsed laser excitation rather than continuous-wave, enabling coherent Rabi oscillation to efficiently populate the biexciton state rather than the small steady-state component left after relaxation processes.[128, 129, 126, 130]

Chapter 5

Decoherence Mechanisms

QDs show great promise as resources for quantum information technology, either as hosts of solid-state electron or hole spin qubits or as sources of single or entangled photon polarization qubits.[12, 18, 16, 131] CQDs offer additional benefits due to their enhanced tunability of energy levels and coupling strengths, as well as their expanded space of charge and spin states.[21] However, each of these applications requires that bound charges initialized into a particular state will evolve coherently in time until read out by optical recombination or acted on by a control pulse.

According to the time-dependent Schrödinger equation

$$i\hbar\frac{\partial}{\partial t}\left|\Psi(t)\right\rangle = H\left|\Psi(t)\right\rangle, \tag{5.1}$$

a system prepared in an eigenstate $|\Psi(0)\rangle = |n\rangle$ with $H|n\rangle = E_n|n\rangle$ will undergo coherent evolution $|\Psi(t)\rangle = e^{-iE_nt/\hbar}|n\rangle$ with a complex oscillating phase. Quantum information technologies require that a second qubit system prepared simultaneously in a similar eigenstate, or a second indistinguishable decay pathway in the case of entangled photon emission, will evolve with a fixed phase relationship relative to the first to enable the desired quantum interference effects. This coherent phase evolution can be interrupted by several types of decoherence processes which randomize the phase, broadening optical transition linewidths and preventing quantum interference effects with similarly prepared states. The first class of decoherence mechanism results from transitions to other states $|m\rangle \neq |n\rangle$ at rates γ_{nm}, with the state $|n\rangle$ having a finite lifetime $\tau_n = (\sum_m \gamma_{nm})^{-1}$. The second class of decoherence mechanism results from variations in the energy $E_n(t)$ due to interactions with phonon modes or fluctuating external fields. This mechanism is referred to as pure dephasing, with no population transfer and an effective dephasing rate γ_{nn}.

Section 5.1 describes experimental measurements of pure dephasing due to a fluctuating local electric field, with simulations supporting a hypothesis of charge trapping at nearby defect sites. Section 5.2 presents measurements of phonon-assisted transitions between exciton states, with a theoretical model explaining phonon coupling mechanisms and simulations suggesting enhanced coupling at tunneling resonances.

5.1 Charge Fluctuations

The energy of exciton states, both direct and indirect, depends quadratically on the electric field F across the CQD due to the quantum-confined Stark effect:[57]

$$E_X(F) = E_0 + pF + \beta F^2.$$

Indirect excitons, though, exhibit a much larger permanent dipole moment $p = -ed$ as a result of charge separation d between dots. This allows indirect exciton transition energies to be tuned linearly with applied field over a wide range, as can be seen in the field-dispersed PL map of Fig. 3.3(c). It could also enable detection of individual nearby charges using resonant optical excitation. Conversely, however, indirect excitons are particularly susceptible to fluctuations in transition energy $\delta E \approx -ed\,\delta F$ due to a small electric field fluctuation δF.

Previous studies of charge noise in similar semiconductor QD heterostructures have determined the primary source of electric field fluctuations to be charges trapped at the interface nearest to the QDs, fluctuating on a time scale of milliseconds or longer.[132, 133, 134, 135]

5.1.1 Line Wandering

When charge fluctuations occur on a timescale longer than the experimental integration time of $T_{int} = 1$ s, the resulting change in energy can be seen as a changing peak energy in PL spectra. This has been observed primarily in patterned samples with CQDs in suspended membrane or cantilever structures. In these samples, the sacrificial AlGaAs layer removed by chemical undercutting leaves an exposed surface near the CQD layers (within 120 nm) where lattice defects are more likely to form. The formation of defects and their population and depopulation by optical excitation and charge tunneling are both stochastic processes, so even within similar structures across a single sample there can be significant variation in the distribution of charge traps and the strength of line wandering effects.

Some examples of this observation are shown in Fig. 5.1 for CQD D1 near the base of a suspended membrane structure. CQD D1 shows dramatic shifts in the energy of multiple PL peaks during each of the five-minute observation periods. PL peaks remain stable for $\sim 1 - 30$ s, with discrete shifts up to 1 meV resulting in variations up to $\sim$5 meV on timescales of minutes. The assignment of these shifts as local electric field fluctuations due to charge trap occupation is supported by the presence of multiple PL transitions from the same CQD which all undergo identical shifts in energy. In addition, PL transitions from a second nearby CQD (with lower intensity due to relative misalignment) undergo discrete shifts mostly at the same times, but with different magnitudes and directions due to its slightly different position and local electric field value.

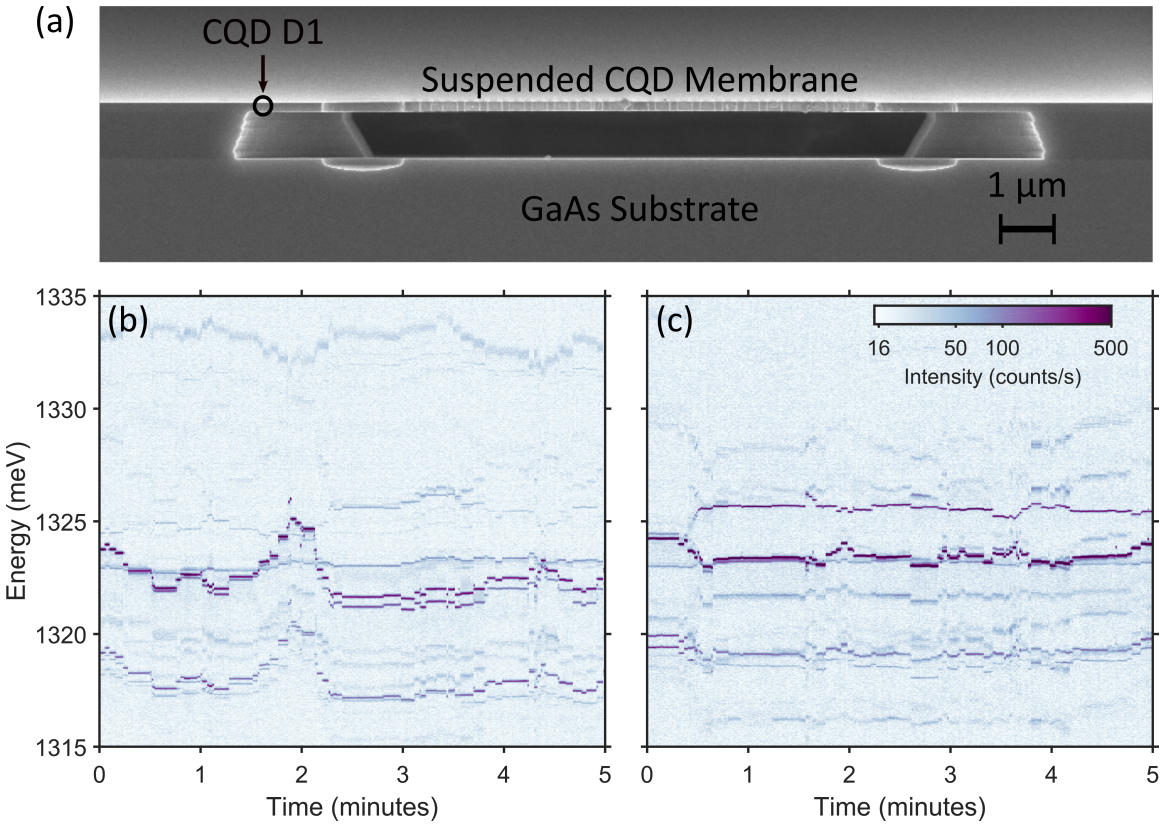

Figure 5.1: (a) Scanning electron micrograph of suspended membrane structure of sample D, indicating position of CQD D1 with severe charge fluctuations. (b) (c) Subsequent PL spectra as a function of time for CQD D1.

5.1.2 Interdot Broadening

Experimental PL and PLE spectra of interdot transitions often show a smooth, approximately Gaussian broadened lineshape. This situation can arise if the local electric field fluctuates at a rate slower than the exciton lifetime (1-100 ns) yet much faster than the measurement duration ($1 - 30$ s for PL, $1 - 20$ minutes for PLE), so that the narrow lifetime-limited Lorentzian lineshape is averaged over a distribution of resonance energies.

If we assume that the interdot transition of interest has a narrow lifetime-limited Lorentzian PL spectrum

$$I_{iX}(E,t) = I_{iX}\left[1 + \frac{4(E - E_{iX}(t))^2}{\Gamma_{iX}^2}\right]^{-1} \tag{5.2}$$

with lifetime $\tau_{iX} = \Gamma_{iX}^{-1}$ and peak intensity I_{iX}, then the spectrum detected experimentally over the integration time T_{int} is given by

$$\bar{I}_{iX}(E) = \int_0^{T_{int}} I_{iX}(E,T)\,dt. \tag{5.3}$$

If charge fluctuations are due to many randomly-distributed charge traps, they can be approximated by a Gaussian probability density function

$$P(\delta F) = \frac{1}{\sigma\sqrt{2\pi}} \exp\left(-\frac{\delta F^2}{2\sigma^2}\right) \tag{5.4}$$

with standard deviation σ corresponding to a full-width at half-maximum (FWHM) of $2\sqrt{2\ln 2}\,\sigma \approx 2.35\,\sigma$. When many charge fluctuations occur rapidly, the system approaches the ergodic limit where the entire probability distribution is explored within each spectrum acquisition. In this limit, the experimentally detected spectrum is given by the Voigt lineshape (convolution of Gaussian and Lorentzian)

$$\bar{I}_{iX}(E) = \int_{-\infty}^{\infty} P(\delta F)\, I_{iX}(E - ed\delta F)\, d(\delta F). \tag{5.5}$$

Finally, if the standard deviation $ed\sigma$ of the energy shifts due to field fluctuations is much larger than the lifetime-limited linewidth Γ_{iX}, the detected spectrum is almost entirely given by the distribution of field fluctuations around the average energy $\langle E_{iX}\rangle$:

$$\bar{I}_{iX}(E) \approx I_{iX}\, P\left[-(E - \langle E_{iX}\rangle)/ed\right]. \tag{5.6}$$

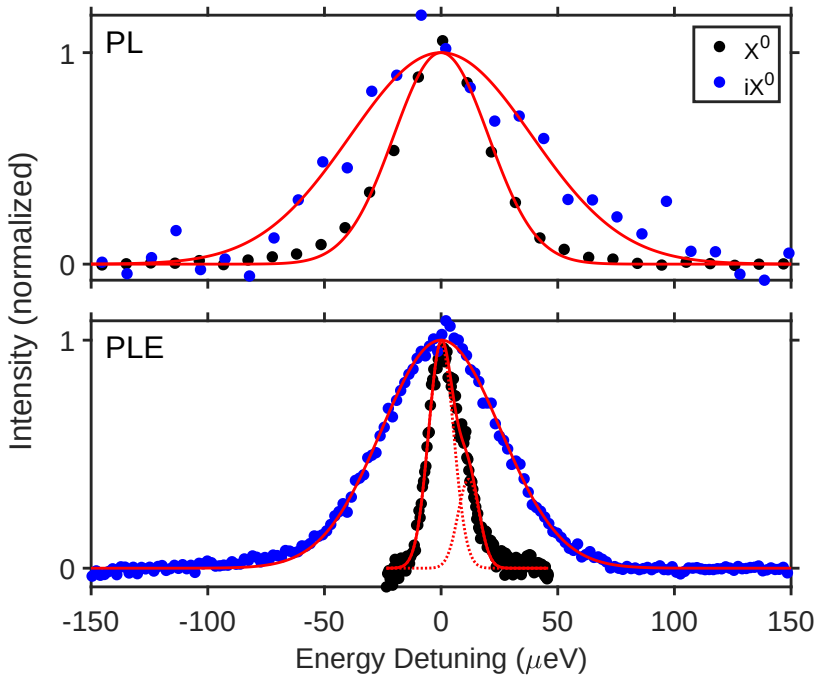

Figure 5.2: Experimental PL emission and PLE absorption lineshapes of X^0 and iX^0 transitions, with Gaussian fits (solid lines) and spin components (dotted lines) where visible.

Fig. 5.2 shows the experimentally detected optical spectra of the direct and indirect exciton transitions in a CQD, with the emission spectrum probed by PL and

the absorption spectrum probed by PLE. Since indirect excitons have the electron and hole trapped in separate QDs, their optical recombination rate is much slower and their lifetime much longer than direct excitons. In the absence of charge fluctuations, we would therefore expect indirect transitions to have a much narrower spectrum than direct transitions. However, experimental observations reveal the opposite—PL spectroscopy shows a linewidth of 47.8 ± 0.5 μeV (limited by spectrometer resolution) for the direct transition and 92 ± 6 μeV for the indirect transition, while PLE spectroscopy shows a linewidth of 12.7 ± 0.2 μeV (for each of two resolved spin states) for the direct transition and 60.1 ± 0.4 μeV for the indirect transition.

In each case, the indirect transition is broader than the direct transition, pointing to charge fluctuations as the primary broadening mechanism. The additional broadening in PL relative to PLE means that charge traps are occupied more often under higher-energy optical excitation, resulting in larger electric field fluctuations. The smooth Gaussian shapes of experimentally observed spectra indicate a large number of distant charge traps, such as those formed during growth at a heterojunction interface.

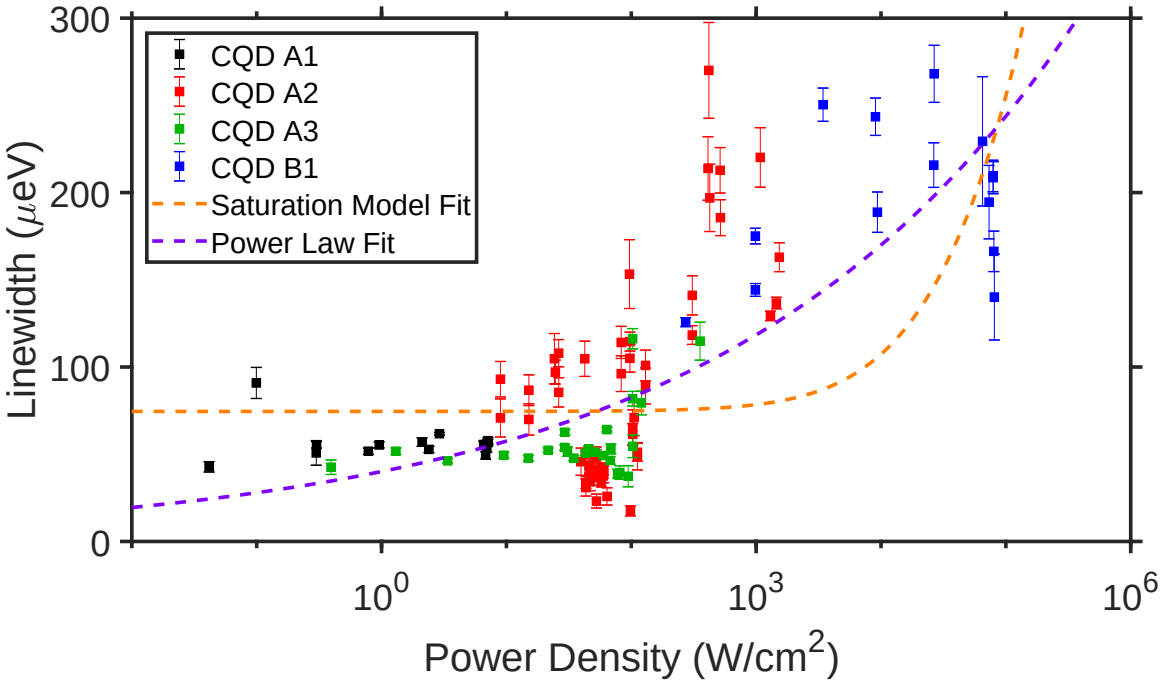

Figure 5.3: Experimental iX^0 PLE linewidth as a function of power density for multiple CQDs on different samples, with fits to saturation and power law models.

Fig. 5.3 shows the PLE linewidths of indirect transitions as a function of power density of the resonant excitation laser, compiled for multiple CQDs across two similar Schottky diode samples. While no single CQD was measured over the entire range of power densities, the combined data shows a common trend of increasing linewidth with power density. One common explanation for power broadening is saturation of a two-level system, which would yield a linewidth of $\Gamma(P) = \Gamma_0\sqrt{1 + P/P_0}$

with a low-power linewidth Γ_0 and significant broadening past the saturation power density P_0. However, the data much more closely follows a power law dependence $\Gamma(P) = \Gamma_0 + AP^x$ with $x = 0.16 \pm 0.02$. While the exact mechanism is not fully understood, this trend suggests that charge fluctuations are generated by optical excitation, even under resonant conditions.

5.1.3 Monte Carlo Simulations

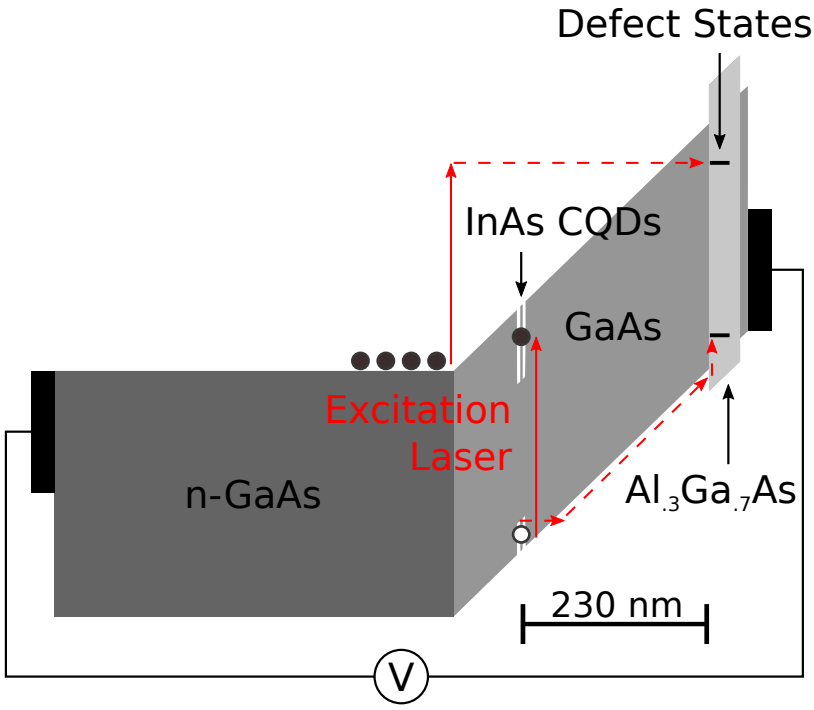

Figure 5.4: Band edge diagram of CQD diode structure, with illustration of defect charging mechanisms under resonant excitation.

Fig. 5.4 illustrates some potential mechanisms of defect charging under resonant CQD excitation, with a laser energy below the bandgap of bulk GaAs. Charge traps can be formed by lattice defects at the material interface between GaAs and AlGaAs layers, with states either just below the conduction band edge to trap electrons or just above the valence band edge to trap holes. In addition to the targeted interband transitions between CQD bound states, the laser can excite conduction electrons from the n-doped substrate into higher-energy conduction states, enabling them to migrate through the intrinsic region of the diode and tunnel into defect states. Alternatively, valence-band holes can tunnel out of CQD bound states and migrate to the AlGaAs barrier, forming a two-dimensional hole gas or becoming trapped in localized defect states.

Markov chain Monte Carlo simulations of charged lattice defects were performed to reproduce experimental observations of CQDs in different diode structures,

giving insight into their spatial distribution and dynamics. Following the approach of Kuhlmann et al.[133], we model the charge traps as identical two-state systems (unoccupied $|0\rangle$ or occupied $|1\rangle$) with a constant lifetime τ_0 and τ_1 for each state. The time-averaged occupation probability is determined by the lifetimes as $p_1 = \tau_1/(\tau_0+\tau_1)$, so that only two of these three quantities can be set independently. The time evolution of an ensemble of charge traps is simulated using the Markov Chain Monte Carlo method, where a random number generator is used to set the initial state of each trap according to a given occupation probability and to update the state of each trap at every subsequent time step. The probability that a charge capture transition will occur during each time step δt is given by

$$p_{0\to1}(\delta t) = 1 - \frac{\tau_0 + \tau_1\, e^{-\delta t(\tau_0^{-1}+\tau_1^{-1})}}{\tau_0+\tau_1}, \tag{5.7}$$

while the probability of a charge escape transition during the same time step is given by

$$p_{1\to0}(\delta t) = 1 - \frac{\tau_1 + \tau_0\, e^{-\delta t(\tau_0^{-1}+\tau_1^{-1})}}{\tau_0+\tau_1}. \tag{5.8}$$

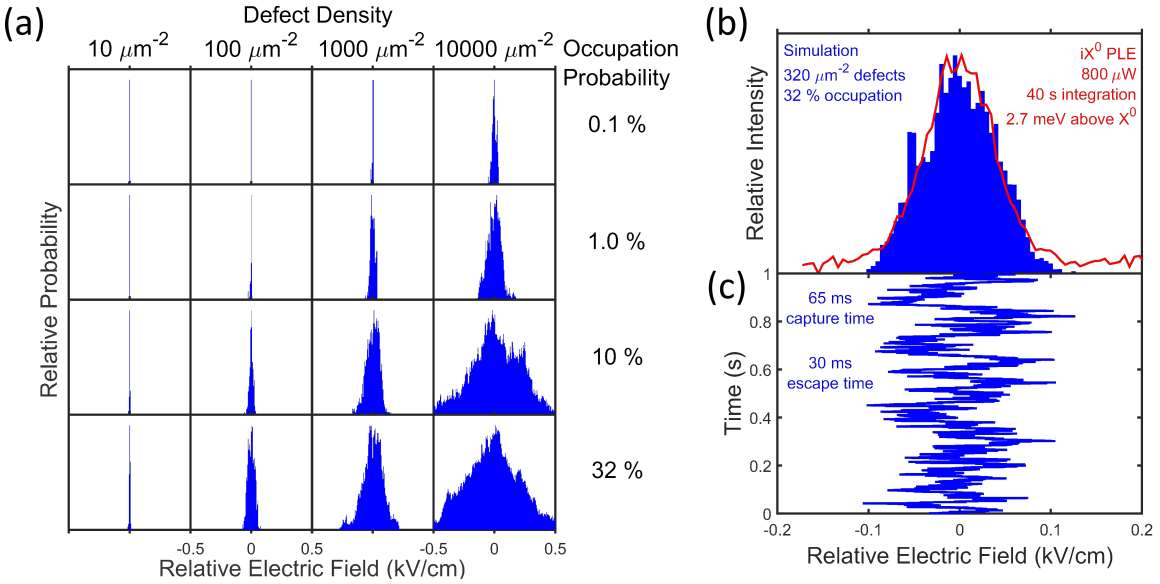

Figure 5.5: (a) Simulated probability distribution of electric field fluctuations for defects located at the GaAs/AlGaAs interface 230 nm above the CQDs, with varying defect densities and average occupation probabilities. (b) Simulated probability distribution of electric field fluctuations for 320 μm^{-2} defect density and 32% occupation probability, compared to experimental iX^0 PLE spectrum. (c) Relative electric field as a function of time for the simulation shown in (b).

To model interface charge fluctuations, we randomly distribute an ensemble of charge traps within a plane at a distance $d = 230\,\text{nm}$ from the quantum dots,

corresponding experimentally to the GaAs/AlGaAs interface, with a chosen average in-plane density N_d of defects. Since the permanent dipole moment of an interdot exciton is primarily oriented in the growth direction, only the component of electric field in this direction will contribute to the observed Stark shift. In a dielectric medium with relative permittivity ϵ_r (12.9 in GaAs), each charge trap at an in-plane distance r from the CQD axis will contribute an electric field component

$$\Delta F_z = \frac{-e}{4\pi\epsilon_0\epsilon_r}\frac{d}{(r^2+d^2)^{3/2}} \tag{5.9}$$

when occupied by a single hole. To limit the number of simulated charge traps, we consider only those within a $1\,\mu$m in-plane distance from the CQD axis.

With the charge escape time fixed at $\tau_1 = 30\,\text{ms}$, corresponding to the findings of Kuhlmann et al., we vary the defect density N_d and occupation probability p_1 and observe the simulated probability distribution of electric field values averaged over a duration $T = 1\,\text{s}$. As shown in Fig. 5.5(a), the width of the electric field distribution increases with N_d or p_1, as additional charge traps are present and they change state more often. While not shown here, the trend in occupation probability is inverted at higher values, with a maximum distribution width at $p_1 = 50\,\%$. The experimental interdot PLE transition lineshape is most closely reproduced with the values $N_d = 320\,\mu\text{m}^{-2}$ and $p_1 = 32\,\%$, as shown in Fig. 5.5(b) and (c).

The close correspondence of simulations and experiments support the idea that the observed broad lineshape of indirect transitions is due to fluctuating charge states of many defect sites located at the nearest material interface, with a high average occupancy. Low-power resonant excitation minimizes charge fluctuations, while higher-power excitation results in photoinduced current and defect charging. The distance between the CQD and the nearest material interface is a critical parameter for determining charge noise in diode structure design, with a closer interface resulting in much larger field fluctuations.

5.2 Phonon Interactions

5.2.1 Phonon Coupling Theory

Coupling between single bound charges and lattice phonons can be described using the general Hamiltonian

$$\begin{aligned} H_{e-ph} = &\sum_{s,\vec{q}} (b_{s,\vec{q}} + b^\dagger_{s,-\vec{q}}) \\ &\times \left[\sum_{ij} c_i^\dagger c_j F^e_{s,ij}(\vec{q}) - \sum_{kl} d_k^\dagger d_l F^h_{s,ij}(\vec{q})\right], \end{aligned} \tag{5.10}$$

with creation (annihilation) operators $b^\dagger_{s,\vec{q}}$ ($b_{s,\vec{q}}$) for phonon modes with polarization $s = \{\text{LA}, \text{TA}_1, \text{TA}_2\}$ and wave vector $\vec{q}$, $c_i^\dagger$ (c_i) for electrons in state $|i\rangle$, and $d_k^\dagger$ (d_k)

for holes in state $|k\rangle$. The phonon coupling constants are expanded into bulk and localized contributions as $F^{\alpha}_{s,ij}(\vec{q}) = g^{\alpha}_{s}(\vec{q})\mathcal{F}^{\alpha}_{nm}(\vec{q})$, with bulk coupling matrix elements $g^{\alpha}_{s}(\vec{q})$ depending on phonon mode and coupling mechanism and geometric form factors

$$\mathcal{F}^{\alpha}_{ij}(\vec{q}) = \langle \alpha_i | \, e^{i\vec{q}\cdot\vec{r}} \, | \alpha_j \rangle = \int \psi^{\alpha *}_{i}(\vec{r}) e^{i\vec{q}\cdot\vec{r}} \psi^{\alpha}_{j}(\vec{r}) \, d^3\vec{r} \tag{5.11}$$

describing overlap of the envelope wavefunctions of involved states modulated by the phonon mode phase.

Since we are interested in transitions between the two lowest-energy neutral exciton states near a tunneling resonance, the relevant energy differences are less than 15 meV, so coupling to optical phonons at energies of 30-40 meV is neglected. The relevant phonon coupling mechanisms which contribute to the bulk matrix element $g^{\alpha}_{s}(\vec{q})$ therefore include deformation potential (DP) coupling to LA phonons, given by

$$g^{e/h(DP)}_{LA}(\vec{q}) = \sqrt{\frac{\hbar q}{2\rho V c_{LA}}} a_{c/v}, \tag{5.12}$$

and piezoelectric (PE) coupling to LA and TA phonons, given by

$$g^{\alpha(PE)}_{s}(\vec{q}) = -i\sqrt{\frac{\hbar}{2\rho V c_s q}} \frac{d_P e}{\epsilon_0 \epsilon_r} M_s(\hat{q}). \tag{5.13}$$

In equations (5.12) and (5.13), ρ is the mass density of the crystal, V is the crystal volume used for normalization of phonon modes (cancels out after summation over wave vectors), c_s is the propagation velocity of phonon mode s, $a_{c/v}$ is the deformation potential of the conduction/valence band, d_P is the piezoelectric constant of the crystal, $\epsilon_0\epsilon_r$ is the electric permittivity of the crystal, and the directional dependence of the PE coupling is given in terms of the phonon mode polarization vectors $\hat{e}_{s,\vec{q}}$ as

$$M_s(\hat{q}) = 2\left[\hat{q}_x(\hat{e}_{s,\vec{q}})_y\hat{q}_z + \hat{q}_y(\hat{e}_{s,\vec{q}})_z\hat{q}_x + \hat{q}_z(\hat{e}_{s,\vec{q}})_x\hat{q}_y\right]. \tag{5.14}$$

Note that these bulk coupling matrix elements assume a constant value of each material parameter, without taking into account variations in composition due to the CQD structure. Previous studies therefore assume that these parameters are determined entirely by the GaAs barrier material, or by assuming a uniform effective composition.[112, 66] Using the orthonormal set of phonon mode polarization vectors

$$\begin{aligned} \hat{e}_{LA,\vec{q}} \equiv \hat{q} &= (\cos\phi\sin\theta, \sin\phi\sin\theta, \cos\theta) \\ \hat{e}_{TA_1,\vec{q}} &= (-\sin\phi, \cos\phi, 0) \\ \hat{e}_{TA_2,\vec{q}} &= (\cos\phi\cos\theta, \sin\phi\cos\theta, -\sin\theta), \end{aligned} \tag{5.15}$$

equation (5.14) for each phonon mode becomes

$$\begin{aligned} M_{LA}(\hat{q}) &= \frac{3}{2}\sin(2\phi)\sin(2\theta)\sin\theta \\ M_{TA_1}(\hat{q}) &= \cos(2\phi)\sin(2\theta) \\ M_{TA_2}(\hat{q}) &= \sin(2\phi)\sin\theta(3\cos^2\theta - 1). \end{aligned} \tag{5.16}$$

Evaluation of the geometric form factors $\mathcal{F}_{ij}^{\alpha}(\vec{q})$ defined in Eq. (5.11) involves integration over a three-dimensional grid of spatial coordinates for each value of the phonon wave vector on a separate three-dimensional grid, thereby constituting a major bottleneck in numerical calculations. Ref. [112] uses the cylindrical symmetry of the envelope wavefunctions to simplify these integrals by separating variables and evaluating the angular integral in terms of m'th-order Bessel functions of the first kind $\mathcal{J}_m(a)$. For the separable ground-state wavefunctions defined in Eq. (2.23) and phonon wave vectors defined in cylindrical coordinates as $\vec{q} = (q_r, \phi, q_z)$, this expression becomes

$$\begin{aligned}\mathcal{F}_{ij}^{\alpha}(\vec{q}) =& 2\pi \int_0^{\infty} e^{-m_\alpha \omega_\alpha r^2/\hbar} \mathcal{J}_0(q_r r)\, r dr \\ & \times \int_{-\infty}^{\infty} Z_i(z) e^{iq_z z} Z_j(z)\, dz.\end{aligned} \tag{5.17}$$

The rate of phonon-assisted tunneling transitions from state $|n\rangle$ to state $|m\rangle$ due to first-order coupling is given by Fermi's golden rule as

$$\gamma_{nm} = \frac{2\pi}{\hbar^2} \left[n_B(T, |\omega_{nm}|) + \Theta(\omega_{nm}) \right] J_{nm}(|\omega_{nm}|), \tag{5.18}$$

where the phonon spectral density

$$J_{nm}(\omega) = \sum_{s,\vec{q}} \left| F_{s,nm}^{X}(\vec{q}) \right|^2 \delta(\omega - \omega_{s,\vec{q}}) \tag{5.19}$$

measures the coupling to phonon modes at the transition frequency $\omega_{nm} = (E_n - E_m)/\hbar$ to ensure energy conservation, the temperature-dependent phonon mode population is given by the Bose distribution $n_B(T, \omega) = (e^{\hbar\omega/k_B T} - 1)^{-1}$, and the step function $\Theta(\omega_{nm}) = 0\,(1)$ for phonon absorption (emission). The summation over phonon modes can be represented in spherical coordinates $\vec{q} = (q, \phi, \theta)$ as an integral over wave vectors with a fixed magnitude:

$$\begin{aligned}J_{nm}(\omega) =& \frac{V}{(2\pi)^3} \sum_s \frac{\omega^2}{c_s^3} \\ & \times \int_0^{\pi} \int_0^{2\pi} \left| F_{s,nm}^{X}\left(\omega/c_s, \phi, \theta\right) \right|^2 \sin\theta\, d\phi d\theta,\end{aligned} \tag{5.20}$$

where the dispersion relation $E = \hbar\omega = \hbar c_s q$ is used to relate wave vector magnitude to the mode-dependent group velocity v_s, and the mode volume V cancels with the corresponding factor in the bulk coupling constants $g_s^{\alpha}(\vec{q})$.

5.2.2 Anticrossing Enhancement

Here, we focus our analysis on the spectral broadening of the neutral exciton optical transitions, which generate the two most prominent lines in the electric field dispersed PL spectrum of Fig. 5.6a. The two transitions form an anticrossing (AC) in the

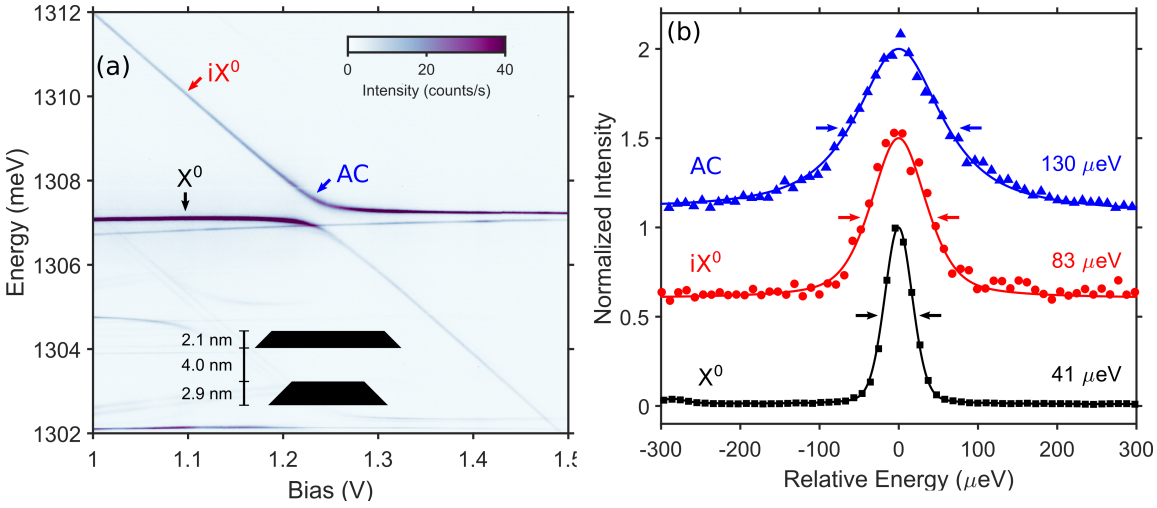

Figure 5.6: (a) Electric field dispersed emission spectra of CQD 1 measured at 20 K near a neutral exciton hole tunneling resonance. Inset shows CQD geometry with QD heights and interdot barrier width. (b) Line profiles of direct (X^0, black squares) and indirect (iX^0, red circles) optical transitions at 1.1 V compared with the upper branch tunneling resonance (AC, blue triangles) at 1.24 V, with Voigt fits (solid lines) and FWHM linewidth values indicated.

center of the image. This anticrossing is a result of a hole level resonance between a direct exciton (X^0), with an electron and hole in the bottom dot, and an indirect exciton (iX^0), with an electron in the bottom dot and hole in the top dot. The PL emission energy of the direct exciton shows a weak dependence on electric field, while that of the indirect exciton shows a strong electric field dependence. This difference in response to the electric field is a result of the static dipole moment $p = \pm ed$, defined by the elementary charge e and the spatial separation d of electron and hole. The avoided crossing is the spectral signature of the formation of molecular states, i.e. the symmetric and anti-symmetric mixing of the direct and indirect excitons wavefunctions, $|\psi\rangle = \alpha\,|X\rangle \pm \beta\,|iX\rangle$.[56] The resulting exciton state, $|\psi\rangle$, should exhibit properties in between that of the direct and the indirect exciton. For example, at the center of the anticrossing the Stark shift is the average of the Stark shift observed for the direct and indirect excitons. Likewise, the radiative lifetime at the center of the anticrossing can be expected to be the arithmetic average of the lifetimes of both exciton states. Consequently, if we were to measure the linewidth of the exciton transition as we follow one of the anticrossing branches through the anticrossing region, i.e. from the direct exciton to the indirect exciton, we expect the linewidths to gradually and monotonically decrease in the absence of nonradiative broadening mechanisms.

The line profiles for three different exciton states X^0, iX^0, and tunneling resonance are shown in Figure 5.6b. The solid lines are pseudo-Voigt fits to the experimental data, evaluated as a linear combination of Lorentzian and Gaussian

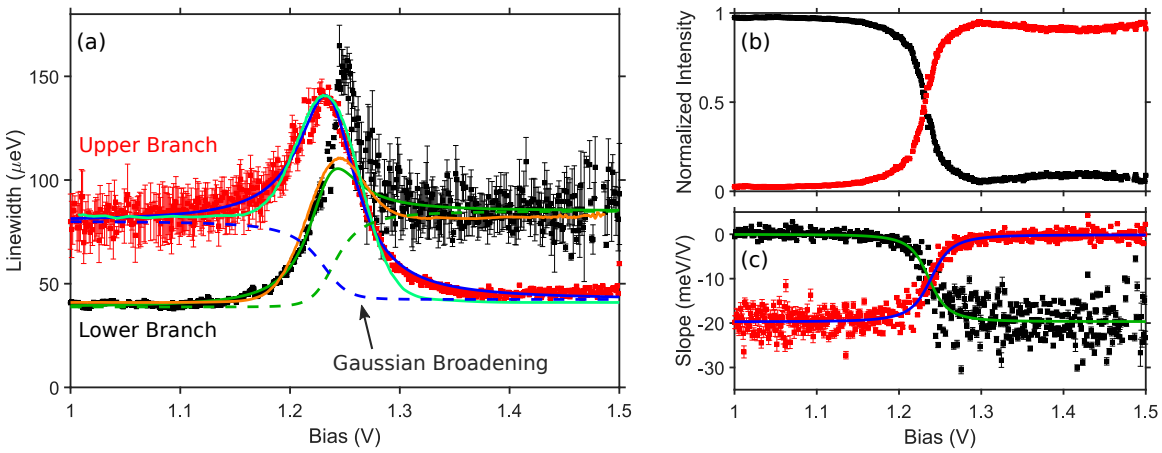

Figure 5.7: (a) Measured linewidth of the lower (black squares) and upper (red circles) branches of the X^0 anticrossing in CQD 1 at 20 K as a function of bias, with fits to Eq. (5.29) (solid lines), the results of numerical simulations (dash-dotted lines), and Gaussian broadening components (dashed lines). (b) Relative intensity of each branch, normalized to the sum of the two intensities at each bias value. (c) Measured bias slope of each branch, with fits to Eq. (5.25) (solid lines).

lineshapes. The linewidth of the direct exciton corresponds to the resolution limit of our experimental setup, 41.4 ± 0.1 μeV. In contrast, we find that the PL linewidth of the indirect exciton is 83 ± 5 μeV, while the linewidth at the upper branch of the anticrossing is 130 ± 3 μeV. In resonant measurements, resolution limited by the laser linewidth, such as described by Czarnocki et al.,[69] we have been able to show that the actual transition linewidth of the direct exciton is on the order of a few μeV, consistent with the typical radiative lifetimes for InAs/GaAs QDs.[136] For the indirect exciton one would expect a much-reduced linewidth, due to the reduced overlap of the electron and hole wavefunctions. That the indirect exciton transitions exhibit the opposite, a larger linewidth than the direct exciton transitions, has been attributed to charge fluctuations near the CQDs and the larger static dipole moment.[57, 137, 134] Regardless of this inverted behavior of the linewidths, we expect a gradual and monotonic change of the exciton transition linewidth as we follow one of the branches through the anticrossing.

In contrast to the expected behavior, we find a non-monotonic change of the PL linewidth. Towards the center of the anticrossing the linewidth increases to values significantly above that of the indirect exciton. In the example shown in Fig. 5.7a, the linewidth of the upper branch broadens at the tunneling resonance to 139 ± 1 μeV compared to 42.5 ± 0.6 μeV in the limit of the direct exciton transition and 80.6 ± 0.6 μeV in the limit of the indirect exciton transition, with similar values for the lower branch. We investigated more than 20 molecules and observed linewidth broadening up to ~ 300 μeV at the tunneling resonance. Theoretical work by Daniels *et al.* suggests that the linewidth broadening at the anticrossing is the result of enhanced phonon coupling.[66] They find that at the tunneling resonances

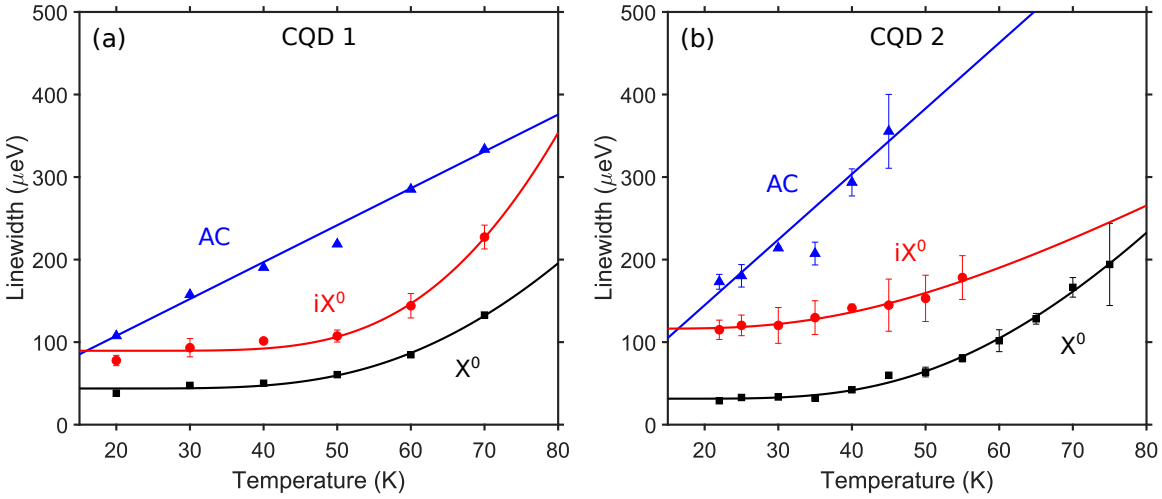

Figure 5.8: Measured temperature-dependent ZPL linewidths for (a) CQD 1 and (b) CQD 2 at and away from the center of the anticrossing, with linear and phonon-activated broadening fits (solid lines).

where the two involved exciton states come closest in energy to each other, transition rates between the two branches assisted by the emission or absorption of phonons are enhanced.

The relative intensities of the upper and lower exciton branches are shown in Fig. 5.7b. The intensity of each branch is equal near the tunneling resonance, where the wavefunction overlap is maximized. The indirect exciton becomes significantly weaker in intensity away from the tunneling resonance, leading to increased uncertainty of linewidth fit values. The slope (change in exciton peak energy as a function of applied bias) of the upper and lower branches is shown in Fig. 5.7c, and follows the predicted dependence of Eq. 5.25 with equal slopes at the tunneling resonance.

The temperature dependence of the PL linewidth is shown in Fig. 5.8 for two CQDs on the same sample, with the theoretical dependence given by Eq's. (5.18) and (2.51). At low temperatures, the linewidth is determined by the one-phonon transition rate between the lowest two eigenstates, with the temperature dependence entering through the phonon mode population $n_B(T, \omega_{21})$ at the transition frequency. The energy splitting $\hbar\omega_{21}$ at the anticrossing is significantly smaller than the thermal energy $k_B T$ in these measurements, leading to the observed linear broadening for the upper branch

$$\frac{\partial \Gamma_2}{\partial T} \approx \frac{\pi}{\hbar} \frac{k_B}{\hbar \omega_{21}} J_{12}(\omega_{21}). \tag{5.21}$$

The slope of this linear broadening, measured as 4.5 ± 0.4 μeV/K for CQD 1 and 7.9 ± 2.1 μeV/K for CQD 2, is therefore proportional to the interdot phonon coupling strength through the spectral density $J_{12}(\omega_{21})$ at the transition frequency. We expect that the linewidth at the anticrossing would approach a constant value at lower temperatures between $5 - 15$ K where the thermal energy decreases below the energy splitting.

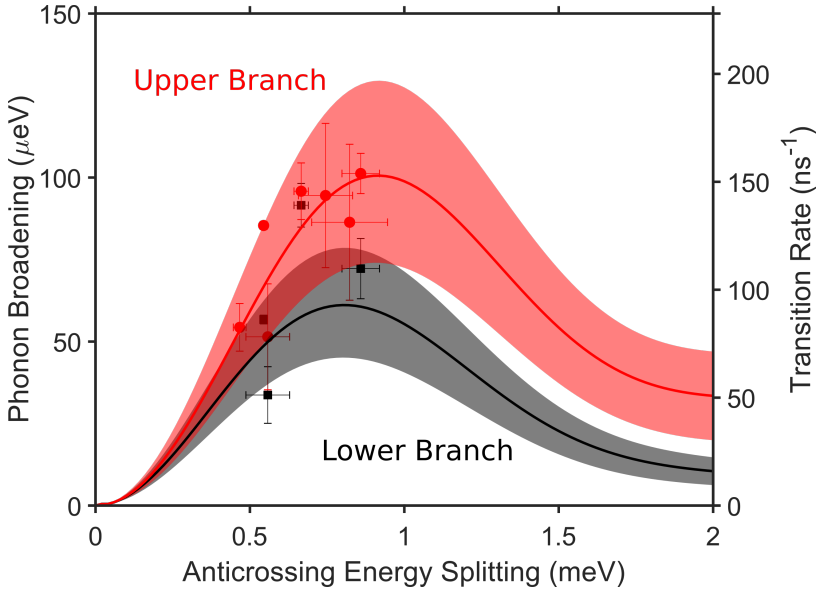

Figure 5.9: Phonon broadening and corresponding transition rates of the lower (black squares) and upper (red circles) branches of the X^0 anticrossing for 7 CQDs at 20 K as obtained from fitting to Eq. (5.29), compared with numerical simulations (solid lines) of perfectly aligned QDs at a fixed interdot barrier width of 4 nm. Shaded regions show simulations for a range of coupling parameters matching observations.

The effect of energy splitting between exciton branches on the phonon-induced linewidth broadening for 7 CQDs is shown in Fig. 5.9. The value of phonon broadening $\Gamma_{1/2}^{ph}$ for each branch is obtained by fitting the bias-dependent linewidth to Eq. 5.29 to remove the effects of Gaussian broadening due to charge fluctuations and spectrometer resolution. The results are compared with numerical simulations of perfectly aligned QDs with an interdot barrier width of 4 nm, predicting a maximum broadening of 100 μeV at 0.9 meV for the upper branch and 60 μeV at 0.8 meV for the lower branch. This corresponds to a maximum transition rate of 150 ns^{-1} (90 ns^{-1}) for phonon emission (absorption). The experimental data appears to follow the simulated curve with variations of up to $\pm 28\%$ from predictions using average phonon coupling strength.

Near the ground state hole tunneling resonance of the neutral exciton state, the spatially direct and indirect excitons expressed in the localized basis as $|X\rangle = |e_B\rangle\,|h_B\rangle$ and $|iX\rangle = |e_B\rangle\,|h_T\rangle$, respectively, are coupled to form new eigenstates

$$\begin{aligned} |1\rangle &= a_{11}\,|X\rangle + a_{12}\,|iX\rangle \\ |2\rangle &= a_{21}\,|X\rangle + a_{22}\,|iX\rangle\,. \end{aligned} \tag{5.22}$$

The coefficients a_{ij} are found by diagonalizing the Hamiltonian matrix

$$H_X = \begin{pmatrix} E_X(U) & -t_h \\ -t_h & E_{iX}(U) \end{pmatrix}, \tag{5.23}$$

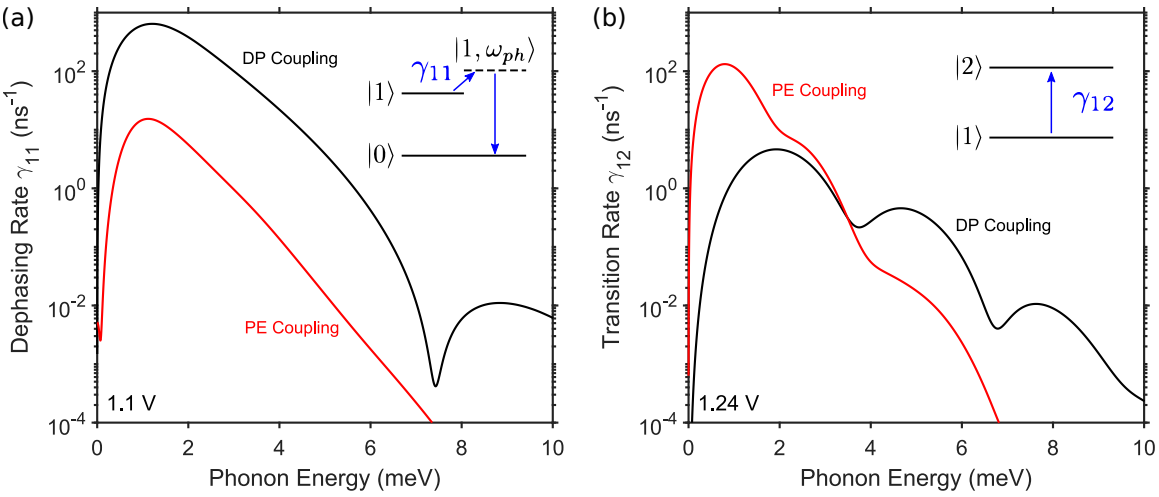

Figure 5.10: (a) Simulated dephasing rate away from the anticrossing and (b) transition rate at the center of the anticrossing, with contributions from deformation potential and piezoelectric coupling. Insets depict the relevant dephasing or transition process.

where t_h is the hole tunnel coupling energy and $E_{X(iX)}(U)$ is the experimentally determined energy of state $|X\rangle$ ($|iX\rangle$) as a function of bias voltage U applied to the diode. The eigenstate energies

$$E_{1/2} = \frac{E_X(U) + E_{iX}(U)}{2} \mp \sqrt{\left(\frac{E_X(U) - E_{iX}(U)}{2}\right)^2 + t_h^2} \tag{5.24}$$

form an avoided crossing, or anticrossing, with the minimum energy difference at resonance given by $\Delta E_{\min} = 2t_h$. Using the linear approximation of Stark shift near an anticrossing centered at U_{AC}, the eigenstate energies are given by $E_X(U) = E_0$ and $E_{iX}(U) = E_0 - p(U - U_{AC})$, leading to the bias-dependent slopes

$$\frac{\partial E_{1/2}}{\partial U} = -\frac{p}{2}\left(1 \pm \frac{U - U_{AC}}{\sqrt{(2t_h/p)^2 + (U - U_{AC})^2}}\right) \tag{5.25}$$

for each eigenstate.

The single-particle phonon coupling Hamiltonian given by Eq. (5.10) can be transformed to the diagonalized exciton basis as

$$H_{X-ph} = \sum_{nm}\sum_{s,\vec{q}} F^X_{s,nm}(\vec{q})\,|n\rangle\langle m|\,(b_{s,\vec{q}} + b^\dagger_{s,-\vec{q}}), \tag{5.26}$$

where the exciton-phonon coupling constants $F^X_{s,nm}$ are obtained by projecting Eq. (5.10) onto the diagonalized eigenstates. Transitions between states $|1\rangle$ and $|2\rangle$ necessarily involve hole tunneling, such that electron-phonon coupling does not contribute. Pure dephasing processes $|n\rangle \to |n\rangle$ with no population transfer, describing

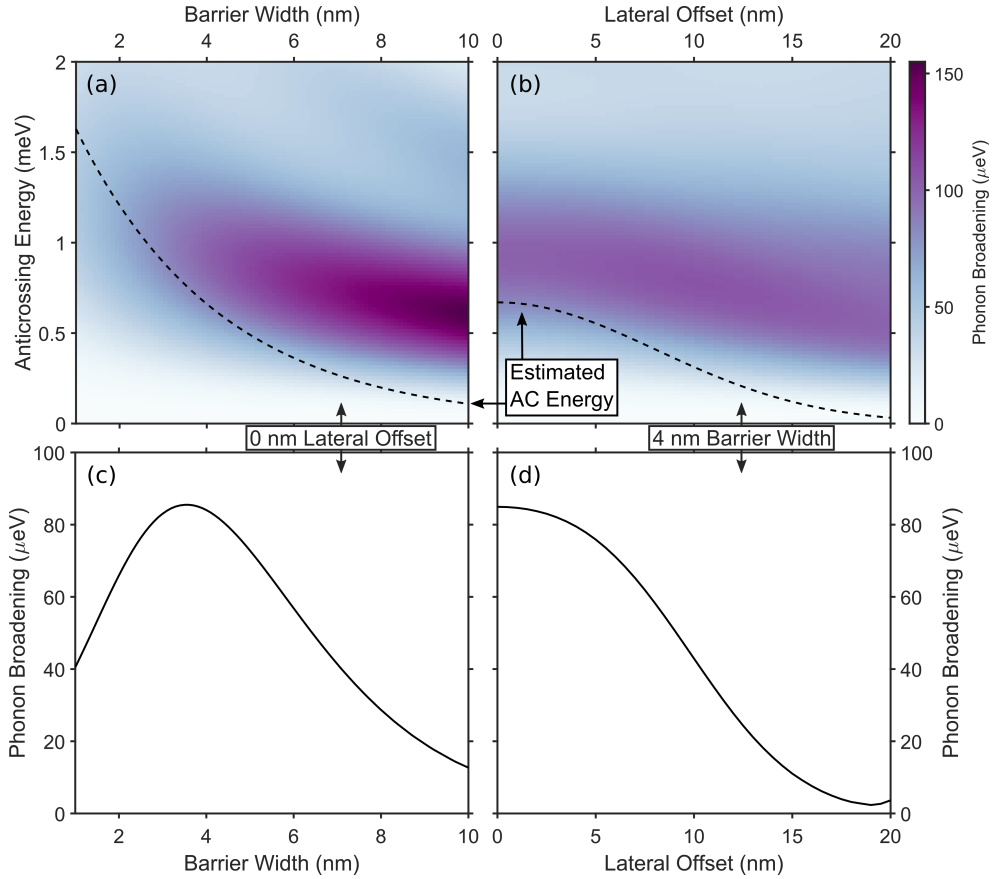

Figure 5.11: Simulated upper branch phonon broadening at 20 K, as a function of anticrossing energy and (a) interdot barrier width and (b) lateral offset between QD centers. Dashed lines in the upper plots show anticrossing energy values expected from previous experimental observations,[1] while lower plots show simulated phonon broadening for these expected anticrossing energies as a function of (c) barrier width and (d) lateral offset.

phonon-assisted optical transitions, can occur by electron- or hole-phonon coupling. Taking these properties into account, the exciton-phonon coupling constants are given in terms of the localized single-particle coupling constants as

$$\begin{aligned} F^X_{s,11} =& F^e_{s,BB} - a^2_{11}F^h_{s,BB} - a^2_{12}F^h_{s,TT} - 2a_{11}a_{12}F^h_{s,BT} \\ F^X_{s,22} =& F^e_{s,BB} - a^2_{21}F^h_{s,BB} - a^2_{22}F^h_{s,TT} - 2a_{21}a_{22}F^h_{s,BT} \\ F^X_{s,12} =& -a_{11}a_{21}F^h_{s,BB} - a_{12}a_{22}F^h_{s,TT} \\ & -(a_{11}a_{22}+a_{12}a_{21})F^h_{s,BT}. \end{aligned} \tag{5.27}$$

For numerical simulations, each integral is converted to a sum over a grid of values with a sufficient number of grid points to achieve satisfactory convergence. Since the system is assumed to have cylindrical symmetry, single-particle localized ground state wavefunctions are calculated using Eq. (2.23) and represented in cylin-

drical coordinates $\vec{r} = (r, \phi, z)$ as a product of r- and z-dependent components $\psi^{\alpha}_{B/T}(\vec{r}) = R^{\alpha}_0(r)Z^{\alpha}_1(z \mp d/2)$. Both r and z values are represented as 100-point grids, covering 30 nm in the r direction and 20 nm in the z direction. For simulations varying lateral offset between QDs (Fig. 5.11b and 5.11d), wavefunctions are represented in Cartesian coordinates with a 25-point grid in each dimension since cylindrical symmetry is broken. Due to the delta function in Eq. (5.19) which enforces energy conservation, it is most convenient to express phonon wavevectors in terms of energy in spherical coordinates $\vec{q}_s = (E/\hbar c_s, \phi, \theta)$. Both angular coordinates are represented as 200-point grids covering a full 4π solid angle, with the azimuthal coordinate ϕ from 0 to 2π and the polar coordinate θ from 0 to π. Form factors are calculated from the envelope wavefunctions using Eq. (5.17), with the transformations $q_r = q \sin\theta$ and $q_z = q \cos\theta$ to express the phonon wavevector in cylindrical coordinates. Due to the cylindrical symmetry, the directional dependence of piezoelectric phonon coupling $M_s(\hat{q})$ is averaged over the azimuthal coordinate as $\bar{M}_s(\theta) = \left(\int_0^{2\pi} M_s(\phi, \theta)^2 \, d\phi/2\pi \right)^{1/2}$ to obtain

$$\begin{aligned} \bar{M}_{LA}(\theta) &= \sqrt{\frac{9}{8}} \sin(2\theta) \sin\theta \\ \bar{M}_{TA_1}(\theta) &= \frac{1}{\sqrt{2}} \sin(2\theta) \\ \bar{M}_{TA_2}(\theta) &= \frac{1}{\sqrt{2}} \sin\theta (3\cos^2\theta - 1). \end{aligned} \tag{5.28}$$

Finally, single-particle coupling constants $F^{\alpha}_{s,ij}(\vec{q})$, calculated using the obtained form factors and bulk coupling constants given by Eqs. (5.12) and (5.13), are represented for each particle $\alpha = \{e, h\}$ and set of QD locations $\{i, j\} = \{B, T\}$ as a function of phonon mode s, phonon energy E, and polar angle θ.

At each value of the bias voltage U, the tunneling Hamiltonian given by Eq. (5.23) is diagonalized to obtain the eigenstate coefficients a_{ij}. These are used to obtain the phonon coupling constants F^X_{nm} and optical dipole matrix elements M_n in the eigenstate basis. The phonon spectral density can then be calculated using Eq. (5.20), allowing calculation of the optical transition rates and absorption and emission spectra using Eq. (2.50). As a final step, Gaussian convolutions are applied to the optical transition spectra in the energy and bias directions to reproduce broadening due to the spectrometer response and local charge fluctuations, respectively. The values of material and structural parameters used in the simulations are listed in Table B.1, except where otherwise noted.

The non-monotonic bias dependence of linewidth in Fig. 5.7a, together with the additional temperature-dependent broadening in Fig. 5.8, indicate a significant enhancement of phonon-assisted transition rates between eigenstates at tunneling resonances. The bias-dependent ZPL linewidth can be fit to the predicted form of Gaussian broadening in Eq. 2.53 with an additional phonon-induced broadening with

a Lorentzian shape, resulting in the function

$$\Gamma_{1/2}(U) = \sqrt{\left(\frac{p\Delta U_{fluct}}{2}\right)^2 \left(1 \pm \frac{U - U_{AC}}{\sqrt{(2t_h/p)^2 + (U - U_{AC})^2}}\right)^2 + (\Gamma_{spect})^2} + \frac{\Gamma_{1/2}^{ph}}{1 + \left(\frac{U - U_{AC}}{2t_h/p}\right)^2} \tag{5.29}$$

for each branch, with fit parameters U_{AC}, t_h, and p describing the position and shape of the anticrossing energy levels and ΔU_{fluct}, Γ_{spect}, and $\Gamma_{1/2}^{ph}$ describing the strength of broadening due to charge fluctuations, spectrometer resolution, and phonon-assisted transitions, respectively.

The theory predicts an asymmetry in peak linewidths of the upper and lower branches, with the upper branch being more broad due to a faster phonon emission process compared to phonon absorption, resulting in a shorter lifetime for state $|2\rangle$. Fits to observed spectra appear to show an additional broadening of the lower branch just past the center of the anticrossing, to a level higher than the peak linewidth of the upper branch. However, the region with increased fit linewidth of the lower branch corresponds to where a second faintly visible peak merges with it. This peak appears to be due to a weakly-allowed recombination from the dark exciton spin state due to spin-orbit coupling, with an exchange splitting of 225 ± 14 μeV far from the anticrossing.[66, 40]

Fig. 5.10 shows the calculated phonon-assisted transition and pure dephasing rates at the anticrossing for each coupling mechanism at 20 K, as a function of phonon energy. Transitions between eigenstates are dominated by piezoelectric coupling at low energies, with a maximum at 0.8 meV for phonon absorption from the lower branch. The linewidth broadening effect is therefore predicted to be strongest for CQDs with an anticrossing splitting energy of $0.8 - 0.9$ meV. The sideband-producing pure dephasing process is dominated by deformation potential coupling, with a maximum at 1.2 meV. The experimental spectra should therefore give a measure of piezoelectric coupling strength through the ZPL linewidth at the anticrossing and deformation potential coupling through the intensity and distribution of acoustic phonon sidebands, which are more prominent away from the anticrossing where the ZPL is narrower. The oscillatory decay of transition and dephasing rates as a function of phonon energy is a known feature of CQDs, arising from resonances in the phonon coupling form factor (Eq. 5.11) between phonon wavelength and QD separation.[112, 123] The phonon coupling strength $F_{s,12}^X(\vec{q})$, primarily due to the piezoelectric interaction, was initially too high when calculated using the material parameters for GaAs listed in Table B.1. This was reduced to match observed peak anticrossing linewidths by using effective $In_xGa_{1-x}As$ composition values of $x = 32 \pm 12\%$ when calculating phonon coupling constants, with material parameters varying linearly between GaAs ($x = 0$) and InAs ($x = 1$). The deformation potential parameters a_c and a_v were both increased by a factor between 1.27 and 2.22 relative to the values listed in Table B.1

to match observed sideband intensities between 0.6% and 1.4% of ZPL intensity, since literature values of these parameters are highly inconsistent. The coupling strength could also be modified more weakly through the form factor $\mathcal{F}_{ij}^{\alpha}(\vec{q})$ by changing the QD charge confinement and single-particle wavefunctions.

The variations in phonon coupling strength can potentially be explained by differences in CQD geometry throughout the sample, with simulated dependence on interdot barrier width and lateral misalignment shown in Fig. 5.11. While the interdot barrier width is expected to be quite uniform throughout each sample, variances in CQD alignment have been observed and could significantly reduce the phonon coupling depending on the lateral confinement within each QD.[40] Since the value of tunnel coupling and anticrossing energy is proportional to wavefunction overlap between localized states, we calibrate the value of anticrossing energy expected in each case using previous measurements on a series of CQD samples grown similarly with different interdot barrier widths to obtain the curves in the lower plots.[1] The simulations predict maximum phonon broadening for interdot barrier widths near 4 nm, and a decrease in phonon broadening with lateral QD misalignment.

While the data and simulations presented in this report focus on the hole tunneling resonance of the neutral exciton state, we expect that the enhancement of phonon coupling at tunneling resonances is a more general effect which can apply to different charge states as well. The geometric phonon coupling form factor is increased by the formation of delocalized eigenstates, which occurs at any tunneling resonance regardless of the configuration of resident charges. The bulk PE coupling constant (Eq. 5.13) is equal for electrons and holes, so the effect can occur regardless of which charge carrier is tunneling. The only remaining requirement for strong phonon coupling enhancement is that the AC splitting energy lies near the maximum of the phonon spectral density for PE coupling, a condition which depends on the size and confinement potential of the QDs. Electron tunneling ACs typically have a much larger energy splitting due to their lower effective mass, inhibiting this effect since PE coupling is strongly weighted towards lower phonon energies.[1] Initial observations indicate a similar level of phonon broadening at hole tunneling resonances in positive trion and neutral biexciton transitions, though the presence of additional optically active spin states makes the fitting procedure more complicated and the results less reliable.

To conclude, we have measured the linewidths of direct exciton, indirect exciton and tunneling resonance states for CQDs. We have confirmed that pure dephasing, phonon relaxation and charge fluctuations in the CQDs lead to linewidth broadening. The existence of phonon transitions between the molecular-like excitons in the system cause the linewidth to broaden beyond the charge fluctuation-induced broadening of the indirect exciton state. The transition of linewidths from direct to indirect exciton state is non-monotonic near tunneling resonances and phonon-induced broadening up to 100 μeV is reported at 20 K, corresponding to phonon-assisted transition rates up to 150 ns^{-1}. These measurements are in good agreement with theoretical calculations of linewidth broadening at tunneling resonances including phonon-assisted transitions due to PE and DP coupling.

Chapter 6

Conclusion

In this dissertation, we have developed a theoretical model of electron and hole confinement in CQDs, including Coulomb and spin interactions, phonon coupling, and optical transitions. Simulations of relaxation dynamics during neutral molecular biexciton cascades indicate that polarization-entangled photon pairs can be generated with a high degree of entanglement fidelity. While this process has been demonstrated in single QDs, we find that charge separation in interdot states of CQDs allows for tunable emission energies and a higher tolerance to anisotropic electron-hole exchange splitting.

Using low-temperature optical PL spectrosopy, we identify charge and spin states in single CQDs and investigate their interactions. Two-laser PLE spectroscopy demonstrates two-photon excitation into the molecular biexciton state via a stepwise process, while calculations identify conditions required for efficient simultaneous two-photon absorption. Further investigations find decoherence by electric field fluctuations from charged lattice defects, and identify a novel enhancement of acoustic phonon coupling at hole tunneling resonances from piezoelectric interactions.

The theoretical model could be enhanced by the inclusion of coupling between valence bands within the multiband $\vec{k} \cdot \vec{p}$ model, as described in Chapter 2. Hole spin states could then by described as a spinor with a small but significant light-hole component, allowing for a consistent description of phonon-assisted spin-flip transitions rather than relying on fits to reported experimental observations. In addition, a full three-dimensional model of CQD confinement including strain relaxation, piezoelectric polarization, and random alloy fluctuations would improve the accuracy of wavefunction and tunnel coupling calculations. Finally, the Markov approximation neglecting re-absorption of emitted photons and phonons, implicit in the derivation of the Lindblad equation used in Chapter 4, can be relaxed by employing one of several methods for calculating non-Markovian dynamics of open quantum systems [138].

Experimentally, collection of photons from the neutral biexciton cascade under resonant two-photon excitation would be enabled by enhanced suppression of scattered laser light. This could be achieved using confocal fiber-coupled excitation and collection with triple-subtractive detection, with further improvement possible by guiding the excitation light through an in-plane optical waveguide coupled to the

CQD. Biexciton cascade emission could be measured by time-correlated single photon counting (TCSPC) with a pair of avalanche photodiode detectors, while full control over detected polarization states would allow quantum state tomography to determine the two-photon polarization state and monitor entanglement. TCSPC would also enable an investigation of charge fluctuation dynamics in combination with spectral filtering [139] or laser frequency scanning [133].

The enhanced acoustic phonon coupling effect observed at hole tunneling resonances also invites further study; initial experiments could unambiguously measure resonant phonon broadening in only one CQD sample with a 4 nm interdot tunneling barrier, limiting the range of observed anticrossing energy splitting values. While measurements of other CQD samples also showed indications of resonant phonon broadening, the lower intensity of interdot transitions combined with a higher level of charge fluctuation broadening resulted in difficulties obtaining consistent linewidth fits and isolating the phonon-induced component of broadening. Further experiments could reduce charge fluctuation broadening by modifying sample structures to increase the distance between the CQD and defect-prone material interfaces, allowing accurate investigations of phonon coupling in samples with different tunneling barrier thickness and anticrossing energy splitting to verify the model calculations. The effect might also be seen at electron tunneling resonances if the anticrossing splitting energy can be sufficiently reduced to the ~ 1 meV range where piezoelectric coupling is maximized, possibly by the inclusion of $Al_xGa_{1-x}As$ or another higher-bandgap material in the interdot barrier. Additionally, the resonant acoustic phonon coupling enhancement has the potential to increase strain sensing and actuation capabilities for CQDs embedded in micro-mechanical resonator structures [11].

To conclude, this dissertation describes a model of coherent spin interactions and relaxation processes in CQDs, allowing an understanding of their behavior and potential usage in quantum information and sensing technologies. While the model has room for improvement in several key areas, it captures the essential properties to allow a simulation of spin dynamics and entangled photon emission. Experimental PL and PLE spectroscopy reveals decoherence mechanisms which are important to understand and avoid for development of CQD-based quantum technologies, including pure dephasing by charge fluctuations and phonon-assisted tunneling. Finally, an enhancement of acoustic phonon coupling between delocalized charge states at hole tunneling resonances was observed, indicating a novel piezoelectric coupling mechanism which might occur more generally in other systems with a delocalized charge distribution.

Appendix A

CQD Charge States

q	n_X	Charge State	$\left(\begin{smallmatrix} e_B & e_T \\ h_B & h_T \end{smallmatrix}\right)$	Spin States	J_z
0	0	g	$\left(\begin{smallmatrix} 0 & 0 \\ 0 & 0 \end{smallmatrix}\right)$	$\|0\rangle$	0
	1	X^0	$\left(\begin{smallmatrix} 1 & 0 \\ 1 & 0 \end{smallmatrix}\right)$	$\|\downarrow\Uparrow\rangle, \|\uparrow\Downarrow\rangle$	±1
				$\|\uparrow\Uparrow\rangle, \|\downarrow\Downarrow\rangle$	±2
		iX^0	$\left(\begin{smallmatrix} 1 & 0 \\ 0 & 1 \end{smallmatrix}\right)$	$\|\downarrow\Uparrow\rangle, \|\uparrow\Downarrow\rangle$	±1
				$\|\uparrow\Uparrow\rangle, \|\downarrow\Downarrow\rangle$	±2
	2	XX^0	$\left(\begin{smallmatrix} 2 & 0 \\ 2 & 0 \end{smallmatrix}\right)$	$\|\uparrow\downarrow_S\Uparrow\Downarrow_S\rangle$	0
		iXX^0	$\left(\begin{smallmatrix} 2 & 0 \\ 1 & 1 \end{smallmatrix}\right)$	$\|\uparrow\downarrow_S\Uparrow\Downarrow_S\rangle, \|\uparrow\downarrow_S\Uparrow\Downarrow_T\rangle$	0
				$\|\uparrow\downarrow_S\Uparrow\Uparrow_T\rangle, \|\uparrow\downarrow_S\Downarrow\Downarrow_T\rangle$	±3
		$iXiX^0$	$\left(\begin{smallmatrix} 2 & 0 \\ 0 & 2 \end{smallmatrix}\right)$	$\|\uparrow\downarrow_S\Uparrow\Downarrow_S\rangle$	0
+1	0	h_B^+	$\left(\begin{smallmatrix} 0 & 0 \\ 1 & 0 \end{smallmatrix}\right)$	$\|\Uparrow\rangle, \|\Downarrow\rangle$	$\pm3/2$
		h_T^+	$\left(\begin{smallmatrix} 0 & 0 \\ 0 & 1 \end{smallmatrix}\right)$	$\|\Uparrow\rangle, \|\Downarrow\rangle$	$\pm3/2$
	1	X^+	$\left(\begin{smallmatrix} 1 & 0 \\ 2 & 0 \end{smallmatrix}\right)$	$\|\uparrow\Uparrow\Downarrow_S\rangle, \|\downarrow\Uparrow\Downarrow_S\rangle$	$\pm1/2$
		iX^+	$\left(\begin{smallmatrix} 1 & 0 \\ 1 & 1 \end{smallmatrix}\right)$	$\|\uparrow\Uparrow\Downarrow_S\rangle, \|\downarrow\Uparrow\Downarrow_S\rangle$	$\pm1/2$
				$\|\uparrow\Uparrow\Downarrow_T\rangle, \|\downarrow\Uparrow\Downarrow_T\rangle$	$\pm1/2$
				$\|\downarrow\Uparrow\Uparrow_T\rangle, \|\uparrow\Downarrow\Downarrow_T\rangle$	$\pm5/2$
				$\|\uparrow\Uparrow\Uparrow_T\rangle, \|\downarrow\Downarrow\Downarrow_T\rangle$	$\pm7/2$
		iiX^+	$\left(\begin{smallmatrix} 1 & 0 \\ 0 & 2 \end{smallmatrix}\right)$	$\|\uparrow\Uparrow\Downarrow_S\rangle, \|\downarrow\Uparrow\Downarrow_S\rangle$	$\pm1/2$
	2	XX^+	$\left(\begin{smallmatrix} 2 & 0 \\ 3 & 0 \end{smallmatrix}\right)$	$\|\uparrow\downarrow_S\Uparrow\Downarrow_S\Uparrow\rangle, \|\uparrow\downarrow_S\Uparrow\Downarrow_S\Downarrow\rangle$	$\pm3/2$
		iXX^+	$\left(\begin{smallmatrix} 2 & 0 \\ 2 & 1 \end{smallmatrix}\right)$	$\|\uparrow\downarrow_S\Uparrow\Downarrow_S\Uparrow\rangle, \|\uparrow\downarrow_S\Uparrow\Downarrow_S\Downarrow\rangle$	$\pm3/2$
		$iXiX^+$	$\left(\begin{smallmatrix} 2 & 0 \\ 1 & 2 \end{smallmatrix}\right)$	$\|\uparrow\downarrow_S\Uparrow\Downarrow_S\Uparrow\rangle, \|\uparrow\downarrow_S\Uparrow\Downarrow_S\Downarrow\rangle$	$\pm3/2$
		$iiXiX^+$	$\left(\begin{smallmatrix} 2 & 0 \\ 0 & 3 \end{smallmatrix}\right)$	$\|\uparrow\downarrow_S\Uparrow\Downarrow_S\Uparrow\rangle, \|\uparrow\downarrow_S\Uparrow\Downarrow_S\Downarrow\rangle$	$\pm3/2$
-1	0	e^-	$\left(\begin{smallmatrix} 1 & 0 \\ 0 & 0 \end{smallmatrix}\right)$	$\|\uparrow\rangle, \|\downarrow\rangle$	$\pm1/2$
	1	X^-	$\left(\begin{smallmatrix} 2 & 0 \\ 1 & 0 \end{smallmatrix}\right)$	$\|\uparrow\downarrow_S\Uparrow\rangle, \|\uparrow\downarrow_S\Downarrow\rangle$	$\pm3/2$
		iX^-	$\left(\begin{smallmatrix} 2 & 0 \\ 0 & 1 \end{smallmatrix}\right)$	$\|\uparrow\downarrow_S\Uparrow\rangle, \|\uparrow\downarrow_S\Downarrow\rangle$	$\pm3/2$
	2	XX^-	$\left(\begin{smallmatrix} 3 & 0 \\ 2 & 0 \end{smallmatrix}\right)$	$\|\uparrow\downarrow_S\uparrow\Uparrow\Downarrow_S\rangle, \|\uparrow\downarrow_S\downarrow\Uparrow\Downarrow_S\rangle$	$\pm1/2$
		iXX^-	$\left(\begin{smallmatrix} 3 & 0 \\ 1 & 1 \end{smallmatrix}\right)$	$\|\uparrow\downarrow_S\uparrow\Uparrow\Downarrow_S\rangle, \|\uparrow\downarrow_S\downarrow\Uparrow\Downarrow_S\rangle$	$\pm1/2$
				$\|\uparrow\downarrow_S\uparrow\Uparrow\Downarrow_T\rangle, \|\uparrow\downarrow_S\downarrow\Uparrow\Downarrow_T\rangle$	$\pm1/2$
				$\|\uparrow\downarrow_S\downarrow\Uparrow\Uparrow_T\rangle, \|\uparrow\downarrow_S\uparrow\Downarrow\Downarrow_T\rangle$	$\pm5/2$
				$\|\uparrow\downarrow_S\uparrow\Uparrow\Uparrow_T\rangle, \|\uparrow\downarrow_S\downarrow\Downarrow\Downarrow_T\rangle$	$\pm7/2$
		$iXiX^-$	$\left(\begin{smallmatrix} 3 & 0 \\ 0 & 2 \end{smallmatrix}\right)$	$\|\uparrow\downarrow_S\uparrow\Uparrow\Downarrow_S\rangle, \|\uparrow\downarrow_S\downarrow\Uparrow\Downarrow_S\rangle$	$\pm1/2$

Table A.1: List of all possible CQD charge and spin states with total charge $q = 0, \pm1$ and number of excitons $n_X \leq 2$, limited to ground-state orbitals (except when filled) and hole tunneling only (electrons fixed in lower-energy bottom QD).

Appendix B

Simulation Parameters

		GaAs	InAs
Material Parameters			
Electron effective mass (m_0) [140]	m_e	0.059	0.042
Hole effective mass (m_0) [140]	m_h	0.37	0.34
Conduction band edge (eV) [140]	E_c	1.518	1.057
Valence band edge (eV) [140]	E_v	0	0.192
CB deformation potential (eV) [112]	a_c	-9.3	
VB deformation potential (eV) [112]	a_v	-0.7	
Piezoelectric constant (C/m^2) [112]	d_P	0.16	0.045
Relative dielectric constant [112]	ϵ_r	12.9	15.15
Crystal density (kg/m^3) [112]	ρ	5300	5670
LA phonon velocity (m/s) [112]	c_{LA}	5150	
TA phonon velocity (m/s) [112]	c_{TA}	2800	
Quantum Dot Parameters			
Bottom QD height (nm) [30]	h_B	2.9	
Top QD height (nm) [30]	h_T	2.1	
QD center separation (nm)	d	6.5	
e^- excited state spacing (meV)	$\hbar\omega_e$	100	
h^+ excited state spacing (meV) [30]	$\hbar\omega_h$	21.2	
h^+ tunnel coupling (μeV)	t_h	330.5	
Exciton intensity ratio	I_X/I_{iX}	17.09	
Bias fluctuation width (mV)	ΔU_{fluct}	3.58	
Experiment Parameters			
Temperature (K)	T	20	
Spectrometer resolution (μeV)	Γ_{spect}	37.0	

Table B.1: Numerical values of physical parameters used in all simulations, except where otherwise noted. Values are taken from references where specified.

Bibliography

[1] A. Bracker, M. Scheibner, M. Doty, E. Stinaff, I. Ponomarev, J. Kim, L. Whitnam, T. Reinecke, and D. Gammon. *Appl. Phys. Lett.*, 89:233110, 2006.

[2] J. Orton and T. Foxon. *Molecular Beam Epitaxy*. Oxford University Press, Oxford, UK, 2015.

[3] J. Wu, S. Chen, A. Seeds, and H. Liu. *J. Phys. D: Appl. Phys.*, 48:363001, 2015.

[4] H. Asahi and Y. Horikoshi. *Molecular Beam Epitaxy*. John Wiley & Sons, Hoboken, NJ, 2019.

[5] S. Chen, W. Li, J. Wu, Q. Jiang, M. Tang, S. Shutts, S. N. Elliott, A. Sobiesierski, A. J. Seeds, I. Ross, P. M. Smowton, and H. Liu. *Nat. Photonics*, 10:307, 2016.

[6] A. Becker, V. Sichkovskyi, M. Bjelica, A. Rippien, F. Schnabel, M. Kaiser, O. Eyal, B. Witzigmann, G. Eisenstein, and J. P. Reithmaier. *Appl. Phys. Lett.*, 110:181103, 2017.

[7] D. Bimberg. *Semiconductor Nanostructures*. Springer, Berlin, Germany, 2008.

[8] A. Marent, T. Nowozin, M. Geller, and D. Bimberg. *Semicond. Sci. Technol.*, 26:014026, 2011.

[9] D. Cadeddu, M. Munsch, N. Rossi, J.-M. Gérard, J. Claudon, R. J. Warburton, and M. Poggio. *Phys. Rev. Appl.*, 8:031002, 2017.

[10] P.-L. de Assis, I. Yeo, A. Gloppe, H. A. Nguyen, D. Tumanov, E. Dupont-Ferrier, N. S. Malik, E. Dupuy, J. Claudon, J.-M. Gérard, A. Auffèves, O. Arcizet, M. Richard, and J.-Ph. Poizat. *Phys. Rev. Lett.*, 118:117401, 2017.

[11] S. G. Carter, A. S. Bracker, M. K. Yakes, M. K. Zalalutdinov, M. Kim, C. S. Kim, C. Czarnocki, M. Scheibner, and D. Gammon. *Appl. Phys. Lett.*, 111:183101, 2017.

[12] D. Loss and D. P. DiVincenze. *Phys. Rev. A*, 57:120, 1998.

[13] M. A. Nielsen and I. L. Chuang. *Quantum Computation and Quantum Information*. Cambridge University Press, Cambridge, UK, 2000.

[14] P. Michler. *Single Semiconductor Quantum Dots*. Springer, Berlin, Germany, 2009.

[15] P. Michler. *Quantum Dots for Quantum Information Technologies*. Springer, Berlin, Germany, 2017.

[16] P. Senellart, G. Solomon, and A. White. *Nat. Nanotechnol.*, 12:1026, 2017.

[17] S. Deshpande, T. Frost, A. Hazari, and P. Bhattacharya. *Appl. Phys. Lett.*, 105:141109, 2014.

[18] R. Winik, D. Cogan, Y. Don, I. Schwartz, L. Gantz, E. R. Schmidgall, N. Livneh, R. Rapaport, E. Buks, and D. Gershoni. *Phys. Rev. B*, 95:235435, 2017.

[19] T. Müller, J. Skiba-Szymanska, A. B. Krysa, J. Huwer, M. Felle, M. Anderson, R. M. Stevenson, J. Heffernan, D. A. Ritchie, and A. J. Shields. *Nat. Commun.*, 9:862, 2018.

[20] J. Liu, R. Su, Y. Wei, B. Yao, S. F. C. da Silva, Y. Yu, J. Iles-Smith, K. Srinivasan, A. Rastelli, J. Li, and X. Wang. *Nat. Nanotechnol.*, 14:586, 2019.

[21] C. Jennings, X. Ma, T. Wickramasinghe, M. Doty, M. Scheibner, E. Stinaff, and M. Ware. *Adv. Quantum Tech.*, 3:1900085, 2019.

[22] D. Kim, S. G. Carter, A. Greilich, A. S. Bracker, and D. Gammon. *Nat. Phys.*, 7:223, 2011.

[23] S. E. Economou, N. Lindner, and T. Rudolph. *Phys. Rev. Lett.*, 105:093601, 2010.

[24] M. Gimeno-Segovia, T. Rudolph, and S. E. Economou. *Phys. Rev. Lett.*, 123:070501, 2019.

[25] C. Jennings and M. Scheibner. *Phys. Rev. B*, 93:115311, 2016.

[26] P. Kumar, C. Jennings, M. Scheibner, A. S. Bracker, S. G. Carter, and D. Gammon. Spectral broadening of optical transitions at tunneling resonances in InAs/GaAs coupled quantum dot pairs. Submitted for publication, 2020.

[27] K. Jacobi. *Prog. Surf. Sci.*, 71:185, 2003.

[28] D. Leonard, K. Pond, and P. M. Petroff. *Phys. Rev. B*, 50:11687, 1994.

[29] Z. R. Wasilewski, S. Fafard, and J. P. McCaffrey. *J. Cryst. Growth*, 201-202:1131, 1999.

[30] M. Scheibner, M. Yakes, A. Bracker, I. Ponomarev, M. Doty, C. Hellberg, L. Whitman, T. Reinecke, and D. Gammon. *Nat. Phys.*, 4:291, 2008.

[31] N. Liu, J. Tersoff, O. Baklenov, Jr. Holmes, A. L., and C. K. Shih. *Phys. Rev. Lett.*, 84:334, 2000.

[32] M. A. Migliorato, A. G. Cullis, M. Fearn, and J. H. Jefferson. *Phys. Rev. B*, 65:115316, 2002.

[33] A. Lenz, R. Timm, H. Eisele, Ch. Hennig, S. K. Becker, R. L. Sellin, U. W. Pohl, D. Bimberg, and M. Dähne. *Appl. Phys. Lett.*, 81:5150, 2002.

[34] V. Jovanov, T. Eissfeller, S. Kapfinger, E. C. Clark, F. Klotz, M. Bichler, J. G. Keizer, P. M. Koenraad, M. S. Brandt, G. Abstreiter, and J. J. Finley. *Phys. Rev. B*, 85:165433, 2012.

[35] P.-L. Ardelt, K. Gawarecki, K. Müller, A. M. Waeber, A. Bechtold, K. Oberhofer, J. M. Daniels, F. Klotz, M. Bichler, T. Kuhn, H. J. Krenner, P. Machnikowski, and J. J. Finley. *Phys. Rev. Lett.*, 116:077401, 2016.

[36] G. S. Solomon, J. A. Trezza, A. F. Marshall, and Jr. Harris, J. S. *Phys. Rev. Lett.*, 76:952, 1996.

[37] N. N. Ledentsov, V. A. Shchukin, M. Grundmann, N. Kirstaedter, J. Böhrer, O. Schmidt, D. Bimberg, V. M. Ustinov, A. Yu. Egorov, A. E. Zhukov, P. S. Kop'ev, S. V. Zaitsev, N. Yu. Gordeev, Zh. I. Alferov, A. I. Borovkov, A. O. Kosogov, S. S. Ruvimov, P. Werner, U. Gösele, and J. Heydenreich. *Phys. Rev. B*, 54:8743, 1996.

[38] W. Wu, J. R. Tucker, G. S. Solomon, and Jr. Harris, J. S. *Appl. Phys. Lett.*, 71:1083, 1997.

[39] H. Eisele, O. Flebbe, T. Kalka, C. Preinesberge, F. Heinrichsdorff, A. Krost, D. Bimberg, and M. Dähne-Prietsch. *Appl. Phys. Lett.*, 75:106, 1999.

[40] M. F. Doty, J. I. Climente, A. Greilich, M. Yakes, A. S. Bracker, and D. Gammon. *Phys. Rev. B*, 81:035308, 2010.

[41] M. Grundmann, O. Stier, and D. Bimberg. *Phys. Rev. B*, 52:11969, 1995.

[42] C. Pryor, J. Kim, L. W. Wang, A. J. Williamson, and A. Zunger. *J. Appl. Phys.*, 83:2548, 1998.

[43] O. Stier, M. Grundmann, and D. Bimberg. *Phys. Rev. B*, 59:5688, 1999.

[44] G. Bester, X. Wu, D. Vanderbilt, and A. Zunger. *Phys. Rev. Lett.*, 96:187602, 2006.

[45] A. Schliwa, M. Winkelnkemper, and D. Bimberg. *Phys. Rev. B*, 76:205324, 2007.

[46] T. Saito, T. Nakaoka, and Y. Arakawa. *Phys. Rev. B*, 91:115306, 2015.

[47] C. Pryor. *Phys. Rev. B*, 57:7190, 1998.

[48] W. Sheng, S.-J. Cheng, and P. Hawrylak. *Phys. Rev. B*, 71:035316, 2005.

[49] D. J. BenDaniel and C. B. Duke. *Phys. Rev.*, 152:683, 1966.

[50] O. Stier and D. Bimberg. *Phys. Rev. B*, 55:7726, 1997.

[51] S. L. Chuang. *Physics of Optoelectronic Devices*. Wiley Interscience, New York, NY, 1995.

[52] J. Luttinger and W. Kohn. *Phys. Rev.*, 97:869, 1955.

[53] G. L. Bir and G. E. Pikus. *Symmetry and Strain-Induced Effects in Semiconductors*. John Wiley & Sons, New York, NY, 1974.

[54] J. Climente, M. Korkusinski, G. Goldoni, and P. Hawrylak. *Phys. Rev. B*, 78:115323, 2008.

[55] M. Korkusinski and P. Hawrylak. *Phys. Rev. B*, 63:195311, 2001.

[56] M. F. Doty, J. I. Climente, M. Korkusinski, M. Scheibner, A. S. Bracker, P. Hawrylak, and D. Gammon. *Phys. Rev. Lett.*, 102:047401, 2009.

[57] S. Ramanathan, G. Petersen, K. Wijesundara, R. Thota, E. Stinaff, M. Kerfoot, M. Scheibner, A. Bracker, and D. Gammon. *App. Phys. Lett.*, 102:213101, 2013.

[58] I. V. Ponomarev, M. Scheibner, E. A. Stinaff, A. S. Bracker, M. F. Doty, S. C. Badescu, M. E. Ware, V. L. Korenev, T. L. Reinecke, and D. Gammon. *Phys. Status Solidi B*, 243:3869, 2006.

[59] M. Scheibner, A. S. Bracker, D. Kim, and D. Gammon. *Solid State Commun.*, 149:1427, 2009.

[60] T. Takagahara. *Phys. Rev. B*, 62:16840, 2000.

[61] E. Poem, J. Shemesh, I. Marderfeld, D. Galushko, N. Akopian, D. Gershoni, B. Gerardot, A. Badolato, and P. Petroff. *Phys. Rev. B*, 76:235304, 2007.

[62] D. Gammon, Al. L. Efros, J. G. Tischler, A. S. Bracker, V. L. Korenev, and I. A. Merkulov. Electronic and nuclear spin in the optical spectra of semiconductor quantum dots. In T. Takagahara, editor, *Quantum Coherence, Correlation and Decoherence in Semiconductor Nanostructures*, chapter 6. Elsevier Science, New York, 2003.

[63] M. Scheibner, M. F. Doty, I. V. Ponomarev, A. S. Bracker, E. A. Stinaff, V. L. Korenev, T. L. Reinecke, and D. Gammon. *Phys. Rev. B*, 75:245318, 2007.

[64] M. O. Scully and M. S. Zubairy. *Quantum Optics*. Cambridge University Press, Cambridge, UK, 1997.

[65] G. Grynberg, A. Aspect, and C. Fabre. *Introduction to Quantum Optics*. Cambridge University Press, Cambridge, UK, 2010.

[66] J. Daniels, P. Machnikowski, and T. Kuhn. *Phys. Rev. B*, 88:205307, 2013.

[67] N. N. Ledentsov. *Growth Processes and Surface Phase Equilibria in Molecular Beam Epitaxy*. Springer, Berlin, Germany, 1999.

[68] M. Henini. *Molecular Beam Epitaxy: From research to mass production*. Elsevier, Oxford, UK, 2013.

[69] C. Czarnocki, M. L. Kerfoot, J. Casara, A. R. Jacobs, C. Jennings, and M. Scheibner. *J. Vis. Exp.*, 112:e53719, 2016.

[70] R. P. Feynman. *Int.J. Theor. Phys.*, 21:467, 1982.

[71] D. Deutsch. *Proc. R. Soc. Lond. A*, 400:97, 1985.

[72] E. Knill, R. Laflamme, and G. J. Millburn. *Nature*, 409:46, 2001.

[73] M. A. Nielsen. *Phys Rev. Lett.*, 93:040503, 2004.

[74] R. Prevedel, M. Aspelmeyer, C. Brukner, A. Zeilinger, and T. D. Jennewein. *J. Opt. Soc. Am. B*, 24:241, 2007.

[75] A. K. Ekert. *Phys. Rev. Lett.*, 67:661, 1991.

[76] C. H. Bennett, F. Bessette, G. Brassard, and L. Salvail. *J. Cryptology*, 5:3, 1992.

[77] Nicolas Gisin, Grégoire Ribordy, Wolfgang Tittel, and Hugo Zbinden. Quantum cryptography. *Rev. Mod. Phys.*, 74:145–195, Mar 2002.

[78] Z. D. Walton, A. F. Abouraddy, A. V. Sergienko, B. E. A. Saleh, and M. C. Teich. *Phys. Rev. A*, 67:062309, 2003.

[79] T. Ono, R. Okamoto, and S. Takeuchi. *Nat. Commun.*, 4:2426, 2013.

[80] Peter van Loock. Optical hybrid approaches to quantum information. *Laser Photonics Rev.*, 5:167–200, 2011.

[81] Pieter Kok, W. J. Munro, Kae Nemoto, T. C. Ralph, Jonathan P. Dowling, and G. J. Milburn. Linear optical quantum computing with photonic qubits. *Rev. Mod. Phys.*, 79:135–174, Jan 2007.

[82] S. E. Economou, J. I. Climente, A. Badolato, A. S. Bracker, D. Gammon, and M. F. Doty. *Phys. Rev. B*, 86:085319, 2012.

[83] Miloslav Dušek and Kamil Brádler. The effect of multi-pair signal states in quantum cryptography with entangled photons. *J. Opt. B: Quantum Semiclass. Opt.*, 4:109–113, 2002.

[84] K. De Greve, L. Yu, P. McMahon, J. Pelc, C. Natarajan, N. Kim, E. Abe, S. Maier, C. Schneider, M. Kamp, S. Höfling, R. Hadfield, A. Forchel, M. Fejer, and Y. Yamamoto. *Nature*, 491:421, 2012.

[85] W. Gao, P. Fallahi, E. Togan, J. Miguel-Sanchez, and A. Imamoglu. *Nature*, 491:426, 2012.

[86] M. Bayer, G. Ortner, O. Stern, A. Kuther, A. Gorbunov, A. Forchel, P. Hawrylak, S. Fafard, K. Hinzer, T. Reinecke, S. Walck, J. Reithmaier, F. Klopf, and F. Schäfer. *Phys. Rev. B*, 65:195315, 2002.

[87] D. Xu, N. Zhao, and J. Zhu. *J. Phys.: Condens. Matter*, 20:045204, 2008.

[88] H. Tong and M. W. Wu. *Phys. Rev. B*, 83:235323, 2011.

[89] C. Santori, D. Fattal, M. Pelton, G. S. Solomon, and Y. Yamamoto. *Phys. Rev. B*, 66:045308, 2002.

[90] N. Akopian, N. H. Lindner, E. Poem, Y. Berlatzky, J. Avron, D. Gershoni, B. D. Gerardot, and P. M. Petroff. *Phys. Rev. Lett.*, 96:130501, 2006.

[91] A. Greilich, M. Schwab, T. Berstermann, T. Auer, R. Oulton, D. R. Yakovlev, M. Bayer, V. Stavarache, D. Reuter, and A. Wieck. *Phys. Rev. B*, 73:045323, 2006.

[92] R. Trotta, E. Zallo, C. Ortix, P. Atkinson, J. D. Plumhof, J. van den Brink, A. Rastelli, and O. G. Schmidt. *Phys. Rev. Lett.*, 109:147401, 2012.

[93] J. Plumhof, R. Trotta, A. Rastelli, and O. Schmidt. *Nanoscale Res. Lett.*, 7:336, 2012.

[94] M. Ghali, K. Ohtani, Y. Ohno, and H. Ohno. *Nat. Commun.*, 3:661, 2011.

[95] G. Juska, V. Dimastrodonato, L. Mereni, A. Gocalinksa, and E. Pelucchi. *Nat. Photonics*, 7:527, 2013.

[96] T. Kuroda, T. Mano, N. Ha, H. Nakajima, H. Kumano, B. Urbaszek, M. Jo, M. Abbarchi, Y. Sakuma, K. Sakoda, I. Suemune, X. Marie, and T. Amand. *Phys. Rev. B*, 88:041306, 2013.

[97] N. H. Lindner and T. Rudolph. *Phys. Rev. Lett.*, 103:113602, 2009.

[98] M. Scheibner, S. Economou, A. Bracker, D. Gammon, and I. Ponomarev. *J. Opt. Soc. Am. B*, 29:A82, 2012.

[99] H. Y. Ramírez and S. J. Cheng. *Phys. Rev. Lett.*, 104:206402, 2010.

[100] N. Sköld, A. Boyer de la Giroday, A. J. Bennett, I Farrer, D. A. Ritchie, and A. J. Shields. *Phys. Rev. Lett.*, 110:016804, 2013.

[101] G. Bester and A. Zunger. *Phys. Rev. B*, 72:165334, 2005.

[102] M. Kerfoot, A. Govorov, C. Czarnocki, D. Lu, Y. Gad, A. Bracker, D. Gammon, and M. Scheibner. *Nat. Commun.*, 5:3299, 2014.

[103] B. Szafran, F. M. Peeters, and S. Bednarek. *Phys. Rev. B*, 75:115303, 2007.

[104] R. Hafenbrak, S. M. Ulrich, P. Michler, L. Wang, A. Rastelli, and O. G. Schmidt. *New Journal of Physics*, 9:315, 2007.

[105] A. J. Hudson, R. M. Stevenson, A. J. Bennett, R. J. Young, C. A. Nicoll, P. Atkinson, K. Cooper, D. A. Ritchie, and A. J. Shields. *Phys. Rev. Lett.*, 99:266802, 2007.

[106] A. J. Bennett, M. A. Pooley, R. M. Stevenson, M. B. Ward, R. B. Patel, A. Boyer de la Giroday, N. Sköld, I. Farrer, C. A. Nicoll, D. A. Ritchie, and A. J. Shields. *Nat. Phys.*, 9:315, 2007.

[107] H. Carmichael. *Statistical Methods in Quantum Optics*. Springer, Berlin, Germany, 2002.

[108] F. Troiani, J. I. Perea, and C. Tejedor. *Phys. Rev. B*, 74:235310, 2006.

[109] A. Carmele, F. Milde, M. R. Dachner, M. B. Harouni, R. Roknizadeh, M. Richter, and A. Knorr. *Phys. Rev. B*, 81:195319, 2010.

[110] R. Hanbury Brown and R. Q. Twiss. *Nature*, 178:1447, 1956.

[111] A. Boyer de la Giroday, N. Sköld, R. M. Stevenson, I. Farrer, D. A. Ritchie, and A. J. Shields. *Phys. Rev. Lett.*, 106:216802, 2011.

[112] K. Gawarecki, M. Pochwala, A. Grodecka-Grad, and P. Machnikowski. *Phys. Rev. B*, 81:245312, 2010.

[113] K. Roszak, P. Machnikowski, V. Axt, and T. Kuhn. *Phys. Status Solidi C*, 6:537, 2009.

[114] E. Tsitsishvili and H. Kalt. *Phys. Rev. B*, 82:195315, 2010.

[115] Y. H. Liao, J. I. Climente, and S. J. Cheng. *Phys. Rev. B*, 83:165317, 2011.

[116] H. Wei, G. C. Guo, and L. He. *Phys. Rev. B*, 89:245305, 2014.

[117] F. Fras, B. Eble, P. Desfonds, F. Bernardot, C. Testelin, M. Chamarro, A. Miard, and A. Lemaître. *Phys. Rev. B*, 86:045306, 2012.

[118] P. R. Eastham, A. O. Spracklen, and J. Keeling. *Phys. Rev. B*, 87:195306, 2013.

[119] P. Borri, W. Langbein, U. Woggon, V. Stavarache, D. Reuter, and A. D. Wieck. *Phys. Rev. B*, 71:115328, 2005.

[120] S. Schumacher, J. Förstner, A. Zrenner, M. Florian, C. Gies, P. Gartner, and F. Jahnke. *Opt. Express*, 20:5335, 2012.

[121] R. Trotta, J. S. Wildmann, E. Zallo, O. G. Schmidt, and A. Rastelli. *Nano Lett.*, 14:3439, 2014.

[122] J. Zhang, J. S. Wildmann, F. Ding, R. Trotta, Y. Huo, E. Zallo, D. Huber, A. Rastelli, and O. G. Schmidt. *Nat. Commun.*, 6:10067, 2015.

[123] J. Rolon, K. Wijesundara, S. Ulloa, A. Bracker, D. Gammon, and E. Stinaff. *J. Opt. Soc. Am. B*, 29:A146, 2012.

[124] C. Simon and W. T. M. Irvine. *Phys. Rev. Lett.*, 91:110405, 2003.

[125] C. Simon, Y. M. Niquet, X. Caillet, J. Eymery, J. P. Poizat, and J. M. Gérard. *Phys. Rev. B*, 75:081302(R), 2007.

[126] M. Müller, S. Bounouar, K. D. Jöns, M. Glässl, and P. Michler. *Nat. Photonics*, 8:224, 2014.

[127] M. Scheibner, S. E. Economou, I. V. Ponomarev, C. Jennings, A. S. Bracker, and D. Gammon. *Phys. Rev. B*, 92:081411(R), 2015.

[128] S. Stufler, P. Machnikowski, P. Ester, M. Bichler, V. M. Axt, T. Kuhn, and A. Zrenner. *Phys. Rev. B*, 73:125304, 2006.

[129] P.-L. Ardelt, L. Hanschke, K. A. Fischer, K. Müller, A. Kleinkauf, M. Koller, A. Bechtold, T. Simmet, J. Wierzbowski, H. Riedl, G. Abstreiter, and J. J. Finley. *Phys. Rev. B*, 90:241404(R), 2014.

[130] S. Bounouar, M. Müller, A. M. Barth, M. Glässl, V. M. Axt, and P. Michler. *Phys. Rev. B*, 91:161302(R), 2015.

[131] R. Trivedi, K. A. Fischer, J. Vučković, and K. Müller. *Adv. Quantum Tech.*, 3:1900007, 2020.

[132] J. Houel, A. V. Kuhlmann, L. Greuter, F. Xue, M. Poggio, B. D. Gerardot, P. A. Dalgarno, A. Badolato, P. M. Petroff, A. Ludwig, D. Reuter, A. D. Wieck, and R. J. Warburton. *Phys. Rev. Lett.*, 108:107401, 2012.

[133] A. V. Kuhlmann, J. Houel, A. Ludwig, L. Greuter, D. Reuter, A. D. Wieck, M. Poggio, and R. J. Warburton. *Nat. Phys.*, 9:570, 2013.

[134] N. Ha, T. Mano, Y.-L. Chou, Y.-N. Wu, S.-J. Cheng, J. Bocquel, P. M. Koenraad, A. Ohtake, Y. Sakuma, K. Sakoda, and T. Kuroda. *Phys. Rev. B*, 92:075306, 2015.

[135] D. Chen, G. R. Lander, K. S. Krowpman, G. S. Solomon, and E. B. Flagg. *Phys. Rev. B*, 93:115307, 2016.

[136] C. Bardot, M. Schwab, M. Bayer, S. Fafard, Z. Wasilewski, and P. Hawrylak. *Phys. Rev. B*, 72:035314, 2005.

[137] X. R. Zhou, J. H. Lee, G. J. Salamo, M. Royo, J. I. Climente, and M. F. Doty. *Phys. Rev. B*, 87:125309, 2013.

[138] I. Vega and D. Alonso. *Rev. Mod. Phys.*, 89:015001, 2017.

[139] M. Abbarchi, T. Kuroda, T. Mano, M. Gurioli, and K. Sakoda. *Phys. Rev. B*, 86:115330, 2012.

[140] J. A. Barker and E. P. O'Reilly. *Phys. Rev. B*, 61:13840, 2000.